Inaugural Dissertation

The effect of inducible nitric oxide synthase-ablation in pulmonary artery smooth muscle cells on cigarette smoke-induced pulmonary hypertension and emphysema development

submitted to the
Faculty of Medicine
in partial fulfillment of the requirements
for the PhD-Degree
of the Faculties of Veterinary Medicine and Medicine
of the Justus Liebig University Giessen

by

Wu, Cheng-Yu

of

New Taipei City, Taiwan

Giessen 2023

From the Department of Internal Medicine
Director: Prof. Dr. Werner Seeger of the Faculty of Medicine of the Justus Liebig University Giessen

Committee:

Supervisor and the First Reviewer: Prof. Dr. Norbert Weißmann
Second Reviewer: Prof. Tim Lahm
Vice-Chair and Co-supervisor: Prof. Dr. Martin Diener
Chair: Prof. Klaus-Dieter Schlüter

Date of Doctoral Defense: 09. August. 2023

Table of contents

1. Introduction

1.1 Respiratory System: Anatomy and Function

The respiratory system in the most of vertebrates is essential for gas exchange. These organisms require different strategies than unicellular organisms to transport oxygen (O_2) and carbon dioxide (CO_2) to the diffusional barriers [1]. The structure of the respiratory system is tailored to its living environment, body build, pattern of the movement, and energy consumption [2]. For example, shark have gills to acquire O_2 from the water, whereas raccoons breathe through their lungs. Both gills and lungs comprise thin-walled structures of the gas-blood barrier, which allows exchanging gases between the environment and the blood, referred to as external respiration. The circulatory system subsequently delivers O_2 to tissues/cells to allow the internal respiration [2]. Ultimately, in the presence of O_2, cells undergo aerobic cellular respiration [3]. O_2 in cells serves as an electron acceptor in the mitochondrial electron transport chain during oxidative phosphorylation to generate an energy-carrying molecule – adenosine triphosphate (ATP) [4] **(Figure 1)**.

1.1.1 The structure of human respiratory system

Human respiratory system can be divided into the upper and lower respiratory system by structure [1]. When the air is inhaled, it first passes the upper respiratory tract, consisting of the nasal or oral cavity (*cavum nasi* or *cavum oris*), *pharynx*, and *larynx* [1]. Then, it enters the lower respiratory system, which, by function, can be further subdivided into conducting zone and respiratory zone [1]. The conducting airways in the lower respiratory tract comprises of *trachea*, several divisions of bronchi (e.g. *bronchus principalis*, *bronchus lobaris*, and *bronchus segmentalis*), and several divisions of bronchioles branching until the terminal bronchioles (*broncholus terminales*) [1]. The respiratory zone of the lung contains respiratory bronchioles (*bronchiolus respiratorius*), alveolar ducts (*ductus alveolaris*), and alveolar sacs (*saccus alveolaris*) [1] **(Figure 2)**.

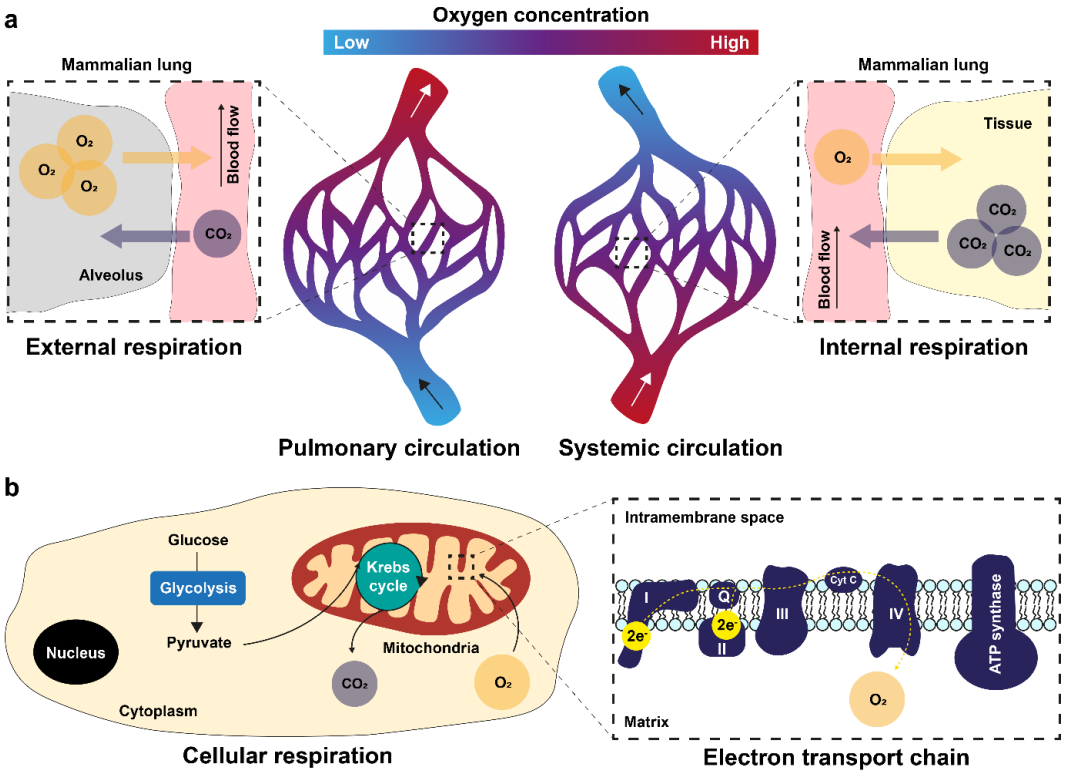

Figure 1. External, internal and cellular respiration. a, Graphical representation of gas exchange during external and internal respiration in mammalians. External respiration occurs in the alveolus of the mammalian lung, from which O_2 diffuses to erythrocytes. In contrast, CO_2 diffuses from the pulmonary circulatory system to the air in the lung alveolus. O_2 is then conveyed to the tissue/cell by the circulatory system, where the internal respiration is taking place. CO_2, on the other hand, enters the circulatory system to be transported to the lung alveolus. **b,** Illustration of cellular respiration from glycolysis to oxidative phosphorylation and the role of O_2 in the cellular respiration.
Abbreviations: O_2, Oxygen. CO_2, Carbon dioxide. e^-, Electron. I, Mitochondrial complex I. II, Mitochondrial complex II. III, Mitochondrial complex III. IV, Mitochondrial complex IV. Q, Coenzyme Q. Cyt C, Cytochrome c.

1.1.2 Human conducting airways

The main functions of the conducting zone are to provide a path for incoming and outgoing air, warm and humidify the passing air, as well as remove pathogens, dust and debris [1]. The entire air passageway in mammals is lined with epithelial cells [5]. The human proximal airways (trachea/bronchi) are composed of a pseudostratified epithelium with multiple cell types, including multi-ciliated cells, secretory club cells, mucus-producing goblet cells, basal cells and neuroendocrine cells [5]. The human distal airways, from bronchioles to the bronchiole-alveolar

duct junction (BADJ), consists of a columnar surface epithelium with similar cell types, but relatively more ciliated cells and club cells [5]. Besides, there are bronchoalveolar stem cells (BASC) at the BADJ region, which serve as progenitor cells for the replenishment of bronchial epithelial cells and alveolar epithelial cells [6] **(Figure 3)**.

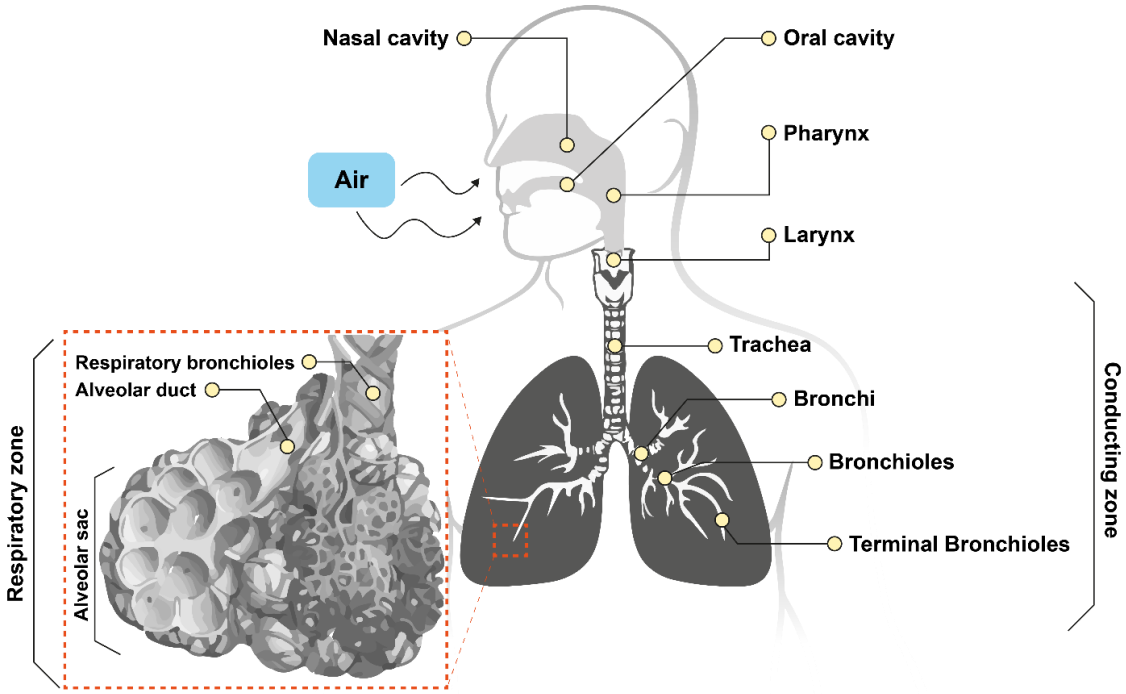

Figure 2. The anatomy of the human respiratory system. Graphical representation of the pathway for the air. During inhalation, air enters the upper respiratory tract via nasal or oral cavity, Then it travels through pharynx and larynx and passes by the conducting zone (trachea, bronchi, bronchioles and terminal bronchioles) and finally reaches the respiratory zone (respiratory bronchioles, alveolar duct and alveolar sac with alveoli). The image was modified from/designed based on the text book – *Human anatomy & physiology* by Elaine N. Marieb and Katja N. Hoehn [7].

1.1.3 The respiratory zone of the human lung

The respiratory zone corresponds to the areas directly involved in gas exchange. The end-point of the mammalian respiratory system consists of thin-walled structures enveloped with capillaries, termed alveolus **(Figure 4)**. The human lung contains approximately 500 million alveoli, with an overall surface area of the respiratory membranes of 100 – 150 m^2 [8]. Such an enormous air-blood

interface area ensures an efficient gas exchange [9]. The driving force for gas exchange in the lung is the pressure gradient [9]. In the ideal situation, partial pressure of oxygen (pO_2) in ambient air (at sea level) is 159 mmHg [10]. A portion of inhaled air is in the conductive zone of respiratory system and does not participate in gas exchange (so-called anatomical dead space) [11]. Therefore, pO_2 decreases to about 100 mmHg when the air reaches the alveoli [11]. As pO_2 in the systemic venous blood is 40 mmHg, O_2 in the alveoli can move across the membranes by passive diffusion [9]. In contrast, pCO_2 in alveolar gas is 40 mmHg and in the venous blood of the body is approximately 45 mmHg [9]. Therefore, CO_2 diffuses to the alveoli and is then exhaled.

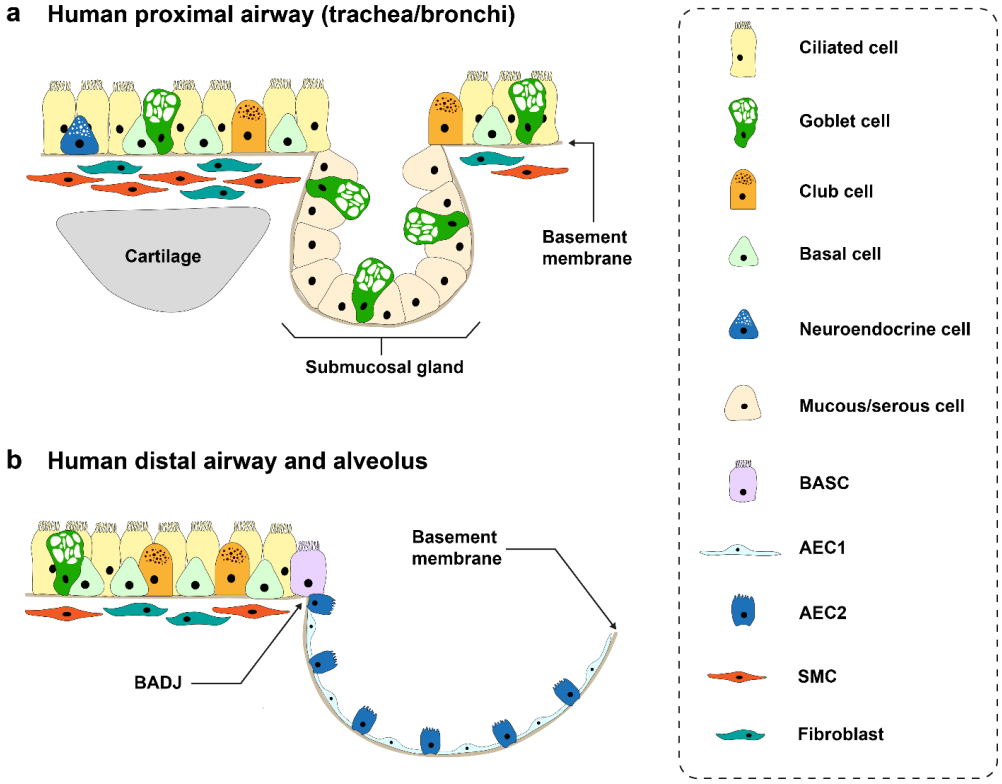

Figure 3. Cell composition of the human proximal airway, distal airway and alveolus. Graphical representation of **a,** the proximal airway (trachea/bronchi) and **b,** the distal airway to the alveolus. Note that some cells are not shown in the figure (e.g. immune cells). This figure was designed based on the publication [12].
Abbreviations: BADJ, Bronchiole-alveolar duct junction. BASC, Bronchoalveolar stem cell. AEC1, Alveolar type 1 epithelial cell. AEC2, Alveolar type 2 epithelial cell. SMC, Smooth muscle cell.

By measuring pCO_2 in pulmonary arterial blood and pCO_2 in the expired air, one can estimate the volume of physiological dead space, which includes the volume of anatomic dead space and the volume of alveolar dead space [13]. This method is known as the Enghoff modification of the Bohr's method [13]. Under the pathologic conditions, exemplified by pulmonary emphysema (see section 1.2.2), the volume of alveolar dead space is increased [13]. Thus, measuring physiological dead space volume can be a clinical application in the respiratory medicine [13].

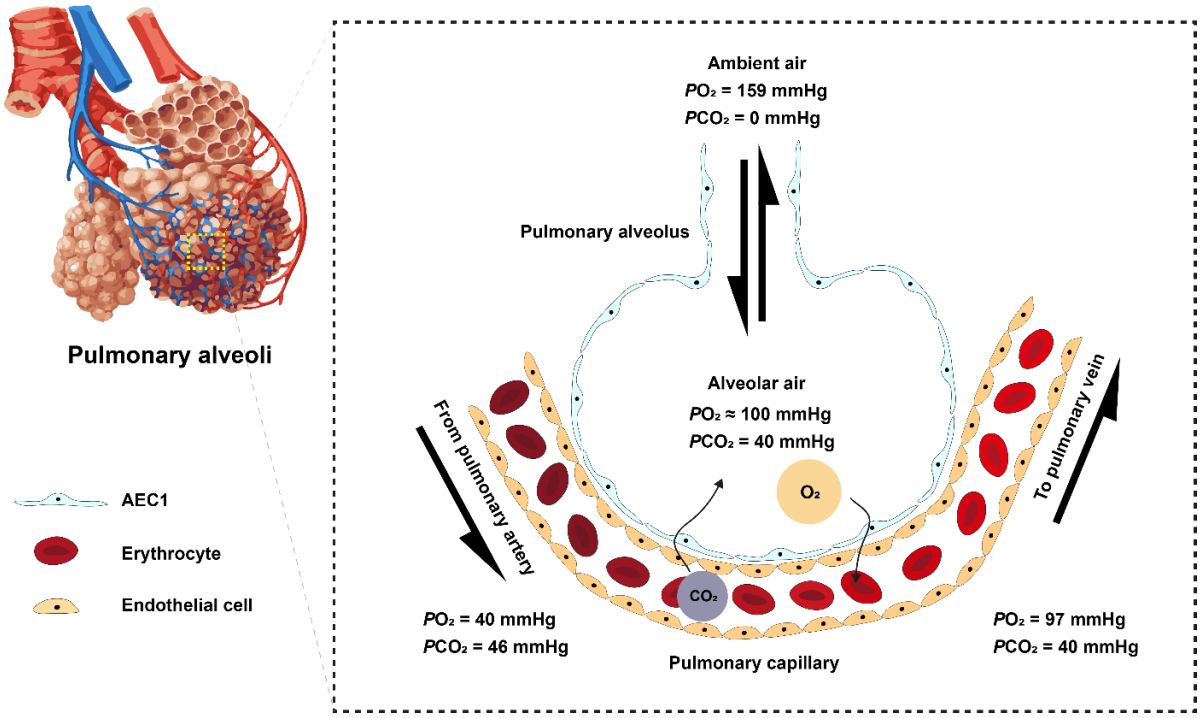

Figure 4. Ideal model of alveolar gas exchange. Graphical illustration of alveolar gas exchange depicting an ideal situation. The deoxygenated venous blood enters the pulmonary capillaries via the pulmonary arteries. Owing to the different gas partial pressures, O_2 diffuses from the alveoli into the blood (mainly into the erythrocytes) and CO_2 diffuses from the blood into the alveoli. The oxygenated blood flows through the heart and enters the systemic circulation. The image was modified from/designed based on the text book – *Human anatomy & physiology* by Elaine N. Marieb and Katja N. Hoehn [7].
Abbreviations: AEC1, Alveolar type 1 epithelial cell. pO_2, The partial pressure of O_2. pCO_2, The partial pressure of CO_2. O_2, Oxygen. CO_2, Carbon dioxide.

Another important clinical tool in pulmonary medicine is spirometry [14]. This method is to measure lung volume and capacity in a human individual [15]. Lung volume is defined as the

volume of air in the lung during inspiration and expiration [9]. There are four termini defined: (1) the tidal volume (TV), defined as the volume of air inhaled or exhaled during normal breathing (average in human is 0.5 l); (2) the inspiratory reserve volume (IRV), defined as the volume of gas that can be forcibly inhaled after normal breathing (average in human is 2.5 l). (3) the expiratory reserve volume (ERV), defined as the volume of gas that can be forcibly expired after normal breathing (average in human is 1.5 l) and (4) the residual volume (RV), defined as the volume of air remaining in the lungs after maximal exhalation (average in human is 1.5 l) [9].

Based on these four "standard" volumes, it is possible to calculate different lung capacities:

$$The\ inspiratory\ capacity\ (IC) = IRV + TV$$

$$The\ functional\ residual\ capacity\ (FRC) = ERV + RV$$

$$The\ vital\ capacity\ (VC) = IRV + TV + ERV$$

$$The\ total\ lung\ capacity\ (TLC) = IRV + TV + ERV + RV$$

Spirometry is very useful for diagnosing lung diseases, characterizing the severity of the diseases, and assessing the response to treatments [14]. One of the most commonly used parameters to analyze pulmonary function is the forced expiration [16]. For example, the ratio of the forced expiratory volume in one second (FEV1) to the forced vital capacity (FVC) (also known as Tiffeneau-Pinelli index) can help to identify whether a patient suffers from a lung disease such as COPD, which will be further addressed in the next section [17].

1.2 Chronic Obstructive Pulmonary Disease (COPD)

Chronic obstructive pulmonary disease (COPD) is a global health problem with, in addition to the burden for the patients, a tremendous socio-economic burden [18]. COPD is a progressive and heterogeneous lung disease with multiple characteristics, such as chronic bronchitis, small airway obstruction, and pulmonary emphysema [12, 18, 19]. Dyspnea, chronic cough and sputum hyper-production are the clinical manifestations in patients with COPD [20]. The patients with COPD may experience frequent acute worsening of respiratory symptoms, so called exacerbations. Exacerbations are mainly attributed to bacterial/viral infections, which deteriorate the patients' health status and accelerate the disease progression [21-23]. Moreover, patients with COPD often suffer from lung cancer and at least mild pulmonary hypertension, which increases the mortality of the patients [19, 24].

The primary cause of COPD development is the inhalation of particulate matter or noxious gas from cigarette smoking. However, in some countries (e.g. China or India), air pollution is the leading etiological factor of the disease [25]. Apart from the environmental risk factors, the disease development may be associated with genetic predisposition. Alpha-1 antitrypsin deficiency (AATD) is a well-known disorder that causes pulmonary emphysema, but it accounts for less than 3% of all COPD cases [26]. Therefore, recent studies focus on phenotyping and/or endotyping this heterogeneous complex disorder, so the pharmacological interventions can be tailored to corresponding groups of patients [27, 28]. To put it into practice, the investigations of the host susceptibility to the disease and their cellular or molecular responses to environmental risk factors are thus becoming necessary [29].

1.2.1 Chronic bronchitis and small airway remodeling in COPD

The classical clinical definition of chronic bronchitis is *"the presence of cough and sputum production for at least 3 months in each of two consecutive years"* [30]. Mucus hyper-production is one of the main features in patients with chronic bronchitis. This characteristic is due to hyper-responsiveness towards environmental irritants that causes mucous glands hypertrophy in the trachea and main bronchi, and goblet cell hyperplasia in the surface epithelium of small airways [31, 32]. In addition to goblet cell hyperplasia, goblet cell metaplasia, small airway remodeling also consists of basal membrane thickening, bronchial smooth muscle cell hyper-proliferation,

immune cell infiltration, and bronchiolar wall fibrosis **(Figure 5)**. Consequently, it drives the inner airway lumen narrowing and gives rise to a significant irreversible airflow limitation in patients with COPD [33].

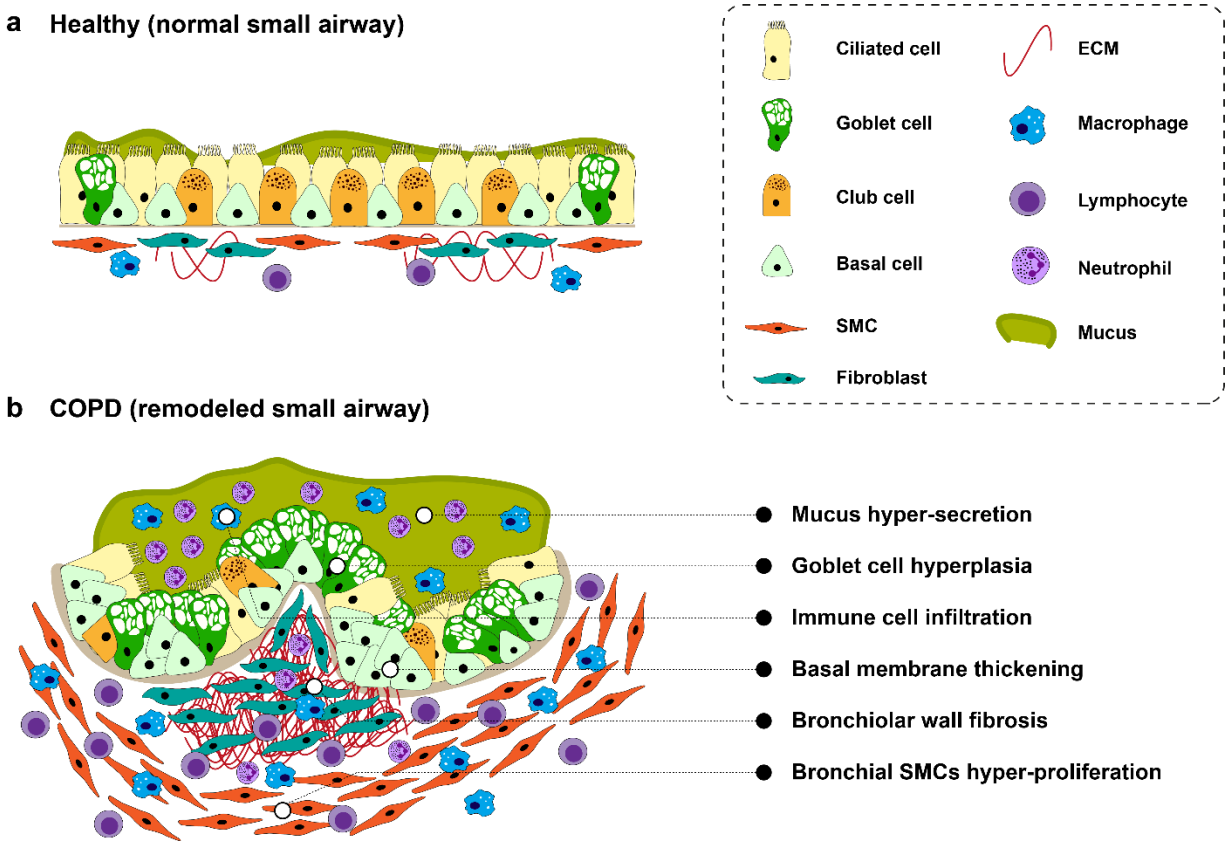

Figure 5. Small airway in a healthy and in a COPD lung. Graphical representation of the **a,** human healthy small airway (inner diameter < 2 mm) and **b,** remodeled airway in human COPD. Abbreviations: SMC, Smooth muscle cell. ECM, Extracellular matrix.

1.2.2 Pulmonary emphysema in COPD

Pulmonary emphysema is another cardinal feature of COPD. By definition, it is "*abnormal permanent enlargement of the air spaces distal to the terminal bronchioles, accompanied by destruction of their walls and without obvious fibrosis"* [34]. The enlargement of the air spaces is mainly attributed to degradation of extracellular matrix (e.g. elastic or collagen fibers) and loss of respiratory surface (e.g. alveoli) [35]. There are several patho-morphological types of emphysema, such as (1) centrilobular (centriacinar), (2) panlobular (panacinar), (3) paraseptal (distal acinar), and (4) irregular emphysema **(Figure 6)** [32].

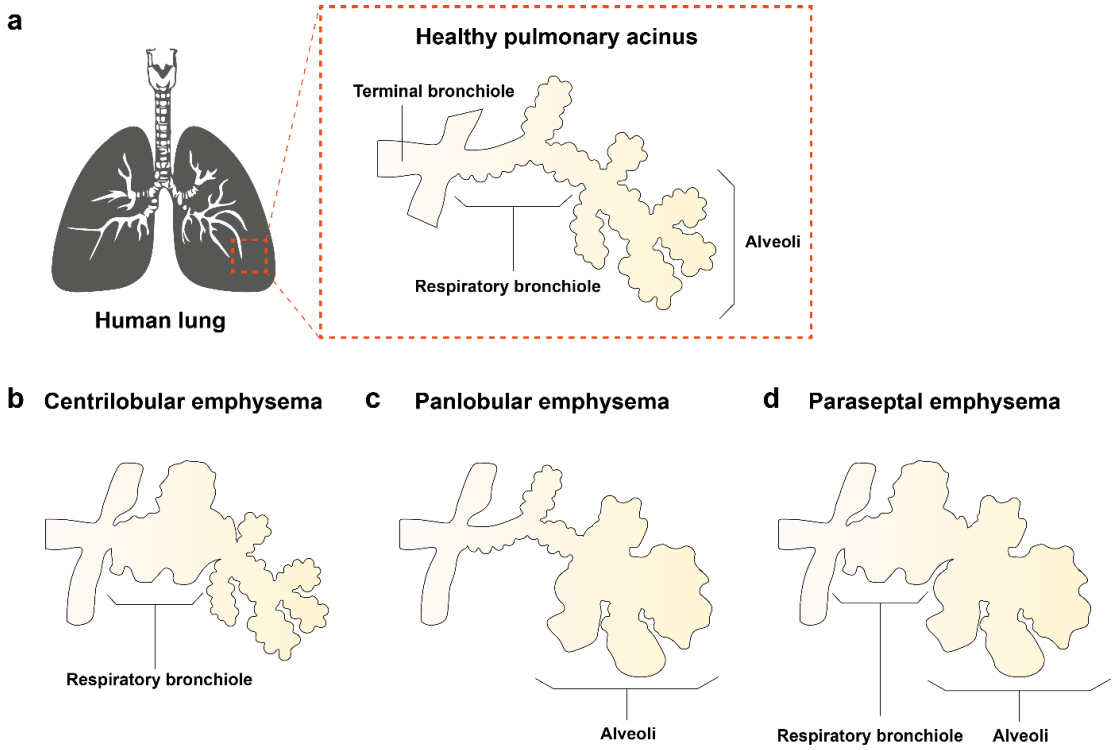

Figure 6. Major patterns of pulmonary emphysema. a, Schematic drawing of the healthy human pulmonary acinus. **b,** Centrilobular emphysema with enlargement in the respiratory bronchiole. **c,** Panlobular emphysema with dilation of the alveoli. **d,** Paraseptal emphysema with air trapping in both respiratory bronchiole and alveoli.

(1) Centrilobular emphysema is predominantly seen in patients who are cigarette smokers, but do not have AATD [32]. The destruction occurs in the proximal acini, primarily formed by respiratory bronchioles. It is typically affecting apical segments of the upper lobes. The patients with centrilobular emphysema do not have increased lung compliance, but severe airway remodeling and airflow limitations [36, 37]. Despite the distinctive pattern, the distal acini may become emphysematous in those patients with severe centrilobular emphysema and thus it may be difficult to distinguish between centrilobular and panlobular emphysema [32].

(2) Panlobular emphysema is characterized by uniform enlargement of the acini from the level of the respiratory bronchioles to the terminal alveolar ducts. Compared with centrilobular emphysema, panlobular emphysema tends to occur in the lower lungs and it is a main feature of patients with AATD [37].

(3) Paraseptal emphysema features an emphysematous distal acinus, but a normal proximal acinus. It occurs mainly in peripheral regions near the pleura. Cystic structures – known as bullae - may appear due to massive airspace enlargement [32].

(4) A hallmark of irregular emphysema, are the irregularly affected acini due to the scarring, caused by inflammatory diseases such as tuberculosis [38].

1.2.3 COPD-associated pulmonary hypertension

Pulmonary hypertension (PH) is defined by a mean pulmonary artery pressure (mPAP) higher than 20 mmHg at rest [39]. An elevated mPAP can be caused by several factors, such as an increased cardiac output, an intercardiac shunt, a high blood viscosity and an increased arterial wedge pressure (PAWP) due to the heart or chronic lung disease [40]. Increased afterload for the right ventricle (RV) is a consequence of elevated mPAP. This results in right ventricular hypertrophy, which can be beneficial for the heart to cope with augmented pulmonary vascular resistance (PVR) [19, 39]. PAWP and PVR were included as important criteria by the latest World Symposium on Pulmonary Hypertension (WSPH) to define if an individual has pre-capillary, post-capillary or combined PH [39]. For instance, to determine if an individual has pre-capillary PH, a mPAP > 20 mmHg, a PAWP $\leq$ 15 mmHg and a PVR $\geq$ 3 Wood units are required. [39-41]. Besides, the WSPH has also classified PH into 5 groups, whereas the hereby investigated PH – PH due to chronic lung disease and/or hypoxia – is classified as group 3 [39]. Reportedly, up to 90% of COPD patient's mPAP is >20 mmHg at rest with profound pulmonary vascular remodeling. The remodeling, such as muscularization or pruning of small blood vessels, was observed not only in patients with COPD, but also in smokers without COPD [42]. Additionally, long-term cigarette smoke (CS) exposure in animal models revealed that pulmonary vascular remodeling precedes emphysema development [43-47], indicating that alterations of the pulmonary vasculature contribute to the lung parenchymal changes and are significantly associated with the COPD development and the prognosis of the patients [19].

1.2.4 Diagnosis, classification of COPD and the disease management

As mentioned in the section 1.1.3, assessment of lung volumes can be a diagnostic tool to determine whether a subject is suffering from a lung disease. According to the guidelines published annually by the Global Initiative for Chronic Obstructive Lung Disease (GOLD), if a subject's spirometry test result in a FEV1/FVC < 0.7 after application of a bronchodilator, then the subject is diagnosed with COPD [48]. In addition, the GOLD has classified patients diagnosed with COPD into four stages of disease severity **(Table 1)**. Together with assessing the patients' risk of exacerbation risk symptom burden, health care professionals can follow the guidelines and provide precise management and treatment to improve or maintain patients' quality of life [20].

Table 1. Classification of COPD severity according to the GOLD guideline.

Stage	Severity	FEV_1%Predicted
GOLD stage 1	Mild	$FEV_1 > 80\%$ predicted
GOLD stage 2	Moderate	$50\% \leq FEV_1 < 80\%$ predicted
GOLD stage 3	Severe	$30\% \leq FEV_1 < 50\%$ predicted
GOLD stage 4	Very severe	$FEV_1 < 30\%$ predicted

1.2.5 Cellular and molecular mechanisms of CS-induced COPD

Several cellular and molecular mechanisms underlying CS-induced COPD development have been identified, such as augmented inflammatory response, unbalanced proteases/anti-protease activity, aberrant cell death/senescence and immoderate nitrosative/oxidative stress [44, 49-51]. These mechanisms may coexist or promote each other, forming a vicious circle.

Aberrant and enhanced inflammatory immune response towards inhaled particles or noxious gas, primarily from CS, is considered as a hallmark of COPD [52]. The toxic components from CS can activate pattern recognition receptors (PRR) such as toll-like receptors. Activation of PRR triggers innate immune responses, which further leads to the induction of adaptive immunity [52]. The cells that participates in the immune responses, including epithelial cells, macrophages, mast cells, neutrophils, eosinophils, natural killer cells (innate), T-cells and B-cells (adaptive), secret pro-

inflammatory cytokines, chemokines, or proteolytic enzymes and produce reactive nitrogen/oxygen species (RNS/ROS) **(Figure 7a)**.

An augmented inflammatory response leads to hyper-production of proteolytic enzymes, such as neutrophil-derived elastase, macrophages-released matrix metalloproteinases (MMPs), mast cells-produced chymase, and T-cells-secreted perforin. These proteases not only breakdown the extracellular matrix (ECM) (e.g. elastin/collagen fragments), but also induce cell death and senescence, which ultimately generate emphysematous lesions in the lungs [52-55] **(Figure 7b)**.

Apart from proteases, CS can cause both programed (e.g. apoptosis) and non-programed (e.g. necrosis) cell death, depending on the degree of stimulations [12]. In the case of rapid and extreme cell injury, the cells undergo necrosis (so-called accidental death). Compared with apoptotic cells, the necrotic cells release a large amount of damage-associated molecular patterns (DAMPs), which further potentiates pro-inflammatory signaling by activating PRR [52, 56]. In contrast, cell senescence may occur during exposure to CS as well [57]. One of the main features of cell senescence is a permanent cell cycle arrest in response to a plethora of stress [58]. However, these "zombie" cells can remain metabolically active and change their secretomic patterns. This phenotype has been termed as senescence-associated secretory phenotype (SASPs), which can alter the micro-milieu in the lungs and contributes to chronic inflammation [59]. Moreover, senescent stem cells lose the self-renewal properties, leading to impaired lung repair and COPD development/progression [58, 60] **(Figure 7c)**.

Cell death and senescence can result from excessive RNS/ROS production. The production of RNS/ROS in the lung primarily comes from immune cells, such as macrophages and neutrophils, and serves as a weapon for killing exogenous pathogens [61]. However, in addition to the immune cells, the bronchial/alveolar epithelial cells and the vascular cells such as pulmonary artery smooth muscle cells (PASMCs) can generate RNS/ROS upon stimulation as well [61]. The disturbance in the balance between the production of RNS/ROS, such as nitric oxide (NO)/superoxide (O_2^-), and antioxidant defense mechanisms, leads to nitrosative/oxidative stress [61]. In the context of CS-induced COPD, the inducible nitric oxide synthase (iNOS) is a crucial source of nitric oxide (NO) [44]. In COPD patients, iNOS is upregulated in pulmonary vascular cells, alveolar macrophages, eosinophils, neutrophils and AEC2 [44, 62, 63]. Recently, a non-phagocytic nicotinamide adenine dinucleotide phosphate (NADPH) oxidase, dependent on the subunit NADPH oxidase organizer 1

(NOXO1) was suggested as a primary source and regulator of O_2^- production in lung emphysema/COPD [47, 64]. Moreover, NO and O_2^- react in a diffusion-limited fashion, generating a highly reactive molecule – peroxynitrite ($ONOO^-$). $ONOO^-$ can post-translationally modify proteins at tyrosine residues, forming 3-nirtotyrosine (3-NT), which has been linked to COPD severity [65, 66]. In COPD, 3-NT is not only a marker of nitrosative/oxidative stress, but also, above a certain threshold, can alter cell signaling, affecting cell migration/proliferation, and cause senescence or cell death. Eventually, it propagates disease progression [62, 67-70] **(Figure 7d)**.

Even though cigarette smoking is the major etiological factor of COPD, only about one quarter of smokers develop the disease [70, 71]. Some individuals do not have significant structural destruction in the lungs despite chronic smoking [72, 73]. Therefore, accumulating research articles focus on investigating the interactions between host susceptibility and environmental factors [29]. It has been reported that genetic variations in antioxidant enzymes, leading to the discrepancy in antioxidant defense between individuals, is a determinant of host susceptibility to CS injury [29, 74, 75]. For example, polymorphisms in the promoter region of nuclear factor erythroid-derived 2-like 2 (Nrf2) have been linked to the COPD susceptibility [76]. In a COPD animal model, deletion of Nrf2 gene predisposed mice to CS-induced emphysema [77]. Nrf2 is a transcription factors that regulates the expression of several antioxidant genes, such as superoxide dismutases (SODs) and heme oxygenase 1 (HO-1) [76]. Along this line, different levels of *HO-1* gene expression were observed in lung tissues of smokers with severe emphysema and smokers with no/mild emphysema [78]. The polymorphisms in the *HO-1* promoter region, which affect the protein expression level, were associated with the COPD susceptibility in smokers [79]. Thus, boosting endogenous anti-oxidant defense by activating Nrf2 or overexpressing HO-1 can be a potential therapeutic strategy to alleviate nitrosative/oxidative stress in several diseases, including COPD [76, 80] **(Figure 7d)**.

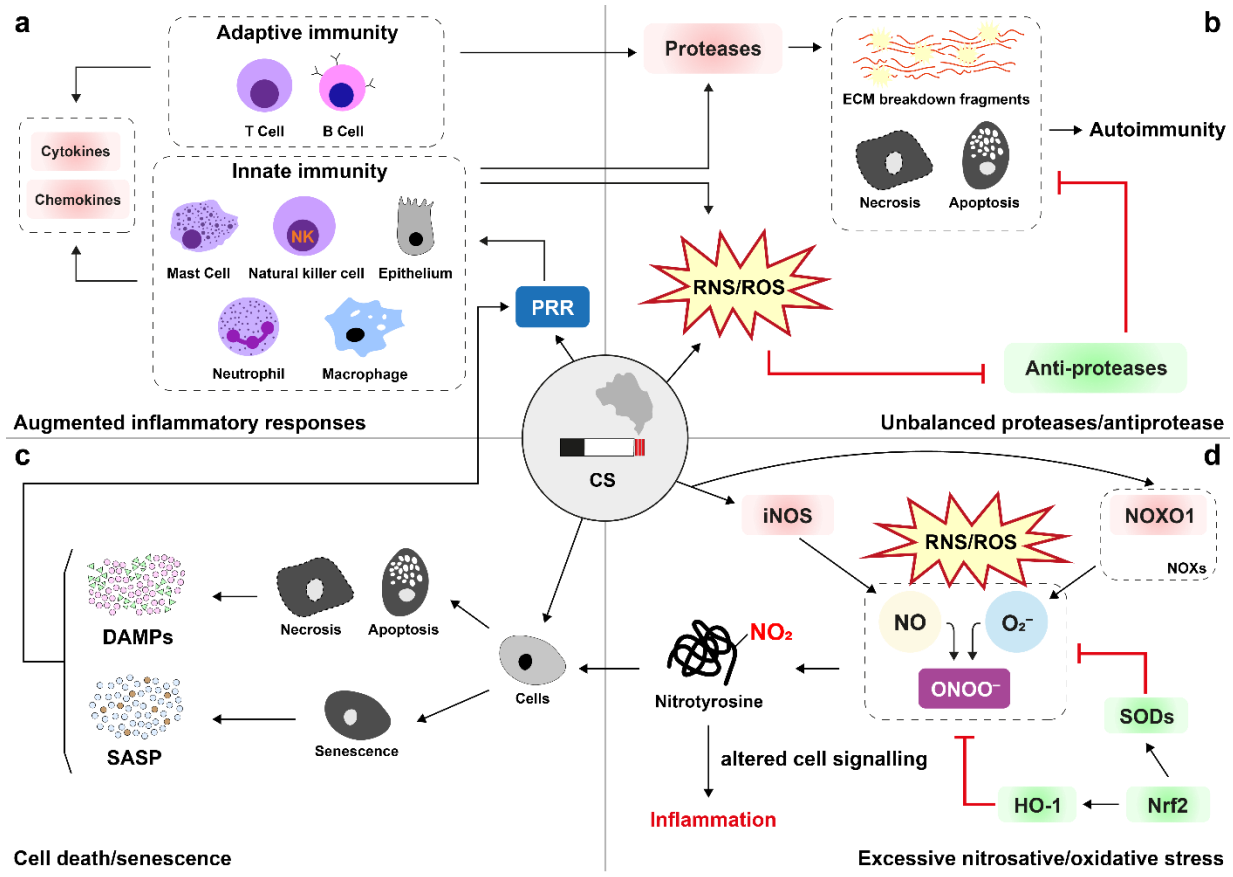

Figure 7. Cellular and molecular mechanisms of CS-induced COPD. a, Augmented inflammatory response in CS-induced COPD. **b,** Unbalanced proteases/anti-protease activity. **c,** Cell death/senescence. **d,** Excessive nitrosative/oxidative stress.
Abbreviations: PRR, Pattern recognition receptor. RNS, Reactive nitrogen species. ROS, Reactive oxygen species. ECM, Extracellular matrix. CS, Cigarette smoke. DAMPs, Damage-associated molecular patterns. SASP, Senescence-associated secretory phenotype. iNOS, Inducible nitric oxide synthase. NOX, Nicotinamide adenine dinucleotide phosphate (NADPH) oxidase. NOXO1, NADPH oxidase organizer 1. NO, Nitric oxide. O_2^-, Superoxide. $ONOO^-$, Peroxynitrite. SOD, Superoxide dismutase. HO-1, Heme oxygenase 1. Nrf2, Nuclear factor-erythroid factor 2-related factor 2.

1.3 Animal models of cigarette smoke (CS)-induced COPD

Modeling human diseases in experimental animals has led to many breakthroughs in biomedical research. For example, Louis Pasteur (1822–1895) developed the effective vaccines against rabies using a rabbit model [81]. His counterpart, Robert Koch (1843–1910) identified *Tubercle bacillus* and verified it in an animal model [82]. Koch's students Emil von Behring (1854–1917) discovered antitoxins by performing animal experiments [83]. In terms of CS-induced COPD, several animal models, mostly in rodents (especially in mice), have been designed to investigate the pathological mechanisms. Eventually, it paves the way to implement a potential therapeutic strategy [84, 85].

1.3.1 Anatomical differences of the lung between mice and humans

Although mammals exhibit a relatively conserved lung structure and function [86], there are some major differences between mice and human. Therefore, it is important to consider this when designing animal experiments. Both, human and mouse lungs, contain 5 lobes, but the lobulation between mice and human are not identical. The human right lung (*pulmo dexter*) contains 3 lobes (*lobus superior*, *lobus medius*, *lobus inferior*) and left lung (*pulmo sinister*) consists of 2 lobes (*lobus superior*, *lobus inferior*) [1]. In mouse, there are four lobes (*lobus cranialis*, *lobus medius*, *lobus caudalis* and *lobus cardialis*) in the right lung and only one lobe in the left lung (*lobus sinister*) [87]. As mice are quadruped, the ramification modus of bronchi are different from human [88]. The airway branching in the mouse lung is more asymmetric than in humans. Also, the mouse airway consists of 13 – 17 generations of bifurcation [89], whereas the human tracheobronchial tree has 23 generations [90]. Another significant difference between mouse and human lung is the cellular composition of the airway epithelium [91]. The mouse intrapulmonary airway is lined with simple columnar epithelia [91]. There are no basal cells or goblet cells in mouse small airways [5]. This makes it challenging to recapitulate human small airway disease by using a mouse model. Alternatively, the guinea pig model would be more suitable to mimic the human airway disease [46, 92].

1.3.2 Chronic CS exposure in mice

Despite the difference in the lung organization between humans and mice, CS-exposed mice share multiple similarities with human cigarette smokers [85, 92]. Mice after 3 months of CS exposure

showed increased mPAP and vasculature remodeling, whereas the airspace enlargement and loss of alveoli appeared only in mice exposed to CS more than 6 months [44, 47, 93, 94]. These findings are in line with the observations in smokers that the alterations in the pulmonary vasculature precede emphysema development [19, 42]. In mice, long-term CS exposure also leads to augmented inflammatory responses and excessive nitrosative/oxidative stress [95, 96]. Moreover, data from mouse *in vivo* studies, either using pharmacological approaches or targeting genes involved in these molecular mechanisms, provide an insight into implementing a potential therapeutic strategy [12, 97-99]. Although the chronic CS exposure mouse COPD model has brought several groundbreaking results, it has a significant limitation: the animals can never develop as severe emphysema as humans at end-stage COPD [92]. To recapitulate the human end-stage emphysema in mice, one should consider using other models, such as the elastase-induced emphysema mouse model [100].

1.3.3 Genetic engineering in mice

To determine the contribution of certain genes associated with disease development, scientists have developed many revolutionary gene-targeting techniques for animal models. Three pioneers, Oliver Smithies, Sir Martin Evans and Mario Capecchi, used embryonic stem cells to generate specific gene-knockout mice [101, 102]. Since then, gene manipulation in mice has become a mainstream to address biological or medical questions [103]. In the context of COPD research, using transgenic or gene-targeted mice enables scientists to elucidate several cellular/molecular mechanisms, underlying CS-driven emphysema development [85]. However, congenital gene-deletion may cause developmental abnormalities in mice [92]. For example, mice lacking the gene encoding for the platelet derived growth factor A (*Pdgfa*$^{-/-}$) suffer from failed alveogenesis and deletion of tissue inhibitor of metalloproteinases (*Timp3*), leading to spontaneous emphysema development [104]. Therefore, conditional gene-deletion in mice can be a good strategy to overcome these challenges.

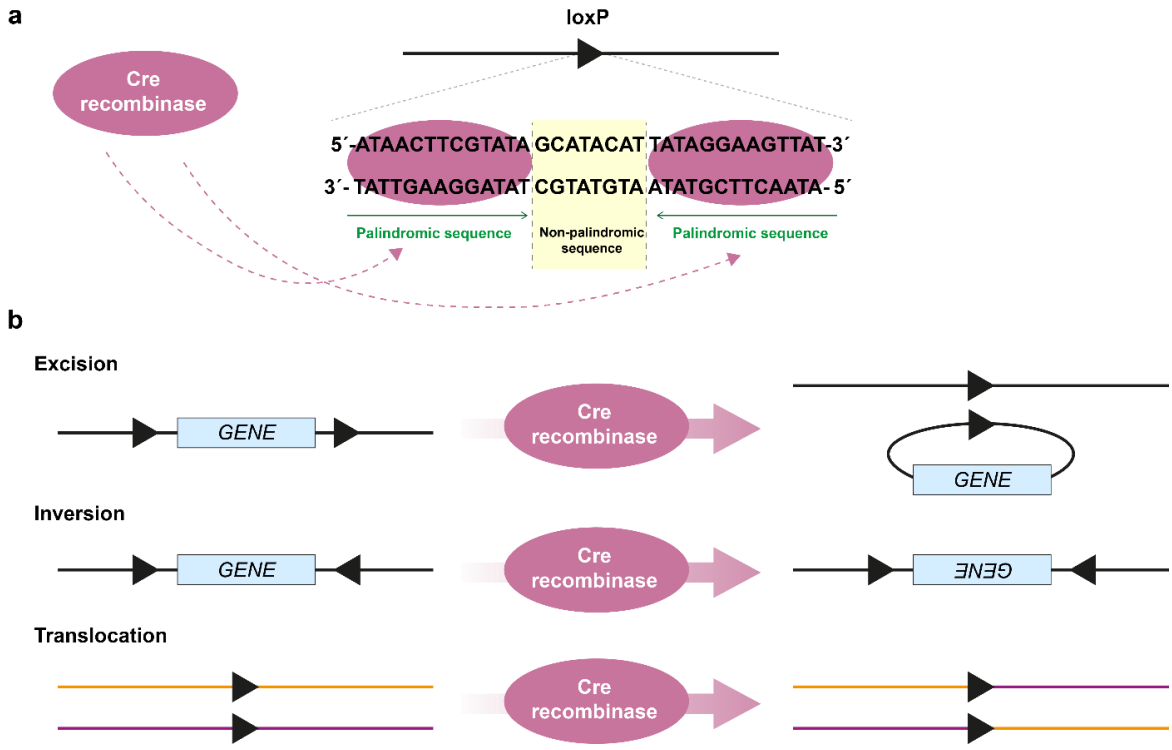

Figure 8. Mechanism of the Cre-loxP system. a, Cre recombinase and the canonical sequence of loxP. Cre recombinase (38 kDa) binds to the recognition sites – palindromic sequence (13 bp) of loxP. **b,** Graphical illustration of three different genomic outcomes of site-specific Cre-loxP recombination, depending on the orientation of the loxP sites.
Abbreviations: Cre, Causes recombination. LoxP, Locus of crossover in P1 bacteriophage.

1.3.3.1 Conditional gene-editing in mice using a Cre-loxP system

To achieve conditional gene-editing in mice, a system using the causes recombination (Cre) recombinase and its recognition site – locus of crossover in P1 bacteriophage (loxP), has been widely employed to target genes at certain timing or in desired cell types [105]. Cre recombinase belongs to the integrase superfamily and catalyzes a site-specific recombination at the recognition sites [106]. The recognition site, loxP, contains two 13-bp palindromic sequences between which an 8-bp non-palindromic sequence is located **(Figure 8a)**. Depending on the orientation and the location of the loxP sites on the DNA sequence, Cre recombinase gives rise to different genetic recombination results **(Figure 8b)**. Tamoxifen (Tmx) induction is one of the most common strategies for conditional gene targeting in mice [107]. In this strategy, Cre recombinase is fused with the human estrogen receptor (ER), which consists of a mutated ligand-binding domain [108].

The Cre-ER^T chimeric protein has physical interaction with the heat shock protein 90 (Hsp90) and this protein complex is localized in cytoplasm [107]. Once 4-hydroxytamoxifen (4-OHT), an active metabolite of Tmx, binds to the Cre-ER^T protein, HSP90 disassociates from Cre-ER^T protein. Subsequently, the translocation of Cre-ER^T protein into nucleus occurs, resulting in Cre-mediated recombination **(Figure 9a, 9b)**. It has been shown that the efficiency of a new version of the fusion protein, Cre-ER^{T2}, is higher than Cre-ER^T protein upon 4-OHT induction [109]. Therefore, using Cre-ER^{T2}/loxP system to achieve conditional gene targeting is currently more preferable.

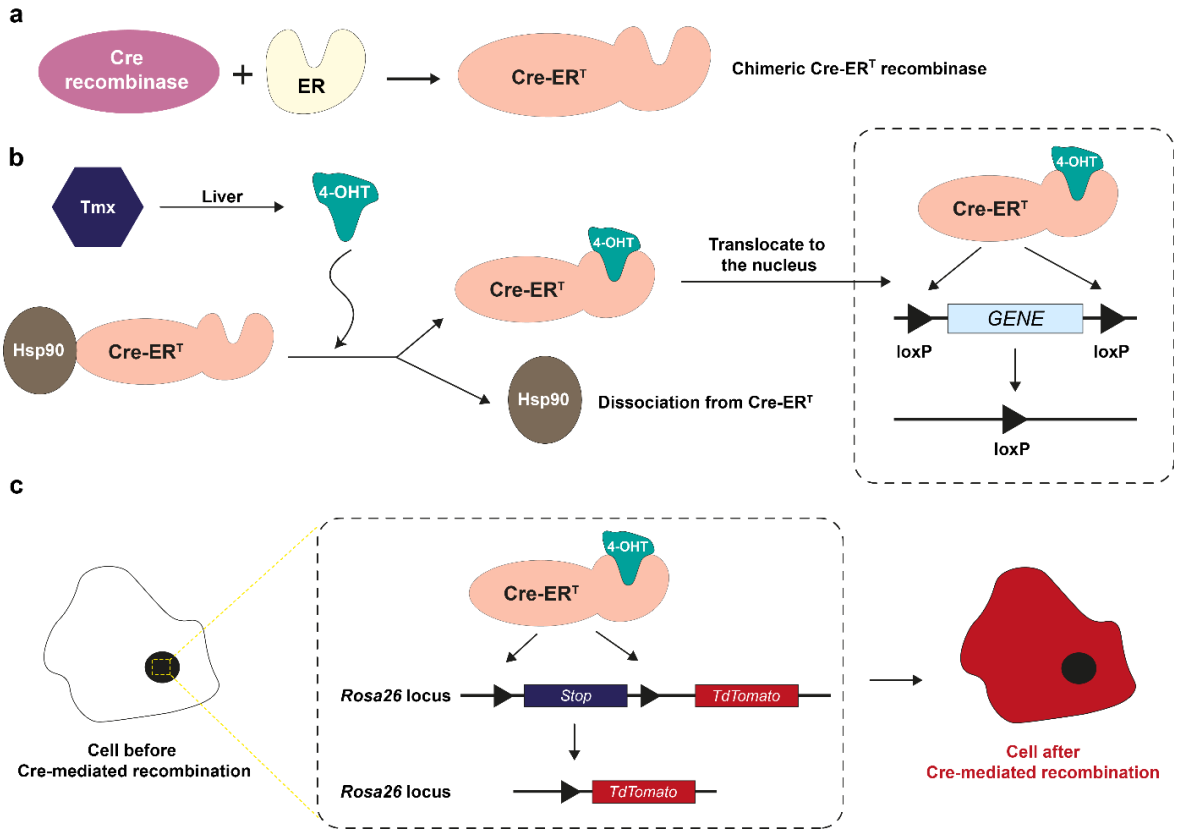

Figure 9. Mechanism of the Cre-ER^T/loxP system. a, Schematic drawing of the fusion between Cre recombinase and the human estrogen receptor protein (ER). **b,** Schematic illustration of the inducible gene-ablation upon administration of tamoxifen (Tmx). Tmx is firstly metabolized in the liver to form 4-hydroxyltamoxifen (4-OHT) [110]. Once 4-OHT binds to the chimeric Cre-ER^T recombinase, HSP90 dissociates from the Cre-ER^T recombinase. The recombinase can then translocate to the nucleus, leading to the Cre-mediated gene-excision. **c,** Schematic illustration of the cell labeling by a reporter protein, namely tandem dimer tomato protein (TdTomato). Before the cell receives 4-OHT, the fluorescence protein – TdTomato is

not translated due to the Stop codon on the *Rosa26* locus. Upon binding of 4-OHT to the Cre-ER^{T} recombinase, the Stop codon is deleted and the TdTomato protein is present in the cell. Abbreviations: Cre, Causes recombination. LoxP, Locus of crossover in P1 bacteriophage. Hsp90, Heat shock protein 90.

1.3.3.2 Inducible cell-specific knockout mouse models

As previously mentioned in section 1.1.2, the lungs comprise of several structurally and functionally different cell types. Therefore, to investigate tissue- or cell-specific genetic gain or loss of function in the lung, many transgenic mouse strains, carrying a CreER^{T2} gene restrained with a cell-specific promoter element, have been generated [111] **(Table 2).** Besides, these animal strains can be further crossbred with mice carrying a loxP-floxed Stop codon and a gene encoding reporter proteins, such as green fluorescence protein (GFP) or tandem dimer tomato protein (TdTomato), on the *Rosa26* locus [112]. This is beneficial for the researchers to trace where Cre-mediated recombination occurs upon the administration of Tmx **(Figure 9)**.

Table 2. Example of inducible cell-specific Cre-expressing mouse line.

Targeted lung cell type	Mouse strain	MGI-ID
AEC2	*Sftpc*^{tm1} (Cre/ER^{T2})^{Blh}	5305340
AEC1	*Aqp5*$^{tm1.1}$ (Cre/ER^{T2})^{Ptch}	6741118
Club cell	Tg(*Scgb1a1*-Cre/ER^{T2})^{5Nar}	5898277
Basal cell	*Krt5*$^{tm1.1}$ (Cre/ER^{T2})^{Blh}	5305438
Smooth muscle cell	Tg(*Acta2*-Cre/ER^{T2})^{12Pcn}	3831907
Endothelial cell	Tg(*Tek*-Cre/ER^{T2})^{1Arnd}	2450312
Fibroblast	Tg(*Col1a2*-Cre/ER$^{T,-ALPP}$)^{7Cpd}	3785760
Macrophage	*Cx3cr1*$^{tm2.1}$(Cre/ER^{T2})^{Jung}	5467985
Myeloid cell	*Lyz2*^{tm1}(Cre/ER^{T2})^{Grtn}	6114757
T lymphocyte	Tg(*Cd4*-Cre/ER^{T2})^{11Gnri}	5493114

Abbreviations: MGI-ID, Mouse genome informatics – identity number. AEC2, Alveolar type 2 epithelial cell. AEC1, Alveolar type 1 epithelial cell.

1.4 Aims of the current study

COPD is still a severe medical condition and currently among the leading causes of morbidity and mortality worldwide [113]. Tremendous efforts have been made to elucidate the molecular mechanisms of COPD to prevent its development, stop progression or to implement a novel therapeutic approach for patients with COPD.

Previously, Seimetz *et al*. identified iNOS as a key enzyme leading to the development of CS-induced PH and emphysema in mice [44]. The vast amount of NO produced by iNOS reacts with O_2^-, resulting in $ONOO^-$ generation and subsequent 3-NT formation. In the respective study, the expression of iNOS was significantly upregulated in pulmonary vessels of mice exposed to CS for 3 and 8 months, but not in alveolar septa and bronchi. Moreover, significant structural alterations in pulmonary vasculature, leading to PH, were shown in mice after 3 months of CS exposure. However, emphysema development required 8 months of CS exposure. Namely, the profound iNOS upregulation in pulmonary vessels suggests not only to foster pulmonary vascular remodeling but maybe also promotes emphysema development.

Seimetz *et al*. further proved that bone-marrow-derived (BMD) iNOS is crucial for PH development, whereas CS-induced emphysema was dependent on non-bone-marrow-derived (NBMD) iNOS [44]. In agreement with this finding, a recently article published by Gredic *et al*. uncovered that myeloid cell-specific *iNos*-deletion protects mice from CS-induced PH, but not from CS-induced emphysema [114]. Hence, the contribution of increased iNOS expression in the lung vascular NBMD cell types to CS-induced emphysema development remains unresolved.

Against this background, I hypothesized that iNOS-deletion in a vascular NBMD cell type, namely pulmonary artery smooth muscle cells (PASMCs) protects mice from CS-induced emphysema development.

Thus, in the scope of this work, the following aspects were closely investigated **(Figure 10)**:

1. The iNOS expressions in human PASMCs upon CS extract (CSE) exposure.
2. Intracellular nitric oxide production in human PASMCs and PASMCs isolated from wildtype (*Wt*) and *iNos*-knockout mice ($iNos^{-/-}$) upon CSE exposure.
3. The effect of CSE exposure in NBMD cells isolated from *Wt* and $iNos^{-/-}$ mice.

4. 3-NT levels and the localization in thuman lungs from healthy donors, smokers without and with COPD.
5. The impact of *Acta2*$^{+}$ cell-specific *iNos*-deletion on the pathogenesis of CS-induced PH and emphysema. In this regard, transgenic mice carried a loxP-flanked *iNos* transgene (*iNos*$^{flox/flox}$), a tamoxifen-dependent inducible Cre recombinase gene expressed under the *Acta2* gene promoter (*Acta2*-Cre/ER^{T2}), and a loxP-flanked Stop codon followed by a gene encoding reporter proteins, tandem dimer tomato protein (TdTomato) on the *Rosa26* locus were employed (See section 2.2.3). Prior to 3 and 8 months of room air (RA) or CS exposure, the mice received tamoxifen (+Tmx) or its vehicle control (+Vehicle).

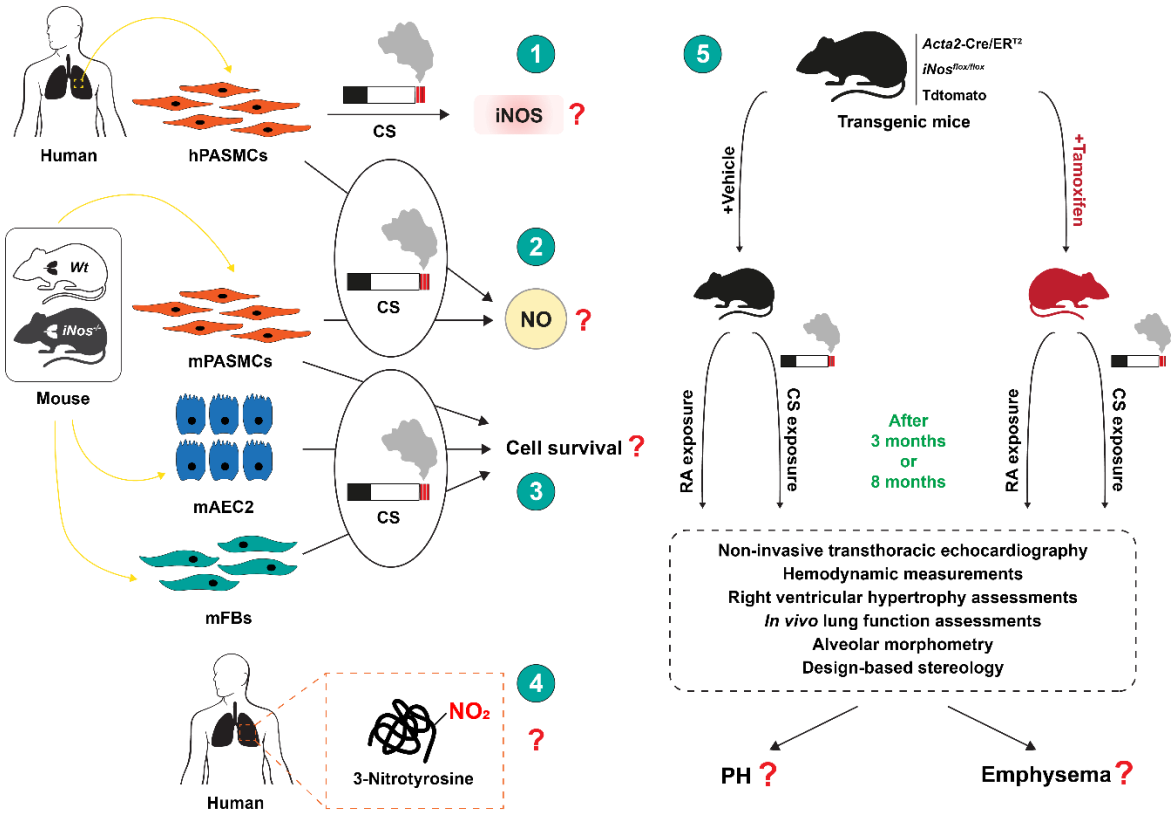

Figure 10. Schematic illustration of the experimental design and the working hypothesis.
Abbreviation: hPASMC, Human pulmonary artery smooth muscle cell. CS, Cigarette smoke. iNOS, Inducible nitric oxide synthase. *Wt*, Wildtype. *iNos*$^{-/-}$, *iNos* knockout. mPASMC, mouse pulmonary artery smooth muscle cell. NO, Nitric oxide. mAEC2, Mouse alveolar type 2 epithelial cell. mFB, Mouse fibroblast. RA, Room air. PH, Pulmonary hypertension.

2. Materials and Methods

All experiments were performed by myself, if not stated otherwise.

2.1 Materials

2.1.1 Equipment

Name	Manufacturer
Automated capillary-based protein immunoassay (Jess)	*ProteinSimple, Bio-Techne Corporation, Minneapolis, MN, USA*
Automated microtome (Leica RM 2165)	*Leica Microsystems GmbH, Wetzlar, Germany*
Balance for substances (Mettler Toledo PB303 Delta Range®)	*Mettler Toledo GmbH, Greifensee, Switzerland*
Cell incubator HERAcell 150	*Thermo Fisher Scientific Inc. Waltham, MA, USA*
Centrifuge Mikro 200R	*Andreas Hettich GmbH & Co. KG, Tuttlingen, Germany*
ChemiDocTM Touch Imaging System	*Bio-Rad Laboratories GmbH, Hercules, CA, USA*
ChemiDocTM XRS+	*Bio-Rad Laboratories GmbH, Hercules, CA, USA*
Cigarette smoke generator	*Burghart GmbH, Wedel, Germany*
Confocal microscope SP8	*Leica Microsystems GmbH, Wetzlar, Germany*
Cooling Plate EG 1150C	*Leica Microsystems GmbH, Wetzlar, Germany*

Culture Hood	*Heraeus GmbH, Hanau, Germany*
Flattening bath for paraffin sections (Leica HI 1210)	*Leica Microsystems GmbH, Wetzlar, Germany*
FlexiVent mechanical ventilator equipped with FX2 module and data-acquisition system	*SCIREQ Scientific Respiratory Equipment Inc., Montreal, Canada*
Heating Block	*VWR International GmbH, Bruchsal, Germany*
Heating chamber	*Memmert, Schwabach, Germany*
Heating Plate Hi 1220	*Leica Microsystems GmbH, Wetzlar, Germany*
Hotplate/Stirrer (371)	*VWR International GmbH, Bruchsal, Germany*
Ice flake machine (Icematic F100 Compact)	*Castelmac SPA, Castelfranco, Italy*
IncuCyte ZOOM	*Essen BioScience, Ltd. Ann Arbor, MI, USA*
InnoScan is900	*Innopsys, Chicago, IL, USA*
Ismatec® roller-pump	*Cole-Parmer GmbH, Wertheim Germany*
Laser microdissection system (LMD6000)	*Leica Microsystems GmbH, Wetzlar, Germany*
Light microscope (DMLA)	*Leica Microsystems GmbH, Wetzlar, Germany*
Low Voltage Power Supplies Power pack P25T	*Biometra GmbH, Jena, Germany*
LUNA-FX7 Automated Cell Counter	*BioCat GmbH, Heidelberg, Germany*

Microplate reader Infinite M200	*Tecan Trading AG, Männedorf, Switzerland*
Mini-PROTEAN® electrophoresis cells	*Bio-Rad Laboratories GmbH, Hercules, CA, USA*
MiniVent type 845 Hugo Sachs	*Hugo Sachs Elektronik – harvard Apparatus GmbH, March-Hugstetten, Germany*
Multimode microplate reader Infinite 200 PRO	*Tecan Trading AG, Männedorf, Switzerland*
Multimode microplate reader Spark®	*Tecan Trading AG, Männedorf, Switzerland*
NanoDrop (ND-1000)	*Kisker-Biotech, Steinfurt, Germany*
Neubauer counting chamber	*Paul Marienfeld GmbH & Co. KG, Lauda-Königshofen, Germany*
Paraffin cooling station Leica EG 1150C	*Leica Microsystems GmbH, Wetzlar, Germany*
Paraffin embedding station Leica EG 1140H	*Leica Microsystems GmbH, Wetzlar, Germany*
PCR Plate sealer PX1	*Bio-Rad Laboratories GmbH, Hercules, CA, USA*
pH meter-766 Calimatic	*Knick Elektronische Messgeraete GmbH & Co. KG, Berlin, Germany*
PowerLab system	*ADInstruments GmbH, Spechbach, Germany*
Precellys® 24 bead beating Tissue Homogenizer	*Thermo Fisher Scientific Inc. Waltham, MA, USA*
QIAxcel Advanced System	*Qiagen GmbH, Hilden, Germany*

Real-Time polymerase chain reaction (PCR) Detection System (CFX Connect™)	*Bio-Rad Laboratories GmbH, Hercules, CA, USA*
Rectal thermometer	*Indus Instruments, Houston, TX, USA*
Roller mixer LLG-uniROLLER 10	*Lab Logistics Group GmbH, Meckenheim, Germany*
Rotary microtome cryostat (CM1520)	*Leica Microsystems GmbH, Wetzlar, Germany*
Shaking table Swip	*Edmund Bühler Gmbh, Bodelshausen, Germany*
SPR-671 Mikro-Tip® mouse pressure catheter, REF 8406719	*Millar Instruments, Houston, TX, USA*
Table Centrifuge Mikro 200R	*Andreas Hettich GmbH & Co. KG, Tuttlingen, Germany*
Thermocycler, T3000	*Biometra GmbH, Jena, Germany*
Thermocycler, Tpersonal	*Biometra GmbH, Jena, Germany*
Thermoregulation plate TCAT-2LV controller	*Physitemp Instruments Inc., Clifton, NJ, USA*
Trans-Blot® Turbo Semi-dry System	*Bio-Rad Laboratories GmbH, Hercules, CA, USA*
Ultrapure Milli-Q®	*Millipore, Merck KGaA, Darmstadt, Germany*
Vevo® 2100 high-resolution Imaging System	*FUJIFILM VisualSonics Inc, Toronto, Canada*
Vibratome (Microm HM650V)	*Thermo Fisher Scientific Inc. Waltham, MA, USA*

Vortexer MS1 Minishaker	*IKA GmbH, Staufen, Germany*
Water bath	*Memmert GmbH&Co.KG, Schwabach, Germany*

2.1.2 Chemicals and consumables

Name	**Manufacturer**
12-230 kDa Separation Module, 8 x 25 capillary cartridges (SM-W004)	*ProteinSimple, Bio-Techne Corporation, Minneapolis, MN, USA*
2-Mercaptoethanol (4227.3)	*Carl Roth GmbH&Co.KG, Karlsruhe, Germany*
50 bp DNA ladder (10416014)	*Thermo Fisher Scientific Inc. Waltham, MA, USA*
6X DNA Gel Loading Dye (R0611)	*Thermo Fisher Scientific Inc. Waltham, MA, USA*
Acetone (32201)	*Merck KGaA, Darmstadt, Germany*
Adenosine (A9251)	*Merck KGaA, Darmstadt, Germany*
Agarose (11406)	*SERVA Electrophoresis GmbH, Heidelberg, Germany*
Agarose, low-gelling temperature (6351)	*Carl Roth GmbH&Co.KG, Karlsruhe, Germany*
Agarose, low-gelling temperature (A9045)	*Merck KGaA, Darmstadt, Germany*
AlamarBlue cell viability reagent (A50101)	*Thermo Fisher Scientific Inc. Waltham, MA, USA*
Alkaline Phosphatase (AP) Polymer System (POLAP-100)	*Zytomed Systems GmbH, Berlin, Germany*
Amersham ECL Plus Western Blotting Detections System (29018903)	*GE Healthcare, Munich, Germany*

Ammonium persulfate (APS, A3678)	*Sigma-Aldrich, Merck KGaA, Darmstadt, Germany*
Doubly distilledwater (3478.1)	*Carl Roth GmbH&Co.KG, Karlsruhe, Germany*
Antibody Diluent (ZUC025-100)	*Zytomed Systems GmbH, Berlin, Germany*
Automatic pipettes (100-1000 µl, 10-100 µl, 1-10 µl)	*Eppendorf AG, Hamburg, Germany*
Background Punisher (BP974)	*Biocare Medical LLC, Pacheco, USA*
Bovine Serum Albumin (BSA, A7030)	*Merck KGaA, Darmstadt, Germany*
Cannulas (16G, 18G)	*BD Biosciences, San Jose, CA, USA*
CAT Hematoxylin (CATHE-M)	*Biocare Medical LLC, Pacheco, USA*
Cell culture dishes (35er, 60er)	*Sarstedt AG&Co.KG, Nümbrecht, Germany*
Cell culture plates (6, 12, 24, 96 well)	*Greiner Bio-One GmbH, Frickenhausen, Germany*
Cell lysis buffer (9803S)	*Cell Signaling Technology Inc., Danvers, MA, USA*
Cell scrapers	*Greiner Bio-One GmbH, Frickenhausen, Germany*
Cell strainers (40 µl, 100 µm)	*Greiner Bio-One GmbH, Frickenhausen, Germany*
Cellulose swabs Pur-Zellin®	*Paul Hartmann AG, Heidenheim, Germany*
Cigarettes 3R4F	*Kentucky Tobacco Research & Development Center, Lexington, KY, USA*
Citrate buffer	*Biocare Medical LLC, Pacheco, CA, USA*
Collagenase (C9891)	*Merck KGaA, Darmstadt, Germany*
Collagenase from *Clostridium histolyticum* (C5138)	*Merck KGaA, Darmstadt, Germany*
Combi-Tips advanced (5 ml, 10 ml, 25 ml)	*Eppendorf AG, Hamburg, Germany*

Comp-Beads	*BD Biosciences, San Jose, CA, USA*
Conical centrifuge tubes (15 ml, 50 ml)	*Greiner Bio-One GmbH, Frickenhausen, Germany*
Corn oil (C8267-500ML)	*Sigma-Aldrich, Merck KGaA, Darmstadt, Germany*
Coverslips 24x36 mm	*Menzel GmbH&Co.KG, Braunschweig, Germany*
Cryo Tubes	*Sarstedt AG&Co.KG, Nümbrecht, Germany*
Crystal violet (C3886)	*Sigma-Aldrich, Merck KGaA, Darmstadt, Germany*
Cytometer Setup and Tracking beads	*BD Biosciences, Heidelberg, Germany*
DAF-FM DA (D23844)	*Invitrogen, Thermo Fisher Scientific Inc. Waltham, MA, USA*
Dako Fluorescence Mounting Medium	*Agilent Technologies Inc., Santa Clara, CA, USA*
DAPI (4′,6-Diamidino-2-phenyl-indol – dihydrochlorid; D9542)	*Merck KGaA, Darmstadt, Germany*
DC™ Protein Assay (5000112)	*Bio-Rad Laboratories GmbH, Hercules, CA, USA*
Dimethylsulfoxide (DMSO, D4540)	*Merck KGaA, Darmstadt, Germany*
Disodiumhydrogenphosphate dihydrate (Na_2HPO_4,106580)	*Merck KGaA, Darmstadt, Germany*
Distilled Water (3478.1)	*Carl Roth GmbH&Co.KG, Karlsruhe, Germany*
Dispase (354235)	*Corning Inc., New York, NY, USA*
Distilled Water (dH2O, DNase-/RNase-free, 10977023)	*Invitrogen, Thermo Fisher Scientific Inc. Waltham, MA, USA*
DIVA Decloaker (DV2004MX)	*Biocare Medical LLC, Pacheco, CA, USA*
Dulbecco's Modified Eagle Medium (DMEM, 31885023)	*GIBCOTM, Thermo Fisher Scientific Inc. Waltham, MA, USA*

DNase (04536282001)	*Roche Diagnostics GmbH, Mannheim, Germany*
Dulbecco's phosphate-buffered saline (DPBS, P04-53500)	*PAN-Biotech GmbH, Aidenbach, Germany*
Electronic animal identification reusable implanter needles (mini)	*Planet-ID GmbH, Essen, Germany*
Embedding cassettes	*Leica Microsystems GmbH, Wetzlar, Germany*
Enzyme-free cell dissociation buffer (13151014)	*GIBCOTM, Thermo Fisher Scientific Inc. Waltham, MA, USA*
Eosin Y, alcoholic (6766007)	*Thermo Fisher Scientific Inc. Waltham, MA, USA*
Ethanol (pure) for molecular biology (108543)	*Merck KGaA, Darmstadt, Germany*
Ethanol 100% (27694)	*Otto Fischar GmbH, Saarbrücken, Germany*
Ethanol 70% (ETO-5000-70-1)	*SAV Liquid Production GmbH, Flintsbach a. Inn, Germany*
Ethanol 96% (27695)	*Otto Fischar GmbH, Saarbrücken, Germany*
Ethylenediaminetetraacetic acid (EDTA, 8043)	*Carl Roth GmbH&Co.KG, Karlsruhe, Germany*
Fetal bovine serum (FBS, F0804)	*Merck KGaA, Darmstadt, Germany*
Fibronectin (F1141)	*Merck KGaA, Darmstadt, Germany*
Filtered tips (10 µl, 100 µl, 1000 µl)	*Nerbe plus GmbH&Co.KG, Winsen, Germany*
Filtopur S 0.2 µm (83.1826.001)	*Sarstedt AG&Co.KG, Nümbrecht, Germany*
Fluoro Care Anti-Fade Mountant (FP 001 G10)	*Biocare Medical LLC, Pacheco, USA*
Formaldehyde (3.5 – 3.7%, stabilized with methanol, 27244)	*Otto Fischar GmbH, Saarbrücken, Germany*
GeneRuler™ 100 bp DNA Ladder (SM0313)	*Thermo Fisher Scientific Inc. Waltham, MA, USA*
Glass bottles, beakers, cylinders	*DURAN Group Holding GmbH, Wertheim, Germany*

Glass bottles, beakers, cylinders	*VWR International LLC, Bruchsal, Germany*
Glass bottles, beakers, cylinders	*Fisher Scientific GmbH, Schwerte, Germany*
Glass slides with polyethylene naphthalate membrane (11505158)	*Leica Microsystems GmbH, Wetzlar, Germany*
Gloves (Nitra-Tex®)	*Ansell Ltd., Tamworth, UK*
Glycine (A1067)	*AppliChem GmbH, Darmstadt, Germany*
Hand towels	*Essity Hygiene and Health, Stockholm, Sweden*
Hank's Balanced Salt Solution (HBSS, 14025050)	*GIBCOTM, Thermo Fisher Scientific Inc. Waltham, MA, USA*
Heparin (Heparin-Natrium 5000 I.E.)	*Ratiopharm GmbH, Ulm, Germany*
Histological glass slides 25x75x1 mm (SuperFrost UltraPlus®)	*R. Langenbrinck GmbH, Emmendingen, Germany*
Hoechst-33342 (62249)	*Invitrogen, Thermo Fisher Scientific Inc. Waltham, MA, USA*
Hydrochloride (HCl, 37%, 4625.1)	*Carl Roth GmbH&Co.KG, Karlsruhe, Germany*
iScript complementary DNA (cDNA) Synthesis Kit (1708890)	*Bio-Rad Laboratories GmbH, Hercules, CA, USA*
Isoflurane (HDG9623)	*Baxter Deutschland GmbH, Unterschleissheim, Germany*
Isopropyl-alcohol (99.8%, 190764)	*Merck KGaA, Darmstadt, Germany*
iTaq Universal SYBR® Green Supermix (1725124)	*Bio-Rad Laboratories GmbH, Hercules, CA, USA*
Ketamine (Ursotamin)	*Serumwerk Bernburg AG, Bernburg, Germany*
Laemmli Sample Buffer 4X (1610747)	*Bio-Rad Laboratories GmbH, Hercules, CA, USA*
L-Glutamine (P04-80100)	*GIBCOTM, Thermo Fisher Scientific Inc. Waltham, MA, USA*

Lumox® multiwell, 96-well	*Sarstedt AG&Co.KG, Nümbrecht, Germany*
MaxBlock™ autofluorescence reducing reagent kit	*Maxvision Biosciences Inc., Washington, USA*
Medical adhesive bands (2.5 cm/9.2 m)	*3M Health Care, St.Paul, MN, USA*
Medium 199 (M199, 31150022)	*GIBCOTM, Thermo Fisher Scientific Inc. Waltham, MA, USA*
Methanol (99.8%, 32213)	*Merck KGaA, Darmstadt, Germany*
Micro tubes (0.5 ml, 1.5 ml, 2.0 ml)	*Sarstedt AG&Co.KG, Nümbrecht, Germany*
Microscope slide box ROTILABO® (K335.1)	*Carl Roth GmbH&Co.KG, Karlsruhe, Germany*
Microtome blades (MX35 Premier)	*Thermo Fisher Scientific Inc. Waltham, MA, USA*
Mounting medium (Pertex®, 41-4012-00)	*Medite GmbH, Burgdorf, Germany*
Multipette E3x	*Eppendorf AG, Hamburg, Germany*
Multiplate™ PCR Plate 96-Well, clear	*Bio-Rad Laboratories GmbH, Hercules, CA, USA*
Needles (BD Microlance 3®) (18 G /1.2 mm x 40 mm, 20 G /0.9 mm x 40 mm, 26G /0.45 mm x 13 mm)	*Becton Dickinson GmbH, Heidelberg, Germany*
N6-(1-Iminoethyl)-L-lysine (L-NIL, 80310)	*Cayman Chemical Co., Ann Arbor, MI, USA*
Nile red (N3013)	*Merck KGaA, Darmstadt, Germany*
Nitrotyrosine ELISA kit (17-376)	*Merck KGaA, Darmstadt, Germany*
Non-tissue culture treated Petri dishes	*Sarstedt AG&Co.KG, Nümbrecht, Germany*
Normocin™ (ant-nr-1)	*InvivoGen, Toulouse, France*
Parafilm®	*Merck KGaA, Darmstadt, Germany*
Paraformaldehyde (PFA, sc-281692)	*Santa Cruz Biotechnology, Inc., Dallas, TX, USA*

Paraplast Plus® for tissue embedding (P3683)	*Merck KGaA, Darmstadt, Germany*
Paveron N (A03AD01)	*Linden Arzneimittel GmbH, Heuchelheim, Germany*
Penicillin/Streptomycin (15070-063)	*GIBCO™, Thermo Fisher Scientific Inc. Waltham, MA, USA*
Phenylmethansulfonylfluorid (PMSF, P7626)	*Merck KGaA, Darmstadt, Germany*
Phenylmethylsulfonyl Fluoride (PVDF)-membrane	*Pall Deutschland Holding GmbH & Co. KG, Dreieich, Germany*
Pierce™ 20X Borate Buffer (SB buffer, 28341)	*Thermo Fisher Scientific Inc. Waltham, MA, USA*
Polystyrene round-bottom tubes with cell strainer cap (5 ml)	*Greiner Bio-One GmbH, Frickenhausen, Germany*
Potassium chloride (KCl, 6781.1)	*Merck KGaA, Darmstadt, Germany*
Potassiumdihydrogenphosphate (KH_2PO_4, 104873)	*Merck KGaA, Darmstadt, Germany*
Povidone-iodine solution (Braunoderm®)	*B.Braun Melsungen AG, Melsungen, Germany*
Precision Plus Protein Dual Color Standards (1610374)	*Bio-Rad Laboratories GmbH, Hercules, CA, USA*
Primers (listed in the section 2.1.5)	*Metabion International AG, Planegg, Germany*
Propidium Iodide (P3566)	*Invitrogen, Thermo Fisher Scientific Inc. Waltham, MA, USA*
Protease-Inhibitor-Cocktail cOmplete™ Mini EDTA-free	*Roche Diagnostics GmbH, Mannheim, Germany*
Proteinase K Novocastra™ (RE7160-K)	*Leica Microsystems GmbH, Wetzlar, Germany*
Red blood cell (RBC) lysis buffer (BD Pharm Lyse™, 555899)	*BD Biosciences, Heidelberg, Germany*
RePlex™ Module (RP-001)	*ProteinSimple, Bio-Techne Corporation, Minneapolis, MN, USA*

Resorcin-Fuchsin (2E-030)	*Waldeck GmbH&Co.KG, Münster, Germany*
RNA lysis buffer – RLT buffer (79216)	*Qiagen GmbH, Hilden, Germany*
RNeasy Mini Kit (74106)	*Qiagen GmbH, Hilden, Germany*
Rodent Decloaker,10X (RD913)	*Biocare Medical LLC, Pacheco, USA*
RPMI medium 1640 (P04-16500)	*PAN-Biotech GmbH, Aidenbach, Germany*
Saline solution (0,9% NaCl; 3570160)	*B.Braun Melsungen AG, Melsungen, Germany*
Serological pipette (5 ml, 10 ml, 25 ml, 50 ml)	*BD Falcon, Heidelberg, Germany*
Skimmed milk powder (T145.3)	*Carl Roth GmbH&Co.KG, Karlsruhe, Germany*
Smooth Muscle Cell Basal Medium 2 (C-22262)	*Promo Cell GmbH, Heidelberg, Germany*
Smooth Muscle Cell Growth Medium 2 (C-22062)	*Promo Cell GmbH, Heidelberg, Germany*
Smooth Muscle Supplement 2 mix (C-39267)	*Promo Cell GmbH, Heidelberg, Germany*
Sodium dodecyl sulfate (SDS, AM9820)	*Invitrogen, Thermo Fisher Scientific Inc. Waltham, MA, USA*
Sodium hydroxide (NaOH, 06203)	*Sigma-Aldrich, Merck KGaA, Darmstadt, Germany*
Surgical instruments	*Fine Science Tools GmbH, Heidelberg, Germany*
SYBR® Safe DNA gel stain (S33102)	*Invitrogen, Thermo Fisher Scientific Inc. Waltham, MA, USA*
Syringes (Injekt®-F) (1 ml, 2 ml, 5 ml, 20 ml)	*B.Braun Melsungen AG, Melsungen, Germany*
Tamoxifen (T5648-1G)	*Sigma-Aldrich, Merck KGaA, Darmstadt, Germany*
Tetramethylethylenediamine (TEMED, 2367.3)	*Carl Roth GmbH&Co.KG, Karlsruhe, Germany*

TGX FastCast Kit (12% gels, 1610185)	*Bio-Rad Laboratories GmbH, Hercules, CA, USA*
Thread, black no.16	*Coats GmbH, Kenzingen, Germany*
Tips for automatic pipettes (200 µl, 1000 µl, 10 µl)	*Sarstedt AG&Co.KG, Nümbrecht, Germany*
Tissue-Tek® O.C.T.™	*Sakura Finetek Germany GmbH, Staufen im Breisgau, Germany*
Total protein assay (DM-TP01)	*ProteinSimple, Bio-Techne Corporation, Minneapolis, MN, USA*
Trifluoroacetic acid aqueous solution (T6508)	*Sigma-Aldrich, Merck KGaA, Darmstadt, Germany*
TRIS (4855.2)	*Carl Roth GmbH&Co.KG, Karlsruhe, Germany*
TRIS-Base (10708976001)	*Sigma-Aldrich, Merck KGaA, Darmstadt, Germany*
Tris-buffered saline 20x (TBS, ZUC052-500)	*Zytomed Systems GmbH, Berlin, Germany*
TRIS-HCl (9090.2)	*Carl Roth GmbH&Co.KG, Karlsruhe, Germany*
Triton X-100 (X100)	*Merck KGaA, Darmstadt, Germany*
Trypsin/EDTA (10x, P10-024100)	*PAN-Biotech GmbH, Aidenbach, Germany*
Tween® 20 (P1379)	*Merck KGaA, Darmstadt, Germany*
Warp Red Chromogen Kit (WR 806)	*Biocare Medical LLC, Pacheco, USA*
Water, sterile (00088992)	*B.Braun Melsungen AG, Melsungen, Germany*
Whatman Gel Blotting Paper	*GE Healthcare, Marlborough, USA*
Xylazin 20 mg/ml	*Serumwerk, Bernburg, Germany*
Xylol (9713.2)	*Carl Roth GmbH&Co.KG, Karlsruhe, Germany*

2.1.3 Software

Name	Manufacturer
Adobe Illustrator	*Adobe Inc., Mountain View, CA, USA*
CFX manager	*Bio-Rad Laboratories GmbH, Hercules, CA, USA*
Compass for SimpleWestern	*ProteinSimple, Bio-Techne Corporation, Minneapolis, MN, USA*
FlexiVent software	*SCIREQ Scientific Respiratory Equipment Inc., Montreal, Canada*
FlowJo	*BD Biosciences, Heidelberg, Germany*
GraphPad Prism Version 9	*GraphPad Software, Inc., La Jolla, CA, USA*
Image Lab Version 4.1	*Bio-Rad Laboratories GmbH, Hercules, CA, USA*
IncuCyte ZOOM software	*Essen BioScience, Ltd. Ann Arbor, MI, USA*
Leica Application Suit	*Leica Microsystems GmbH, Wetzlar, Germany*
LabChart 7	*AD Instruments GmbH, Spechbach, Germany*
NanoDrop Software	*Kisker Biotech GmbH&Co.KG, Steinfurt, Germany*
PowerLab data acquisition system (MPVS-Ultra Single Segment Foundation System)	*AD Instruments GmbH, Spechbach, Germany*
Qwin software	*Leica Microsystems GmbH, Wetzlar, Germany*
R software	*The R Foundation, Iowa City, IA, USA*

Stereology software newCAST	*Visiopharm, Hørsholm, Denmark*
Microsoft office 2016	*Microsoft Corporation, Redmond, WA, USA*
Tecan i-control	*Tecan Trading AG, Männedorf, Switzerland*
VevoLAB version 5.6.1	*FUJIFILM VisualSonics Inc, Toronto, Canada*

2.1.4 Animals

C57BL/6J	*The Jackson Laboratory, Bar Harbor, ME, USA (MGI-ID: 3028467)*
B6.129P2-*Nos2*^{tm1Lau}/J	*The Jackson Laboratory, Bar Harbor, ME, USA. (MGI-ID: 2163455)*
STOCK; *Nos2*$^{tm2904.1Arte}$ Tg(CAG-flpe)2Arte Tg(Acta2-CreER^{T2})12Pcn Gt(ROSA)26Sor$^{tm9(CAG-tdTomato)Hze}$/J	*Bred in house; obtained by crossing m*ouse *strain 1 (customized by Taconic Biosciences GmbH, Leverkusen, Germany): Nos2$^{tm2904.1Arte}$ Tg(CAG-flpe)2Arte , mouse strain 2 (offered by Professor Saverio Bellusci's group): Tg(Acta2-Cre/ER^{T2})12Pcn (MGI-ID:3831907) and mouse strain 3(offered by Professor Saverio Bellusci's group): Gt(ROSA)26Sor$^{tm9(CAG-tdTomato)Hze}$/J (MGI-ID:3809523)*

2.1.5 Primer sequences

2.1.5.1 Genotyping primers specific for Mus musculus genes

Gene	Primer sequence	Product size (bp)
Nos2_5905	F: 5'-GGTGGATCTCTGTGAGTTCAGG-3' R: 5'-AGGCACACACACAAGTTCAGG-3'	*Wt*: 211 *Tg*: 368
Nos2_5906	F: 5'-ATATTCTGCCTAGACGGTGTGA-3' R: 5'-TCAGTGACGACGATCTCCTTAAA-3'	*Wt*: 217 *Tg*: 309
Acta2-Cre/ER^{T2}	F: 5'-ATTTGCCTGCATTACCGGTC-3' R: 5'-ATCAACGTTTTGTTTTCGGA-3'	349
Tdtomato-Wt	F: 5´-CCGAAAATCTGTGGGAAGTC-3´ R: 5´-AAGGGAGCTGCAGTGGAGTA-3´	297
Tdtomato-flox/flox	F: 5'-CTGTTCCTGTACGGCATGGG-3' R: 5'-GGCATTAAAGCAGCGTATCC-3'	196

2.1.5.2 RT-qPCR Primers specific for Homo sapiens genes

Gene	Primer sequence	Product size (bp)
NOS2	F: 5'- TTCAGTATCACAACCTCAGCAAG-3' R: 5'- TGGACCTGCAAGTTAAAATCCC-3'	207
B2M	F: 5'- GCCGTGTGAACCATGTGACT-3' R: 5'- GCAAGCAAGCAGAATTTGGA-3'	128

2.1.6 Antibodies

Name	Manufacturer
Anti-mouse secondary Horseradish-peroxidase-labeled antibody (042-205)	*ProteinSimple, Bio-Techne Corporation, Minneapolis, MN, USA*

Anti-rabbit secondary Horseradish-peroxidase-labeled antibody (042-206)	*ProteinSimple, Bio-Techne Corporation, Minneapolis, MN, USA*
Donkey anti-mouse IgG (H+L) Highly Cross-Adsorbed Secondary Antibody, Alexa Fluor™ Plus 647 (A32787)	*Invitrogen, Thermo Fisher Scientific Inc. Waltham, MA, USA*
Donkey anti-rabbit IgG (H+L) Highly Cross-Adsorbed Secondary Antibody, Alexa Fluor™ Plus 488 (A32790)	*Invitrogen, Thermo Fisher Scientific Inc. Waltham, MA, USA*
Donkey anti-goat IgG (H+L) Highly Cross-Adsorbed Secondary Antibody, Alexa Fluor™ Plus 555 (A32816)	*Invitrogen, Thermo Fisher Scientific Inc. Waltham, MA, USA*
Horseradish-peroxidase-labeled anti-mouse secondary antibody (W4011)	*Promega GmbH, Madison, WI, USA*
Horseradish-peroxidase-labeled anti-rabbit secondary antibody (W4021)	*Promega GmbH, Madison, WI, USA*
Mouse anti-alpha smooth muscle actin antibody (A5228)	*Sigma-Aldrich, Merck KGaA, Darmstadt, Germany*
Mouse anti-beta-actin antibody (ab8227)	*Abcam, Cambridge, UK*
Rabbit anti-3-NT antibody (06-284)	*Millipore, Merck KGaA, Darmstadt, Germany*
Rabbit anti-iNos antibody (ab3523)	*Abcam, Cambridge, UK*
Rabbit anti-iNOS antibody (NB300-605)	*Novus, Bio-Techne, Minneapolis, MN, USA*
Rat anti-CD16/CD32 antibody (553142)	*BD Biosciences, San Jose, CA, USA*
Rat anti-CD31 antibody (550274)	*BD Biosciences, San Jose, CA, USA*

Rat anti-CD45 antibody (550539)	*BD Biosciences, San Jose, CA, USA*
Goat anti-Pecam1 antibody (AF3628)	*R&D system, Bio-Techne, Minneapolis, MN, USA*
Mouse anti-Acta2 antibody (MAB1420)	*R&D system, Bio-Techne, Minneapolis, MN, USA*

2.2 Animal experiments

To investigate the effect of iNOS-deletion in PASMCs on emphysema development, transgenic mice (see section 2.2.3) were employed to target *iNos* gene-deletion in *Acta2*$^{+}$ cells. Before exposing mice to room air (RA) or cigarette smoke (CS) for 3 months **(Figure 11a)** and 8 months **(Figure 11b)**, transgenic mice were subjected to either tamoxifen (+Tmx) or its vehicle control (+Vehicle) administration. Non-invasive transthoracic echocardiography was performed one day before hemodynamic and lung function measurements. After the sacrifice of the mice, the hearts and lungs were collected for further analyses, including right ventricular hypertrophy assessment, alveolar morphometry and designed-based stereology.

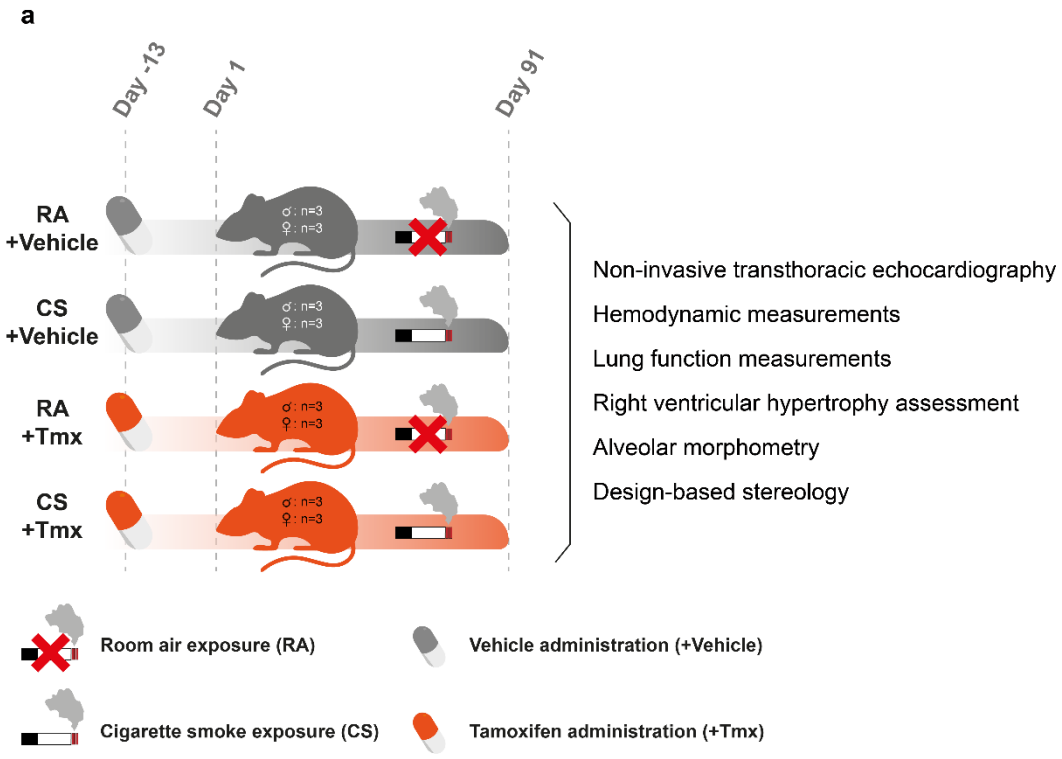

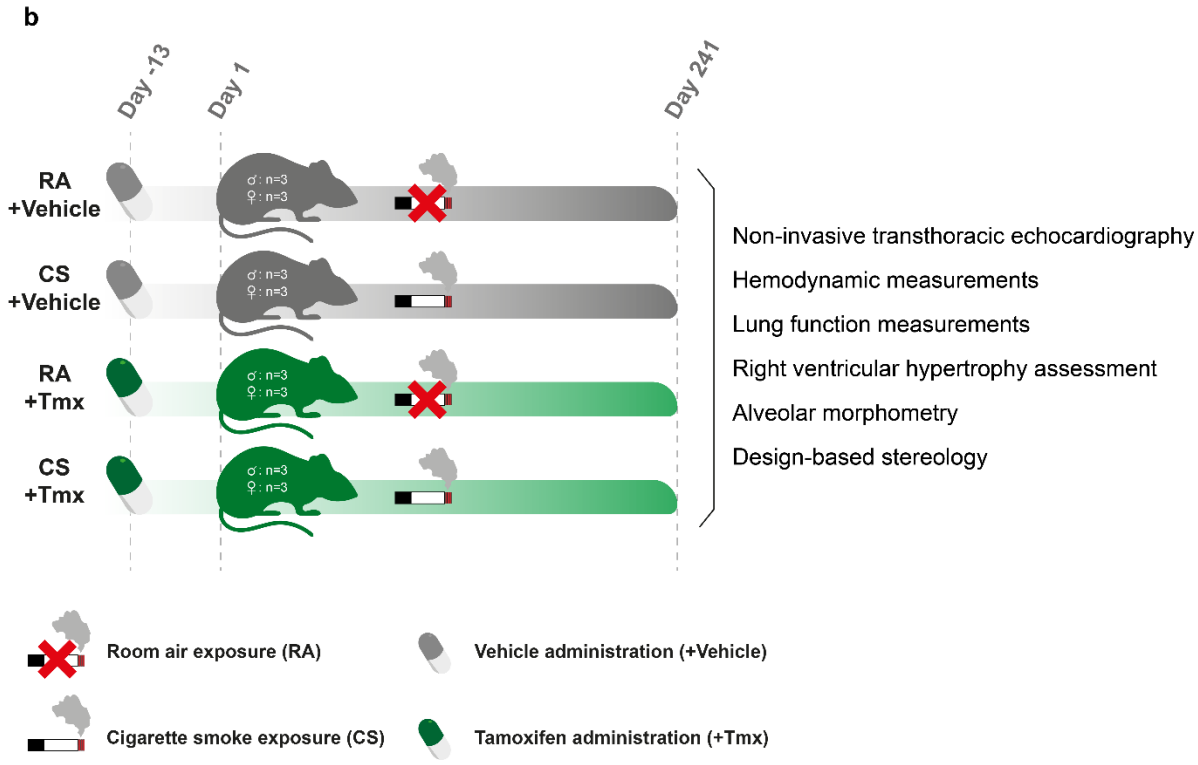

Figure 11. Schematic illustration of *in vivo* experiments. a, The mice were subjected to vehicle (+Vehicle) or tamoxifen (+Tmx) administration for 14 days prior to 90 days (3 months) of room air (RA) or cigarette smoke (CS) exposure. **b,** The mice were subjected to vehicle (+Vehicle) or tamoxifen (+Tmx) administration for 14 days prior to 240 days (8 months) of room air (RA) or cigarette smoke (CS) exposure.

2.2.1 Governmental approval for animal experiments

All animal experiments were approved by the local governmental authorities (Regierungspräsidium Gießen) and performed in accordance with the German animal welfare law and the European legislation for the protection of animals used for scientific purposes (2010/63/EU). Approval information are listed in the **Table 3**.

Table 3. Ethical approval number of animal experiments.

Animal approval number	Experimental setup
115/2014	Cell isolation
G46/2016	Cigarette smoke exposure
G95/2019	Cigarette smoke exposure

2.2.2 Animal housing

No more than five mice were housed in a single cage with bedding (wooden pieces), nesting material, water and food supply *ad libitum*. The cages were placed in an individually ventilated cage (IVC) system. The mice were under controlled conditions, in which the ambient air temperature and humidity were kept at 22±2°C and 55±10%, respectively, with 13 hours light cycle.

2.2.3 Design of animal experiments

All animals used in the current study were bred in the central animal facility of Justus Liebig University Giessen. The transgenic mice were from three different genetic backgrounds: 1) mice carrying a tamoxifen-inducible Cre recombinase gene under the control of an *Acta2* gene promoter (*Acta2*-Cre/ER^{T2}) were crossbred with 2) mice carrying a *loxP*-flanked Stop cassette followed by a CAG promoter-driven gene encoding red fluorescent protein, tandem dimer Tomato (TdTomato), inserted into the *Rosa26* gene locus. Then, the crossbred mouse strain was further crossbred with 3) mice carrying a *loxP*-flanked *iNos* gene. The offsprings were inbred to achieve homozygosity of the loci (**Figure 12**). All mice were genotyped before experiments started. Adult transgenic mice (12-16 weeks old) were randomly allocated to the experimental groups. Each group had an equal portion of male and female mice, which were administrated with tamoxifen (group name: +Tmx) or the vehicle control (group name: +Vehicle) Once tamoxifen was administrated in this mouse strain, *iNos* was deleted concomitant with the expression of the red fluorescent protein in the *Acta2*-positive (*Acta2*$^{+}$) cells. Then the mice were exposed to RA or CS for the following 3 or 8 months (**Figure 11a and 11b**).

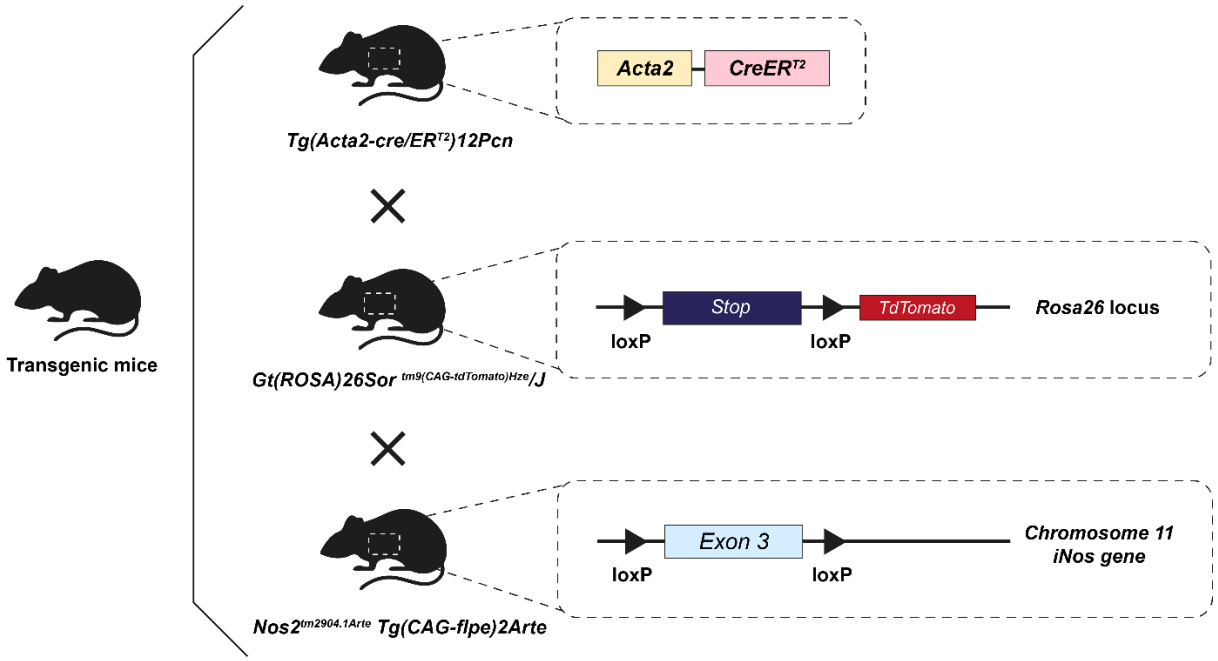

Figure 12. Schematic representation how the transgenic mice were generated. The transgenic mice used for this study were cross bred from 3 different mouse strains: 1) *Tg(Acta2-Cre/ER^{T2})12Pcn*, 2) *Gt(ROSA)26Sor$^{tm9(CAG-tdTomato)Hze}$/J*, and 3) *Nos2$^{tm2904.1Arte}$ Tg(CAG-flpe)2Arte*.
Abbreviations: Cre, Causes recombination. LoxP, Locus of crossover in P1 bacteriophage.

2.2.4 Genotyping

All mice were genotyped before the experiments started. For genotyping, 1 M NaOH solution was added into a tube with a single mouse pinna ear biopsy, followed by a 95°C incubation for 15 minutes. After adding 50 µM TRIS-HCl, the tube was vortexed and centrifuged to extract the genomic DNA for the following polymerase chain reaction (PCR). The components of each PCR are listed in **Table 4**. After PCR, the amplicons were loaded on a SYBR-safe-contained agarose gel (see section 2.5.2.2). An example of the genotyping results is shown in **Figure 13**.

Table 4. The components of each PCR for genotyping a single mouse.

Target gene	***Acta2*-Cre/ER^{T2}**	***Tdtomato*$^{flox/flox}$**	***iNos*$^{flox/flox}$**
Components	Volume (µl)	Volume (µl)	Volume (µl)
ddH_2O	7.7	14.3	9.3
FlexiBuffer	3.0	5.0	3.0
$MgCl_2$	1.2	2.0	0.9

dNTPs	0.3	0.5	0.3
Primers	0.3	0.3	0.2
GoTaq-Polymerase	0.2	0.2	0.2
Genomic DNA	2.0	2.0	1.0

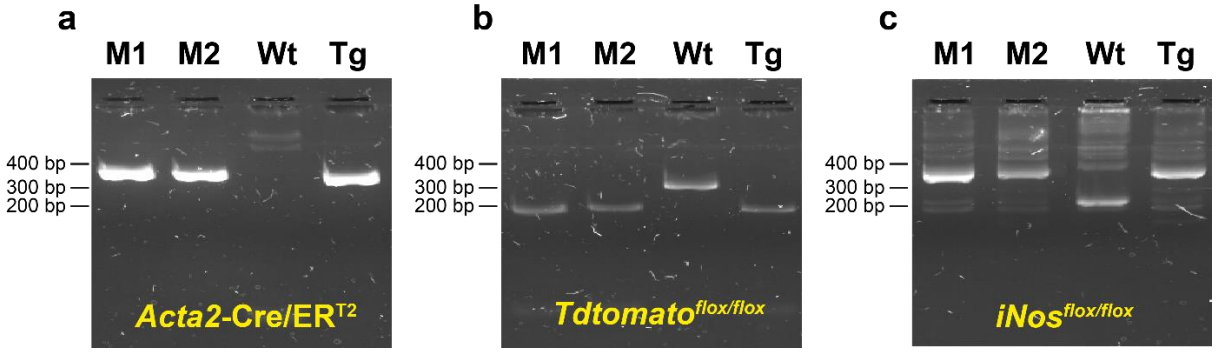

Figure 13. Representative images of the genotyping results. Before the animals were assigned to the experimental groups, the genomic DNA of each animal was tested by PCR for the amplification of the transgenes (see **Table 4**). **a,** The PCR product from the biopsy of a transgenic mouse, which carried an *Acta2*-Cre/ER^{T2} transgene, shows a band at 349 bp, but no band appears from the amplicons of the wildtype mouse. **b,** The PCR product from the biopsy of transgenic mouse, which carried a *Tdtomato*$^{flox/flox}$ transgene, shows a band at 196 bp. The amplicons from wildtype mouse show a band at 297 bp. **c,** The PCR product from the biopsy of a transgenic mouse, which carried an *iNos*$^{flox/flox}$ transgene, shows a band at 368 bp. The amplicons from a wildtype mouse shows a band at 211 bp.
Abbreviations: M1, M2 represents transgenic mouse sample. Wt, Wildtype mouse. Tg, Transgenic mouse.

2.2.5 Tamoxifen and vehicle solution preparation

Tamoxifen was dissolved into the corn oil (vehicle) for preparing a 10 mg/ml tamoxifen solution. Prior to administration, both vehicle and tamoxifen solution were warmed up in a water bath at 37°C. Each mouse was administrated with either vehicle or tamoxifen solution via intraperitoneal (i.p.) injection (0.1 ml solution/10g weight of mouse) and once a day (q.d.) for 5 days.

2.2.6 Chronic cigarette smoke exposure

Mainstream cigarette smoke (CS) was produced by the combustion of 3R4F cigarettes in a semi-automatic CS-generator and conveyed to the exposure chambers as previously described [44, 93, 97]. Animals were kept in those chambers for 6 hours/day, 5 days/weeks for 3 or 8 months. The concentration in the exposure chamber was gravimetrically measured and adjusted to a concentration of 200 mg particulate matter per m^3. The age-matched control mice were kept in the same conditions but without CS exposure. The smoke exposure setup and the mice lungs that were exposed to either RA or CS for 8 months are shown in **Figure 14**.

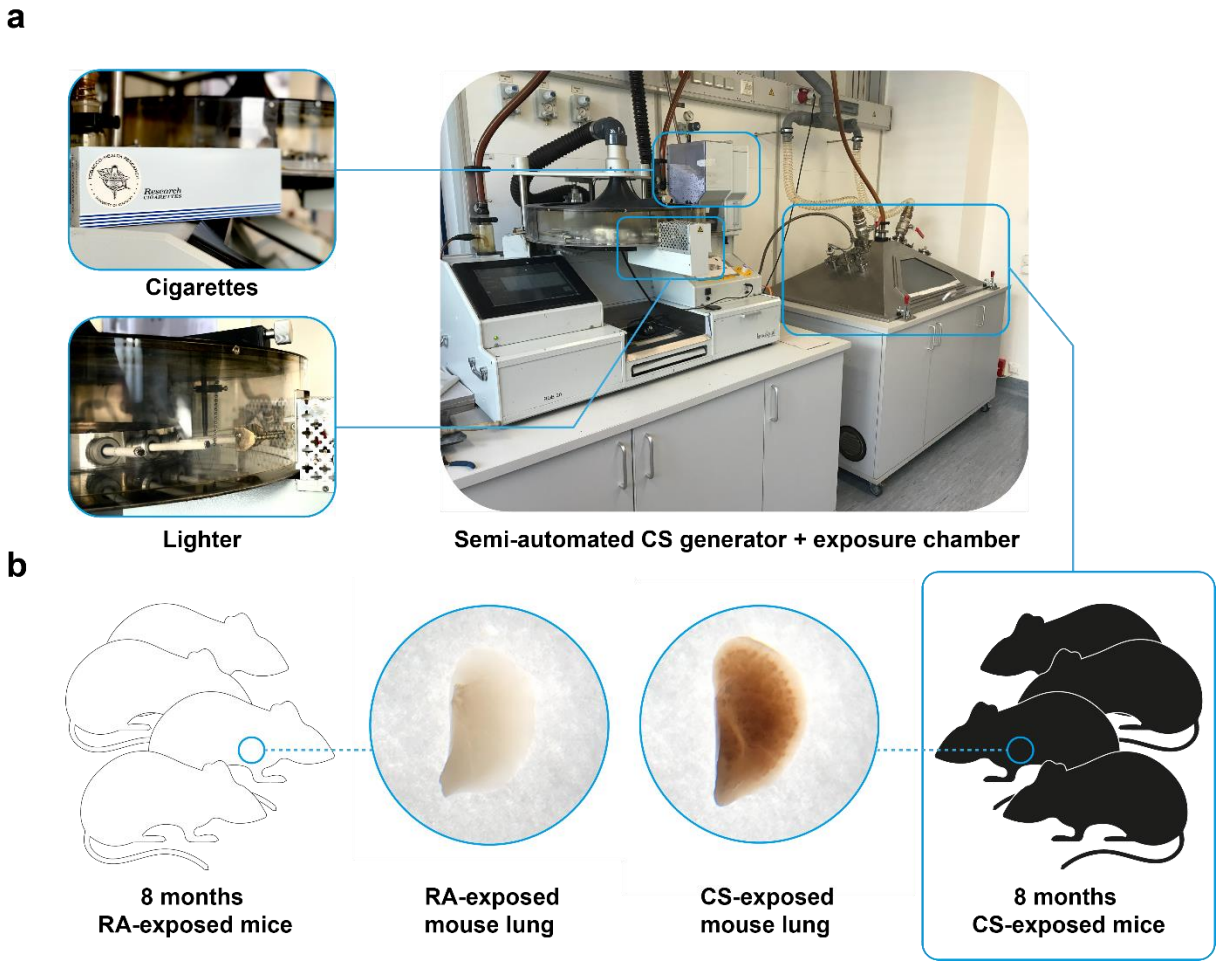

Figure 14. Chronic cigarette smoke exposure setup. a, Images of cigarettes, the lighter of the semi-automated cigarette smoke generator and the exposure chamber. **b,** Representative images of a formalin-fixed mouse lung lobe after 8 months of room air or cigarette smoke exposure. Abbreviations: RA, Room air. CS, Cigarette smoke.

2.2.7 Non-invasive transthoracic echocardiography

Non-invasive *in vivo* transthoracic echocardiography was performed, using a Vevo® 2100 high-resolution Imaging System equipped with a high-frequency M550D transducer (22-55 MHz). The mice were anesthetized using 3% isoflurane and maintained with 1.5% isoflurane supplemented in 100% oxygen. The body temperature and heart rate were monitored and the chest hairs were removed before the imaging **(Figure 15a)**. All parameters were measured and calculated as previously reported [44, 97, 115, 116].

Briefly, the right ventricular outflow tract (RVOT) was displayed under the parasternal short-axis view. The PA flow velocity time integral (VTI) were acquired from a pulsed-wave Doppler flow velocity profile of the RVOT in a superior angulation. By multiplying the PA area and the RVOT-VTI, the echocardiography-derived stroke volume was determined. Cardiac index (CI) was calculated by the following formula:

$$CI = \frac{Stroke\ volume\ \times Heart\ rate}{Body\ weight} \qquad -Formula\ 1$$

To determine the afterload of the right ventricle (RV), the ratio of pulmonary artery acceleration time (PAT, defined as the time from the initial onset of pulmonary artery (PA) flow velocity to the maximum) and pulmonary artery ejection time (PET, defined as the total duration of the flow through the pulmonic valve) was calculated **(Figure 15b)**.

For determination of RV dilatation, the right ventricular internal diameter (RVID) was assessed under the RV-focused apical 4-chamber view. In the same view, the tricuspid annular plane systolic excursion (TAPSE) were measured as an indicator of RV function. RVID was measured as the distance between the RV free wall and the septum in B-mode, whereas TAPSE was analyzed in anatomical M-mode (AM mode. Furthermore, to assume a possible RV hypertrophy in mice, the RV free wall thickness (RVWT) was evaluated under a modified parasternal short-axis view **(Figure 15c)**.

For the left heart structure and function, the parasternal long-axis view was introduced to acquire left ventricular interventricular septal thickness (IVS), internal diameter (LVID), and posterior wall thickness (LVPW) at both end-systole and end-diastole (IVS;s, LVID;s, LVPW;s and IVS;d,

LVID;d, LVPW;d, respectively) from M-model images at the level of the papillary muscles **(Figure 15d)**. LV ejection fraction (EF) was calculated under the following formula:

$$EF(\%) = 100 \times \left\{\frac{[(LVID;d)^3 - (LVID;s)^3]}{(LVID;d)^3}\right\} \qquad -Formula\ 2$$

Echocardiographic analyses, measurements and calculations were performed in a blinded manner.

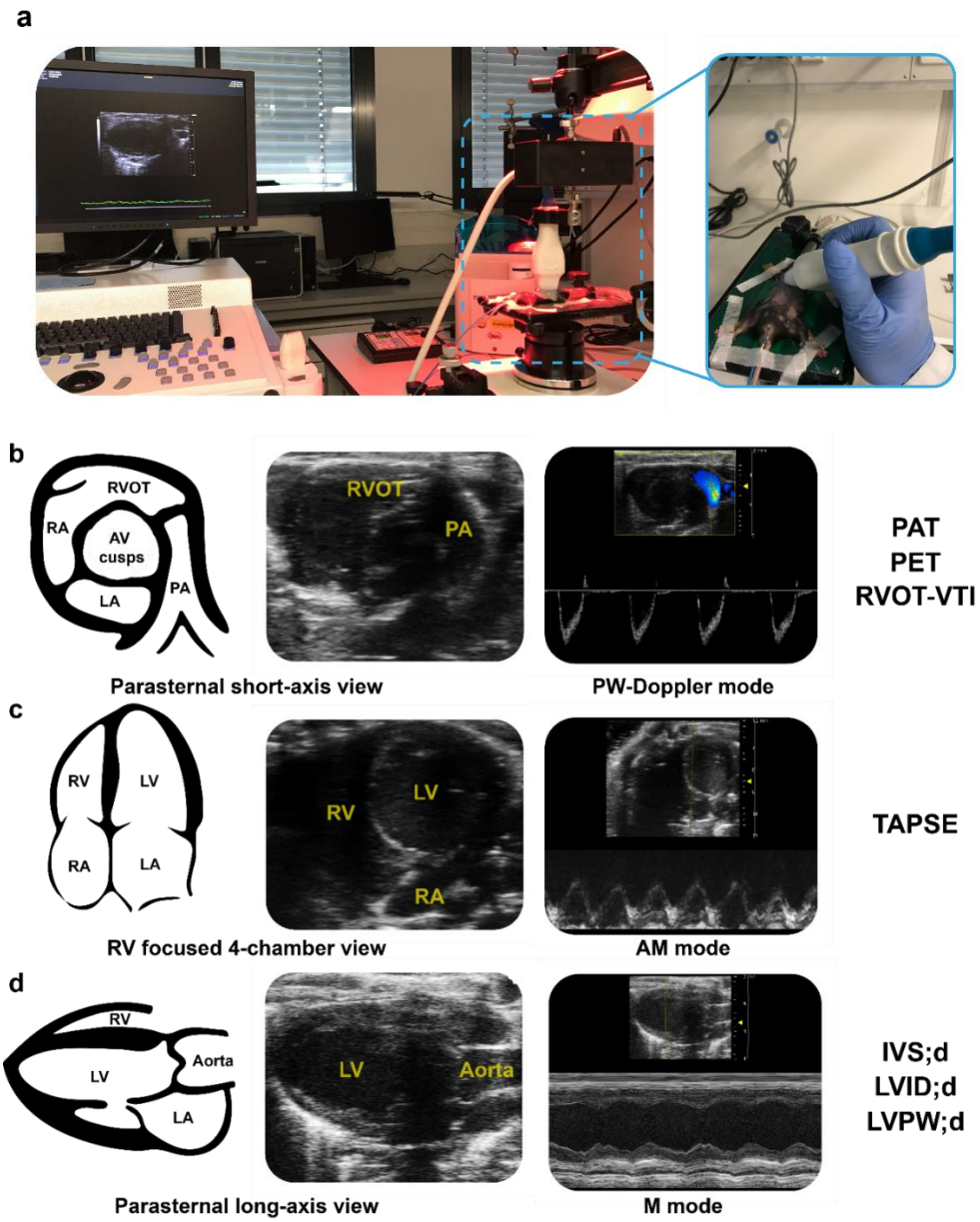

Figure 15. Non-invasive transthoracic echocardiography. a, A photo of the Vevo® 2100 high-resolution Imaging System taken during a measurement. **b,** Representative images acquired from parasternal short-axis view and PW-Doppler mode. **c,** Representative images acquired from RV focused 4-chamber view and AM mode. **d,** Representative images acquired from parasternal long-axis view and M mode.
Abbreviations: RV, Right ventricle. LV, Left ventricle. RVOT, Right ventricular outflow tract. AV, Aortic valve. LA, Left atrium. RA, Right atrium. PA, Pulmonary artery. PAT, Pulmonary artery acceleration time. PET, Pulmonary artery ejection time. PW, Pulsed-wave. VTI, Velocity time integral. AM mode, Anatomical motion mode. M mode, Motion mode. IVS;d, Interventricular septal thickness; diastolic. LVID;d, Left ventricular internal diameter; diastolic. LVPW;d, Left ventricular posterior wall thickness; diastolic.

2.2.8 Lung function measurement

In vivo lung function was measured by Marija Gredic, PhD (Excellence cluster cardiopulmonary institute [CPI], Justus Liebig University, Giessen, Germany), following previously described protocols with slight modifications [47, 93, 97]. For anesthesia, mice were placed in a chamber, infused with 3% isoflurane supplemented with 100% O_2 at a flowrate of 1 liter/minute. After reaching surgical tolerance, the mouse was restrained on a thermoregulation plate with constant anesthesia supply via a mask covering the nose and the mouth. The body temperature and the electrical activity of the heart were monitored by a rectal thermometer and electrocardiogram (ECG) electrodes, respectively. The mouse was subjected to a tracheotomy, followed by the intubation using a 18G metal tubus. The tubus was fixed in the trachea with a thread and the mouse was ventilated by a FlexiVent system, equipped with a FX2 module, at a frequency of 150 breaths/minute and a tidal volume of 5 ml/kg. *In vivo* lung function tests (pressure-volume loops and static compliance) were performed using the FlexiVent predetermined script at a positive end-expiratory pressure (PEEP) of 3 cmH_2O, with a consistent perturbation order, following the manufacturer's recommendations and the previous published article [93]. The results are presented as an average of x measurements and a coefficient of determination above 0.95.

2.2.9 Hemodynamic measurement

Hemodynamic measurements were performed by by Marija Gredic, PhD (Excellence cluster cardiopulmonary institute [CPI], Justus Liebig University, Giessen, Germany), following previously described protocols [44, 47, 93, 97, 117]. Briefly, the mouse jugular vein was surgically exposed and a micro-tip catheter (SPR 671; REF 8406719; Millar Instruments, Houston, TX,

USA) was forwarded into the right ventricle to assess right ventricular systolic pressure (RVSP). Measurements were recorded and analyzed using the PowerLab system and LabChart 7.0 software. Once the measurements were finished, the animals were sacrificed by exsanguination.

2.2.10 Organ harvest and lung fixation

Following sacrifice, the animals' abdominal and thoracic cavities were opened. The liver and kidney were collected. The lungs were continuously ventilated and perfused with a saline solution at 22 cmH_2O pressure through the pulmonary artery until the lungs were visibly blood free. The right lung lobes were then collected and snap-frozen in liquid nitrogen for further analyses. After removal of the right lung lobes, the left lung lobe was fixed under simultaneous vascular perfusion (20 cmH_2O) and lung inflation (12 cmH_2O) with formalin for 20 minutes. Subsequently, the left lung lobe was removed from the thoracic cavity and placed in a 4% formaldehyde solution overnight at room temperature.

After removal from the thoracic cavity, the heart was separated into two parts: (1) right ventricle (RV), (2) left ventricle and septum (LV+S). To assess RV hypertrophy, Fulton index was calculated by the following equation:

$$Fulton\ index = \frac{RV\ weight}{(LV + S)\ weight} \qquad -\ Formula\ 3$$

The entire procedure of organ harvesting is illustrated in **Figure 16**.

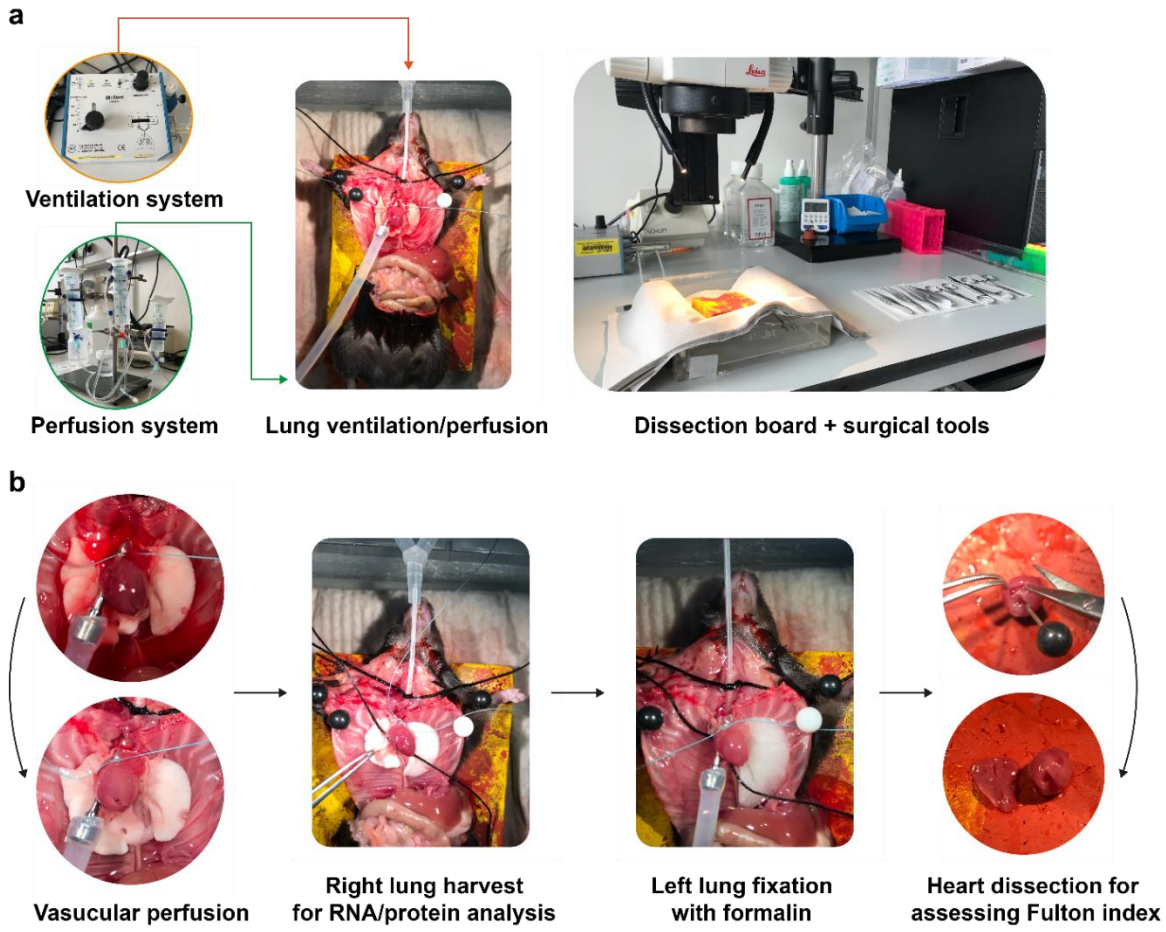

Figure 16. The procedure of mouse lung and heart organ harvesting. a, Illustration of the lung ventilation/perfusion system, dissection board and surgical tools. **b,** The catheter was inserted into the pulmonary artery with a constant flow of saline solution. Once the lungs were blood free, the right lung was removed and snap-frozen. The catheter was again inserted into the pulmonary artery with a constant flow of formalin solution. Simultaneously, the lung was inflated with formalin solution through the trachea. After removal of the left lung lobe, the heart was dissected into two parts: right ventricle and the left ventricle + septum for Fulton index measurement.

2.3 Human lung tissue samples

Human lung tissues, obtained from the biobank of the German Center for Lung Research (Deutsches Zentrum für Lungenforschung Biobank), were directly processed for cell isolation/cryo-embedding, snap-frozen for mRNA/protein extraction, or fixed in 4.5% (v/v) paraformaldehyde for histology after explantation. Acquired tissues were from healthy donors, donors that were determined by pathologists as smokers, smokers with no/mild COPD (GOLD

stage 0/1) who had undergone pulmonary lobectomy, and smokers with end-stage COPD (GOLD stage 3/4) who had undergone lung transplantation. The studies were approved by the Ethics Committee of the Justus-Liebig-University School of Medicine (AZ 58/15).

2.4 *In vitro* experiments

2.4.1 Murine cell isolation and culture

Mice were anesthetized with a mixture of ketamine (100 mg/kg body weight), xylazine (20 mg/kg body weight), and heparin (50,000 IU/kg body weight), followed by exsanguination. Then, the lungs from the euthanized mouse were perfused through the pulmonary artery with saline solution.

2.4.1.1 Murine pulmonary artery smooth muscle cells

The murine pulmonary artery smooth muscle cell (mPASMCs) isolation was performed following a previously described protocol [47]. Briefly, the *Wt* and *iNos*$^{-/-}$ mice lungs were perfused via the pulmonary artery with 3 ml Dulbecco's phosphate-buffered saline. Each mouse lung was installed with 5 mg/mL agarose/iron solution via the pulmonary artery and filled with 10 mg/mL agarose solution through the trachea until the lung was inflated. The iron-filled lung was then removed from the thoracic cavity and placed into ice-cold DPBS for 10 minutes.

Afterwards, the iron-filled lung was mechanically minced by 3-scissors and enzymatically digested at 37°C with warm collagenase solution for 1 hour, followed by shearing with both a 15 Gauge and 18 Gauge syringe needle. To stop the collagenase activity, M199 medium with 10% fetal bovine serum (v/v) and 1% penicillin/streptomycin (v/v) was added. A magnetic concentrator was employed to separate the isolated vessel pieces (attached to iron) from other tissue fragments. The isolated vessel pieces were immersed by Smooth Muscle Cell Growth Medium 2, supplemented with 10% FBS (v/v), 1% P/S (v/v), and 100 µg/ml Normocin^{TM} on a culture dish. After 18 days, PASMCs sprouted from vessel pieces were washed with PBS, detached by 1x trypsin and centrifuged at 1200 rpm for 5 minutes. For all the experiments, PASMCs were seeded at a density of 10,000 cells/cm^2 on culture dishes/plates. Cells were used for experiments until passage 2.

2.4.1.2 Murine alveolar type 2 epithelial cells

The isolation of murine alveolar type 2 epithelial cells (mAEC2s) was performed following a previously described protocol [47]. Briefly, *Wt* and *iNos*$^{-/-}$ mice lungs were perfused via the pulmonary artery with 3 ml Dulbecco's phosphate-buffered saline and inflated through the trachea with 1 mL dispase. The lungs were subsequently placed into falcon tubes and incubated with dispase at 37°C for 45 minutes. Then, the lung lobes were minced by scalpels. The fine suspension was washed with Dulbecco's Modified Eagle Medium and filtered sequentially through 70 µm and 40 µm strainers. After centrifugation at 4°C, 800 rpm for 10 minutes, cell pellets were re-suspended in DMEM medium. Then the cell suspension was plated on a 100 mm non-culture petri dish, which was pre-coated with rat anti-mouse CD45, rat anti-mouse CD31, and rat anti-mouse CD16/CD32 (all of them in 1:1000 dilution) antibodies. The dish was placed into an incubator for 30 minutes at 37°C. The non-adherent cells were transferred from an antibody-coated dish to a new culture dish. After incubation for 60 minutes at 37°C, the non-adherent cells were collected and centrifuged (the adherent cells were kept for pulmonary fibroblasts culture – see section 2.4.1.2). The number of mAEC2 was determined by Nile red staining in a Neubauer chamber.

The cells were seeded directly after isolation on 96-well plates coated with fibronectin. Each well contained 40,000 mAEC2 in DMEM supplemented 10% FBS (v/v) and 1% P/S (v/v).

2.4.1.3 Murine pulmonary fibroblasts

The isolation of murine pulmonary fibroblasts (mFBs) was described in mAEC2s isolation – see section 2.4.1.2. Once the non-adherent cells were removed from the culture dish, the DMEM supplemented with 10% FBS (v/v), 1% P/S (v/v), and 100 µg/ml Normocin^{TM} (DMEM growth medium) was added. The cells were trypsinized and passaged when they reached 80% confluence. After four passages, the cells were used for experiments. For all experiments, mFBs were seeded at a density of 10,000 cells/cm^2 on culture dishes/plates (no more than 8 passages).

2.4.2 Human pulmonary artery smooth muscle cell culture

Primary human PASMCs (hPASMCs) were purchased from Lonza and maintained in Smooth Muscle Cell Growth Medium 2, containing Smooth Muscle Cell Growth Medium 2 SupplementMix, 10% FBS (v/v), 1% P/S (v/v), and 100 µg/ml Normocin^{TM}. Cells were incubated

at 37°C in a humidified atmosphere of 5% CO_2. Experiments were performed between passage 3 to 8 at a seeding density of 10,000 cells/cm^2.

2.4.3 Cigarette smoke extract (CSE) preparation

Mainstream smoke from a burning 3R4F cigarette was drawn into a falcon tube containing 10 ml of the vehicle medium (DMEM supplemented with 1% P/S (v/v)) by a vacuum pump. The burning of a whole cigarette was restrained to 1 minute by a pressure regulator. The apparatus was assembled in a fume hood as shown in **Figure 17**. CSE strength was measured using a spectrophotometer and calculated by dividing the absorbance at a wavelength of 290 nm by the absorbance at a wavelength of 280 nm (A_{290nm}/A_{280nm}). Then, CSE was sterile-filtered through a 0.22-µm pore filter and adjusted to a pH of 7.4. The CSE solution was considered 100% and diluted with growth medium to the indicated concentration. The solution was delivered to the cells within 30 minutes upon preparation.

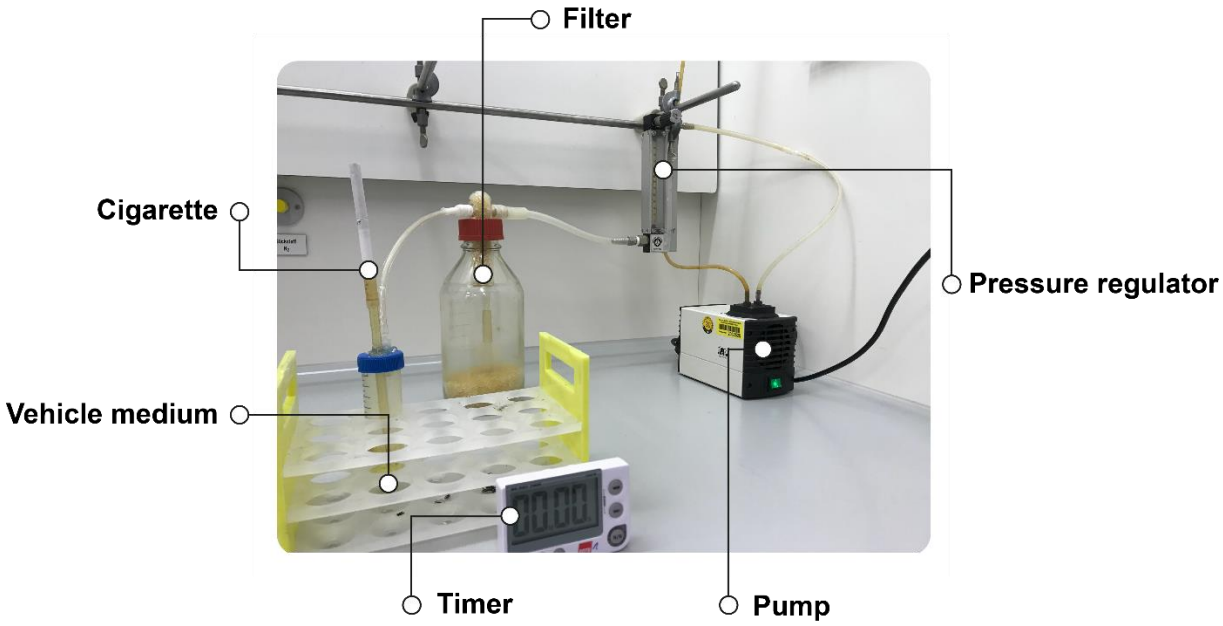

Figure 17. *In vitro* CSE exposure preparation setup. CSE was prepared under a fume hood. After the cigarette was lit, the pump was switched on and then the main stream smoke was bubbled through the vehicle medium. Abbreviation: CSE, Cigarette smoke extract.

2.4.4 Cell survival assay

A sulforhodamine B (SRB) colorimetric assay was employed to determine cell survival. All procedures were conducted based on a previous publication [118]. Briefly, the cells were seeded on a 96-well plate one day before CSE exposure. After 6 hours of CSE exposure, 100 µl cold 10% trifluoroacetic acid aqueous solution (TCA; v/v) was added in each well to fix the cells. The plate then was incubated for 1 hour at 4°C. Subsequently, the plate was rinsed with sterile water to remove the fixative. Followed by drying the plate, 0.05% SRB in 10% acetic acid (v/v) was added to stain the cell protein component. 1% acetic acid (v/v) was used to rinse the excessive SRB solution before 10 µM Tris-base (pH = 10.5) was added to dissolve SRB. The Fluorescence intensity (FI) was measured by a microplate reader (excitation/emission wavelength: 488/585 nm). The cell survival, shown in percentage, was calculated by following equation:

$$Cell\ survival\ (\%) = \frac{FI\ (indicated\ CSE\ concentration) - FI\ (blank)}{FI\ (indicated\ cell\ in\ 0\%\ CSE) - FI\ (blank)} \times 100\% \qquad - Formula\ 4$$

2.4.5 N^6-(1-Iminoethyl)-lysine (L-NIL) treatment preparation

N^6-(1-Iminoethyl)-lysine (L-NIL) is an analogue of nitric oxide synthase substrate, *L*-arginine **(Figure 18)**, which can selectively inhibit iNOS activity over other isoforms, endothelial nitric oxide synthase (eNOS) and neuronal nitric oxide synthase (nNOS) [119]. To ensure the compounds potency during the treatment, L-NIL working solution was always freshly prepared by dissolving it into PBS. On the next day after the cell were seeded on a 96-well plate, the cells was treated with freshly prepared L-NIL in the indicated concentration. After 1-hour pre-treatment, the cells were exposed to the indicated concentration of CSE. The control group was treated with PBS and denoted as “Vehicle”.

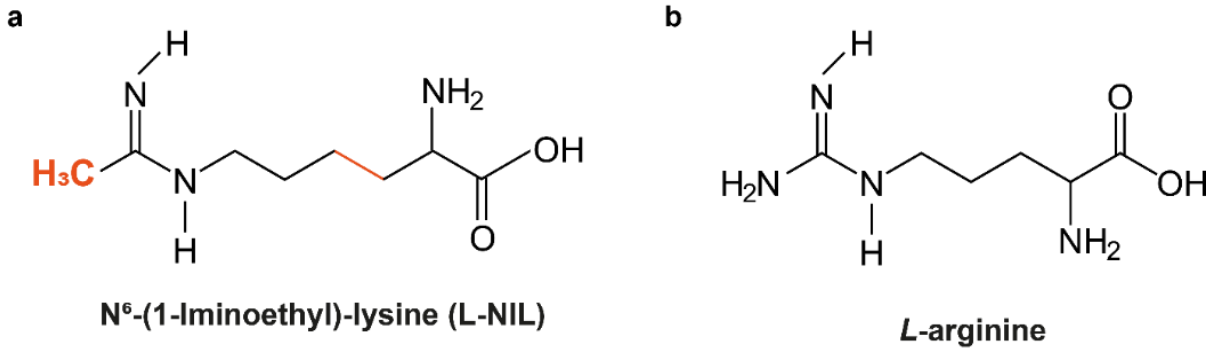

Figure 18. Chemical structure of the iNOS selective inhibitor – L-NIL and *L*-arginine a, L-NIL. **b,** *L*-arginine.

2.4.6 Intracellular nitric oxide detection

To detect intracellular nitric oxide, 4-amino-5-methylamino-2', 7'-difluorofluorescein diacetate (DAF-FM DA) was applied. DAF-FM DA is a cell-permeable compound **(Figure 19)**. Upon reaction with esterase, it is converted into a non-cell-permeable chemical, DAF-FM. Once nitric oxide is present, it oxidizes DAF-FM, forming a fluorescence product, DAF-FM triazolo-fluorescein (DAF-FM T) [120]. The cells were seeded on a 96-well plate one day before CSE exposure. After 6 hours of CSE exposure, the medium in the well was substituted by growth medium containing 10 μM of DAF-FM DA. The cells were incubated with the DAF-FM DA-contained medium for 30 minutes at 37°C. After the incubation, the medium containing DAF-FM DA was replaced by fresh growth medium and the plate was incubated at 37°C for 15 minutes. The fluorescence intensity was assessed by Incucyte ZOOM after the final incubation (excitation/emission wavelength: 460/524 nm). The results were calculated by the software provided by the manufacturer.

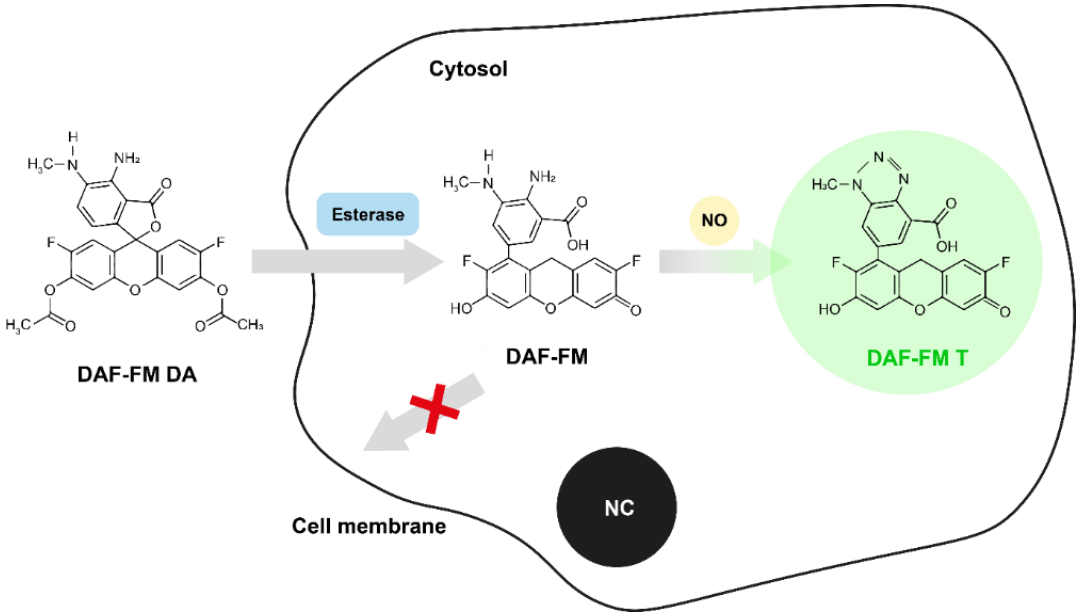

Figure 19. The mechanism of intracellular NO detection by DAF-FM DA. DAF-FM DA is a cell permeable molecule. It is hydrolyzed by esterases in the cytosol, which forms a cell impermeable compound, DAF-FM. DAF-FM reacts with NO, forming a strong fluorescent compound, DAF-FM T.
Abbreviations: DAF-FM DA, 4-amino-5-methylamino-2', 7'-difluorofluorescein diacetate. DAF-FM T, DAF-FM triazolo-fluorescein. NO, Nitric oxide. NC, Nucleus.

2.5 Molecular biology

2.5.1 Sample preparation

2.5.1.1 Preparation for RNA expression analyses

For RNA isolation, cells were lysed with RLT buffer supplemented with 1% 2-mercaptoethanol (v/v). Total RNA was isolated by using the RNeasy Mini kit. Following, the concentration of the RNA was quantified by a Nanodrop. The purified RNA was reverse-transcribed by using the iScript cDNA Synthesis Kit following the manufacturer's instructions and a thermocycler following the protocol listed in the **Table 5**.

Table 5. Synthesis of cDNA.

Step	Temp. (°C)	Time (sec.)
1	25	300
2	46	1200
3	95	60
4	4	∞

2.5.2.2 Preparation for antibody-based protein analyses

Cells or lung tissues were lysed by using the Cell lysis buffer supplemented with 1 mM phenylmethylsulfonyl fluoride (PMSF). The lung tissues were further homogenized with a Precellys® 24 bead beating tissue homogenizer. Following, the lysates were quantified by a DC™ protein assay. The protein expression was examined by either western blotting or capillary-based protein immunoassay.

2.5.2 RNA expression analysis

2.5.2.1 Real-time quantitative reverse transcriptase polymerase chain reaction (qRT-PCR)

0.5 µg of cDNA was plated on Hard-Shell® 96-Well PCR plates with the iQ SYBR Green Supermix and the target gene-specific primers – inducible nitric oxide synthase (*iNOS*). Beta-2-microglobulin (*B2M*) was used as a reference gene. All assays were confirmed to have an optimum amplification efficiency and that the Ct values were all within the validated dynamic range. All primers used in my thesis were purchased from Metabion International AG and are listed in the section 2.1.5. The procedure of the qRT-PCR is listed in the **Table 6**.

Table 6. Real-time quantitative reverse transcriptase polymerase chain reaction protocol.

Step	Procedure	Temp. (°C)	Time (sec.)	Cycle	Note
1	Pre-denaturation	95	600	1	
2	Denaturation	95	10	40	

3	Primers Annealing	59	10		
4	Elongation	72	10		
5	Data collection	72	10		Back to step 2
6	Melting curve construction	55-95 (+0.5/cycle)	10 + 5	80	0.5°C increment with 5 seconds for data collection

2.5.2.2 Agarose gel electrophoresis

1X sodium borate (SB) buffer was prepared by mixing 50 ml of 20X SB buffer and 950 ml of ddH_2O. A 2% agarose gel was prepared by dissolving 2 gram of agarose in 100 ml 1X SB buffer. Before polymerization of the agarose, 2 µl SYBR Safe DNA gel stain was added. 10 µl of amplicons were mixed with 2 µl of 6X DNA gel loading dye prior to loading on the 2% agarose gel. At least one well from each agarose gel was loaded with a 50 bp DNA Ladder. DNA bands were visualized using a ChemiDoc™ Touch Imaging System.

2.5.3 Antibody-based protein analysis

2.5.3.1 Western blotting

20 µg of protein was added into a tube, containing 1X Laemmli sample buffer, supplemented with 10% 2-mercaptoethanol (v/v). After 5 minutes incubation at 95°C, the samples were loaded on TGX FastCast stain-free 12% polyacrylamide gels (v/v) and separated by electrophoresis (100 Volts, 400 mA, 150 W for 1.5 hrs). Then, the separated proteins were transferred to a polyvinylidene difluoride (PVDF) membranes, by a Trans-Blot® Turbo Semi-dry system. After blocking with 6% skimmed milk (w/v) for an hour, the membrane was incubated with a primary antibody overnight at 4°C. Followed by a washing step using TBS-T buffer (TBS + 1% Tween 20 (v/v)) for 5 minutes, the membrane was incubated with a secondary antibody conjugated with horseradish peroxidase for 1 hour at room temperature. Subsequently, the membrane was washed with TBS-T buffer (TBS + 1% Tween 20 (v/v)) for 5 minutes 3 times. Protein bands were visualized with the Amersham ECL Plus western blotting detection system, using a ChemiDoc™ Touch imaging system. Densitometry was performed with the Image Lab™ Software and each

band was standardized to the intensity of β-actin that was used as a loading control. Rabbit anti-iNOS (1:500), mouse anti-β-actin (1:50,000) primary antibodies, anti-rabbit (1:5,000) and anti-mouse (1:5,000) secondary HRP conjugated antibodies were used in this assay.

2.5.3.2 Capillary-based protein immunoassay

0.2 µg/µL of protein sample was prepared following the protocol provided by the manufacturer. Samples, blocking buffer, primary and secondary antibodies, wash buffer, recasting Replex buffer and Lumino-peroxide mix were all loaded into a plate, pre-filled with separation matrix, stacking matrix, split running buffer 2 and matrix removal buffer. The loaded plate was placed into a capillary-based protein immunoassay instrument – JESS for the analysis. A rabbit anti-3-NT antibody (1:20, 06-284, Millipore, Merck KGaA, Darmstadt, Germany) was used as a primary antibody. Antibody detection was done by using the ready-to-use anti-rabbit secondary antibody provided by ProteinSimple. The total protein assay was performed for protein normalization purposes. Results were calculated by the integration of areas under the peaks at the size of the target proteins. The instrument and the plate arrangement is shown in **Figure 20**.

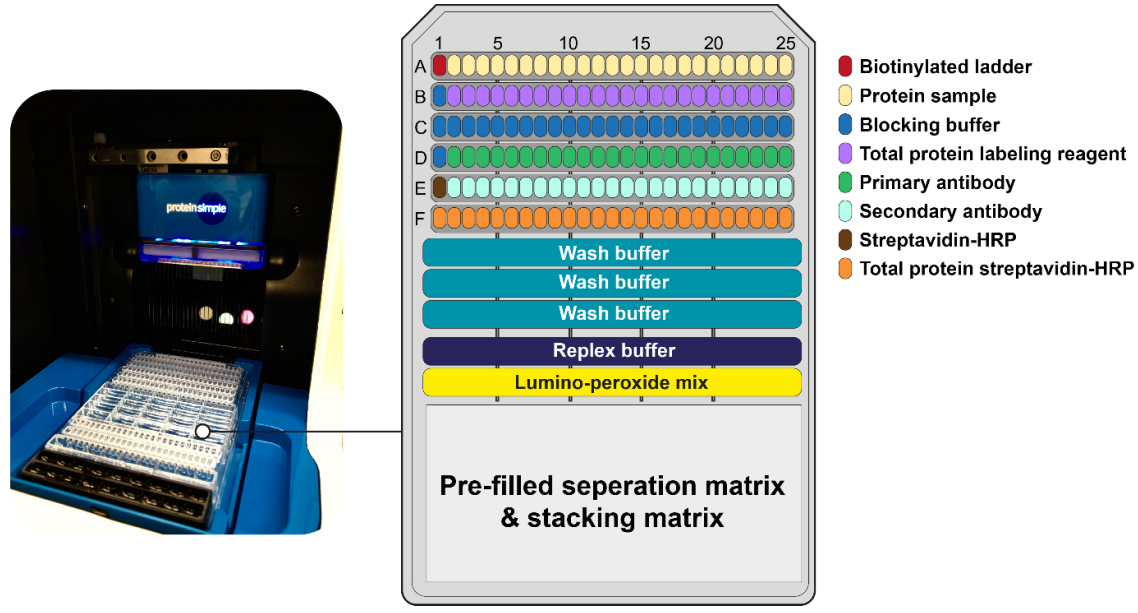

Figure 20. Capillary-based protein immunoassay. Image, taken by myself, of a plate put into the JESS device and a plate arrangement suggested by the manufacturer (right). The image of the pre-filled plate was designed based on the manual guide provided by the manufacturer.

2.6 Histology

2.6.1 Paraffin-embedded tissue section preparation

2.6.1.1 Mouse lung volume measurement

To define the reference space of the lungs for design-based stereology, the volume of the mouse left lung lobe was determined based on Archimedes principle [121]. Briefly, a beaker containing saline was placed on the weighing scale. A lab retort stand with a meter rule was put next to the weighing scale. The tare weight was set at the position when the tea clamp infuser was fully submerged into the saline **(Figure 21a)**. Once the fixed mouse left lung lobe was completely immersed into saline, the weight was measured **(Figure 21b)**. As the density of saline is approximately 1 g/cm^3, the reference space of the lung was defined as the weight of displaced fluid.

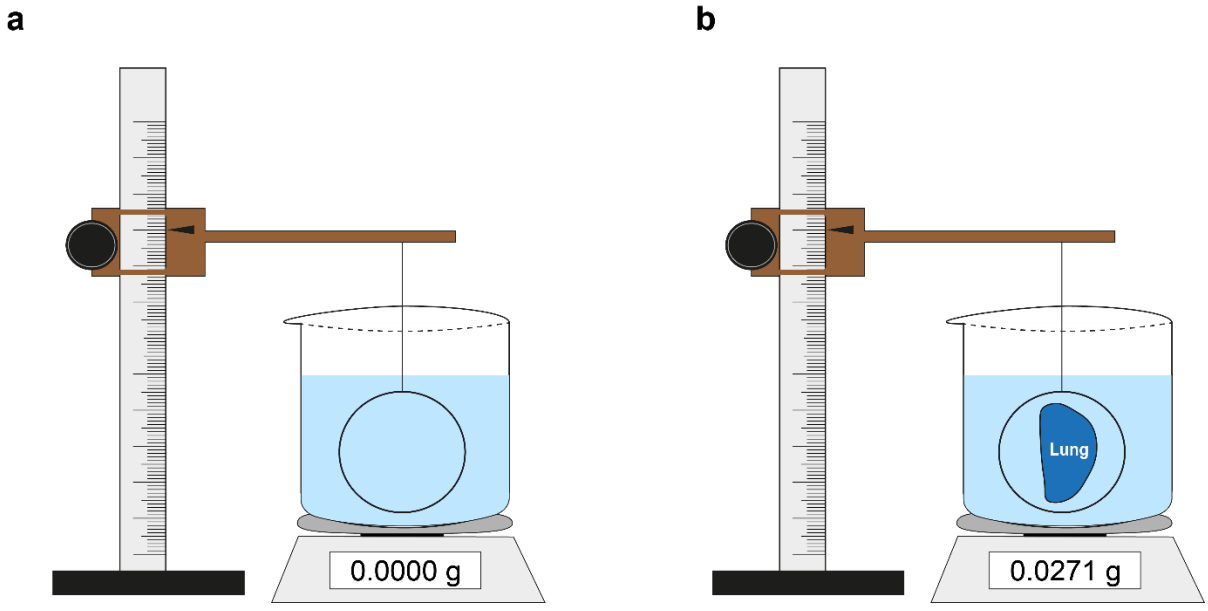

Figure 21. Measurement of the mouse lung volume. **a,** Graphical illustration of the setup for mouse lung volume determination without a formalin-fixed mouse lung. Once the tea clamp infuser was submerged in the saline, the scale was tared and the position of lab retort stand was recorded. **b,** Graphical illustration of the setup for mouse lung volume determination with a formalin-fixed mouse lung. The formalin-fixed mouse lung was placed into the tea clamp infuser and the lab retort stand was set to the recorded position. The density of saline is approximately 1 g/cm^3, so the lung volume can be defined as the weight of displaced fluid.

2.6.1.2 Mouse lung sampling

To analyze in all depths through mouse left lung lobes unbiasedly, the systemic uniform random sampling principle was followed [121]. Briefly, all formalin-fixed lung lobes were put in 3% agarose **(Figure 22a)** and each agarose block was cut in 3-mm thick sections **(Figure 22b)**. The lung sections were transferred to the embedding cassettes, following a dehydration process as previously described [93]. The dehydrated tissues were then embedded into paraffin blocks, which were cooled down prior to placing in an automated microtome. Each paraffin-embedded mouse lung was cut in 3-µm thick sections by microtome blades. The cut sections were placed on a warm water bath to remove the fine wrinkles or folds, and transferred to the histological glass slides. Following a 2-hour incubation at 40°C, the dried glass slides were stored in a microscope slide box until the staining was performed.

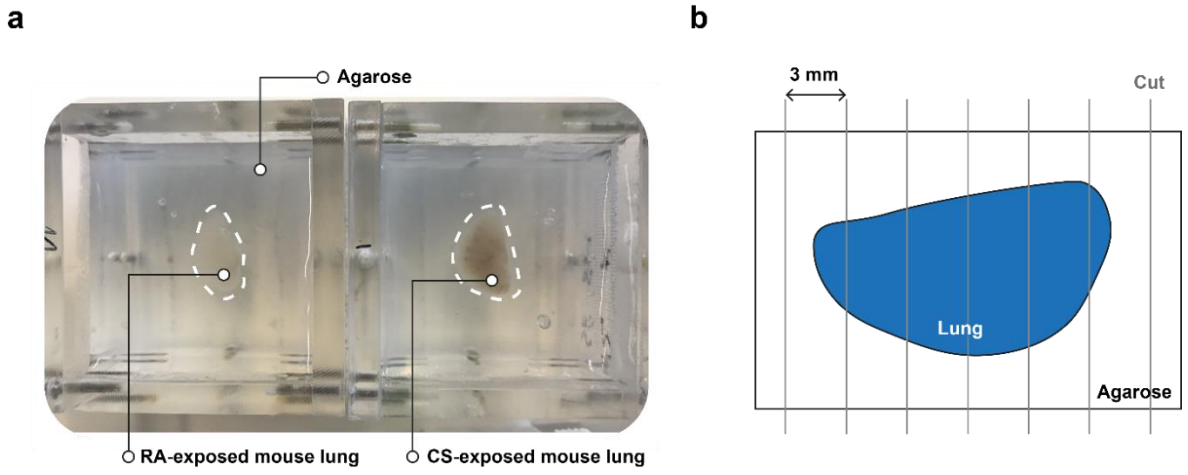

Figure 22. Sample preparation of formalin-fixed mouse lung lobes. **a,** Representative picture of a RA/CS-exposed mouse lung lobe, embedded into a 3% agarose cube. **b,** Graphical illustration of the systemic uniform random sampling. The agarose-embedded, formalin-fixed mouse lung lobe was cut into slices of equal thickness (3 mm) with a random start outside the lung.
Abbreviations: RA, Room air. CS, Cigarette smoke.

2.6.1.3 Human lung sampling

The formalin-fixed human lung biopsies were directly subjected to the dehydration process, without cutting into 3-mm thick sections. The dehydrated tissues were processed in the same way as described in section 2.6.1.2 until the staining was performed.

2.6.2 Deparaffinization and rehydration

Before any type of the staining, the paraffin slides were deparaffinized and rehydrated following the procedure shown in **Table 7**.

Table 7. Deparaffinization and rehydration protocol for paraffin-embedded slides.

Step	Procedure	Time (min.)	Reagent/condition
1	Deparaffinization	60	59°C
2		10 (3×)	Xylol
3	Rehydration	5 (2×)	Ethanol 99.6%
4		5	Ethanol 96%
5		5	Ethanol 70%
6		3 (2×)	Distilled water

2.6.3 Hematoxylin and eosin (H&E) staining

To visualize cell structures and assess alveolar morphometry, H&E staining was performed on the rehydrated slides following the protocol shown in **Table 8**. Hematoxylin stains cell nuclei a blue, whereas eosin stains cytoplasm an orange [122]. The dehydrated slides were mounted with mounting medium and covered with coverslips.

Table 8. Hematoxylin and eosin staining protocol.

Step	Procedure	Time (min.)	Reagent/condition
1	Staining	20	Acidic hematoxylin (Mayer)
2		5	Running tap water (lukewarm)
3		1	Ethanol 96%
4		4	Eosin Y
5	Dehydration	5 (2×)	Ethanol 96%
6		5	Ethanol 99.6%
7		5	Isopropanol
8		5 (3×)	Xylol

2.6.4 Weigert's elastin staining (Elastica van Weigert staining)

To visualize elastic fibres in the lungs for the quantification of alveoli density, Weigert's staining solution containing the colour complex with Resorcin-fuchsin solution was utilized [123]. The successful staining shows a dark purple color. Nuclei were stained red by a Nuclear Fast Red solution. Weigert's elastin staining was performed on the rehydrated slides following the protocol shown in **Table 9**. The dehydrated slides were mounted with mounting medium and covered with coverslips.

Table 9. Weigert's elastin staining protocol.

Step	Procedure	Time (min.)	Reagent/condition
1	Staining	At least 960	Resorcin-fuchsin solution
2		15	Running tap water
3		10	Nuclear Fast Red solution
4	Dehydration	5 (2×)	Ethanol 96%
5		5	Ethanol 99.6%
6		5	Isopropanol
7		5 (3×)	Xylol

2.6.5 Alveolar morphometry

Images of the H&E stained lung slides were acquired in a uniformly random fashion under a light microscope (CTR6000; Leica Microsystems GmbH). Airspace percentage, alveolar septal wall thickness and mean linear intercept (MLI) were assessed from the acquired images by the Qwin alveolar morphometry software as previously described [44]. Only the alveolar compartment was considered for the measurements. All visible vessels or airways were excluded from the analyzed images.

2.6.6 Design-based stereology

To estimate the number of alveoli, a three-dimensional test system was utilized. This test system is termed a physical disector [124]. Briefly, the paraffin-embedded lungs were cut alternately in 3-µm thickness, with a 3-µm distance between two sections. These two sections were placed on the same microscope slide, followed by Weigert's elastin staining procedure. Images of stained slides were scanned by a light microscope (CTR6000, Leica Microsystems GmbH), using a program equipped in the Visiopharm newCAST software. The same software was used for the analysis of the scanned slides. Each image contained a limited area as a test frame **(Figure 23)**. Two sectors were aligned and exhibited next to each other. If the alveolar wall has incomplete connection in one section, but at the same place, the corresponding section was connected, then the event was counted (so-called the "bridge") [121, 125]. The density of alveoli (alveoli/cm^3) was calculated by the following equation:

$$density\ (alveoli) = \frac{bridges}{test\ frames \times size\ of\ test\ frame\ \times thickness\ between\ 2\ sections} - Fomula\ 5$$

By multiplying the density (alveoli) with the lung volume assessed by the weight of the displaced fluid (see section 2.6.1.1), the number of alveoli in the mouse left lung lobe was estimated.

$$Number\ (Alveoli) = density\ (Alveoli) \times lung\ volume \qquad - Formula\ 6$$

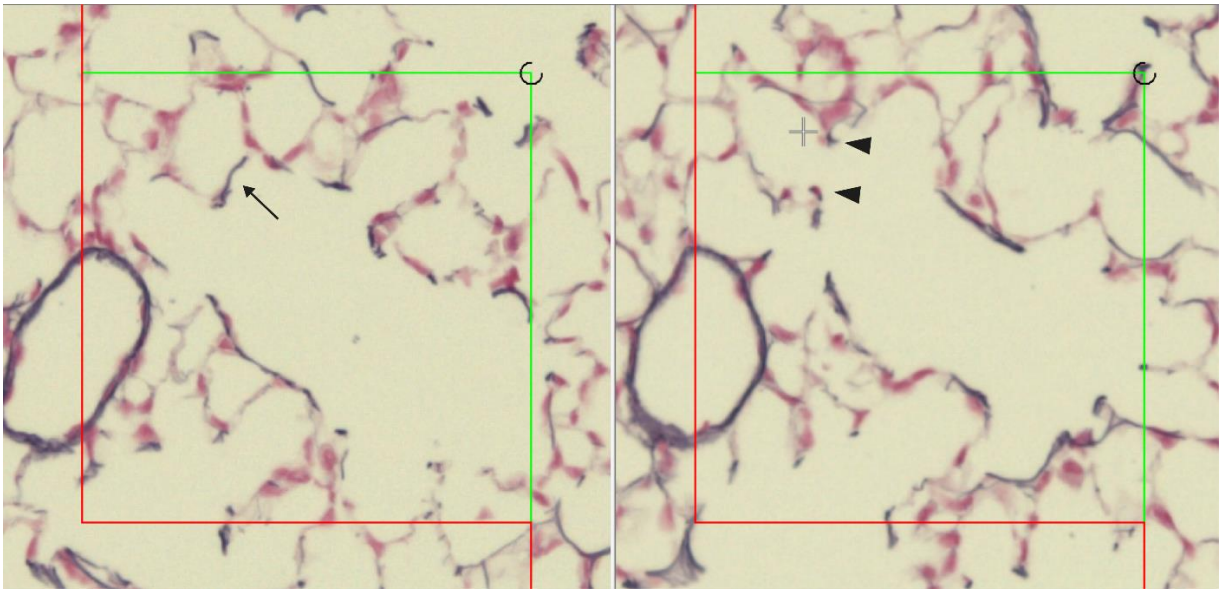

Figure 23. Representative image of assessing the alveoli density in the mouse lung, using the design-based stereology. Images from two alternate sections are superimposed. The arrow depicts the bridge in the reference section (left), whereas the arrowheads depict the absent of the bridge in the look-up section (right). If this event occurs within the counting frames (the square assembled by green and red lines), then the bridge is counted. Note that any bridges in touch with the red line are excluded, but with the green line are included in the evaluation.

2.6.7 Immunofluorescence staining and confocal microscopy

Paraffin-embedded human and mouse lungs were cut in 3-µm thick sections. Deparaffinization and rehydration was performed according to routine protocols. Antigen retrieval was performed by cooking slides in commercially available citrate buffer. Background fluorescence was quenched by using the MaxBlock™ autofluorescence reducing reagent kit following the manufacturer's protocol. Unspecific binding was blocked by 10% BSA (v/v). The slides from mouse lungs were incubated overnight at 4°C with a rabbit anti-iNOS antibody (abcam, 1:100), goat anti-Pecam1 (R&D system, 1:200), mouse anti-Acta2 (R&D system, 1:200), whereas those from human lungs were incubated with rabbit anti-3-NT (Millipore, 1:100). The next day, slides were washed in PBS and incubated with donkey anti-rabbit, donkey anti-goat or donkey anti-mouse secondary antibodies conjugated with fluorescent dyes Alexa Fluor 488, 555 or 647 (Invitrogen, 1:400) for 3 hours at room temperature. All antibodies were diluted in a 10% BSA solution (v/v). After washing and staining with 0.1 µg/ml DAPI (for human lung slides) or 10 ng/ml Hoechst-33342 (for mouse lung slides), the slides were covered using an anti-fade mounting medium.

Human and mouse lung tissue sections were examined by a laser scanning confocal microscopy (Leica TCS SP5, Leica Microsystems GmbH) as previously described [47]. Five randomly selected fields of vision and a series of confocal optic sections were taken in each sample by using a Leica Plan APO 63x/1.30 objective lens. Each recorded image was taken using multichannel scanning and consisted of 2048 × 2048 pixels. To improve image quality and to obtain a high signal/noise ratio, each image from the series was signal-averaged.

For quantification of immunofluorescence, all mouse lung specimens of the different groups were immunolabeled simultaneously with identical conditions of fixation and dilutions of the primary and secondary antibodies. The iNos fluorescence intensity was measured in the regions of interest (ROIs) using a range of 0 – 255 grey values and normalized to Hoechst-33342 fluorescence intensity **(Figure 24)**. For each quantification procedure, a specific setting was established and kept constant in all measurements.

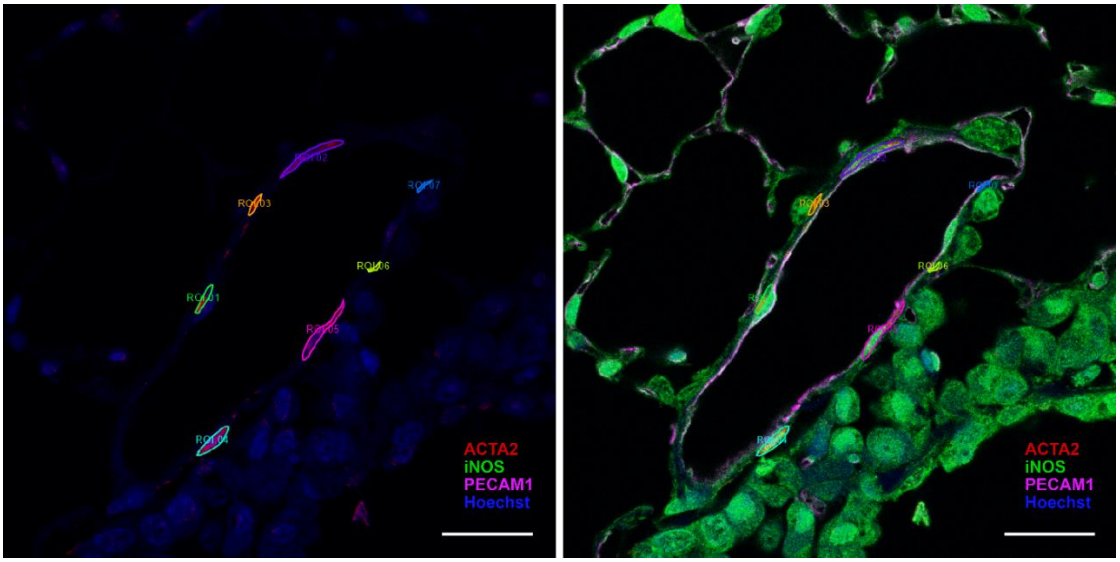

Figure 24. Representative images of assessing the iNOS fluorescence intensity in the mouse lung. Left image: the regions stained in red were circled as regions of interest (ROIs). Right image: the iNOS fluorescence intensity was assessed only on the ROIs. Scale bar = 20 µm. Abbreviation: ACTA2, alpha-smooth muscle actin. iNOS, inducible nitric oxide synthase. PECAM1, platelet endothelial cell adhesion molecule 1.

2.7 Statistical analyses

For the *in vitro* investigations in hPASMCs, experiments were conducted in technical replicates. The investigations in mPASMCs, mAEC2s, mFBs and human lung tissues samples were conducted in biological replicates. For *in vivo* experiments, each dot in the figures represents the result obtained from one individual mouse. Data were analyzed using the GraphPad Prism 9 software and visualized in scatterplots. The mean values for each group are represented by horizontal lines ± standard error of the mean (S.E.M.). Prior to statistical analyses, D'Agostino-Pearson omnibus normality tests were performed using the GraphPad Prism 9 software to measure skewness and kurtosis of the data [126]. For comparison between two groups, paired/unpaired Student's t-test was employed. For multiple comparisons, Dunnett's multiple-to-one procedure and Tukey's honestly significant difference tests were used to control the family-wise error-rate. An asterisk (*) denotes $p < 0.05$, which was considered statistically significant. Additionally, the significance of the interaction between the experimental factors was evaluated and its *p*-value is indicated in the graph.

3. Results

Seimetz *et al*. previously identified the inducible nitric oxide synthase (iNOS) as a driver of CS-induced pulmonary hypertension (PH) and emphysema development in mice [44]. In this article, the *iNos* gene expression was significantly upregulated in the pulmonary vessels but not in bronchi and alveolar septa of CS-exposed mouse lungs. By using chimeric mice, Seimetz *et al*. showed that CS-induced emphysema is dependent on *iNOS*-containing non-bone-marrow-derived (NBMD) cells. However, it is still difficult to pinpoint which *iNOS*-containing vascular NBMD cell type plays a critical role in the pathogenesis of CS-induced emphysema.

Against this background, the current work aimed 1) to investigate the iNOS expression in a vascular NBMD cell type – in pulmonary artery smooth muscle cells (PASMCs) upon CS exposure and 2) to determine the effect of iNOS-deletion in PASMCs on CS-induced emphysema development.

3.1 CSE exposure induces iNOS expression in human PASMCs (hPASMCs).

To confirm that iNOS was expressed in PASMCs and was induced upon CS, commercially available hPASMCs were seeded on culture dishes, exposed to cigarette smoke extract (CSE), and harvested for investigating mRNA and protein levels. The mRNA expression was examined by real-time quantitative reverse transcriptase polymerase chain reaction (qRT-PCR). The end-point amplicons were loaded on an agarose gel for electrophoresis to validate the specificity of the primers. The images demonstrated only a single band at 207 base pair (bp) in the well added with *iNOS* primer pairs. In the well added with primer pairs targeting *beta-2 microglobulin* (*B2M*) showed a single band at 128 bp **(Figure 25a)**. The results indicated that *iNOS* was induced in hPASMCs after 6-hour 3% cigarette smoke extract (CSE) exposure, whereas it was undetectable in hPASMCs upon 0% CSE exposure (only exposed with vehicle medium) **(Figure 25a)**. In line with the mRNA results, a significant increase of iNOS protein levels was observed in hPASMCs following a 6 hours of 3% and 5% CSE exposure (but only a tendency upon 1% CSE exposure), compared to those cultivated with vehicle medium. Additionally, iNOS protein expression in CSE-exposed PASMCs was increased in a dose-dependent manner **(Figure 25b)**.

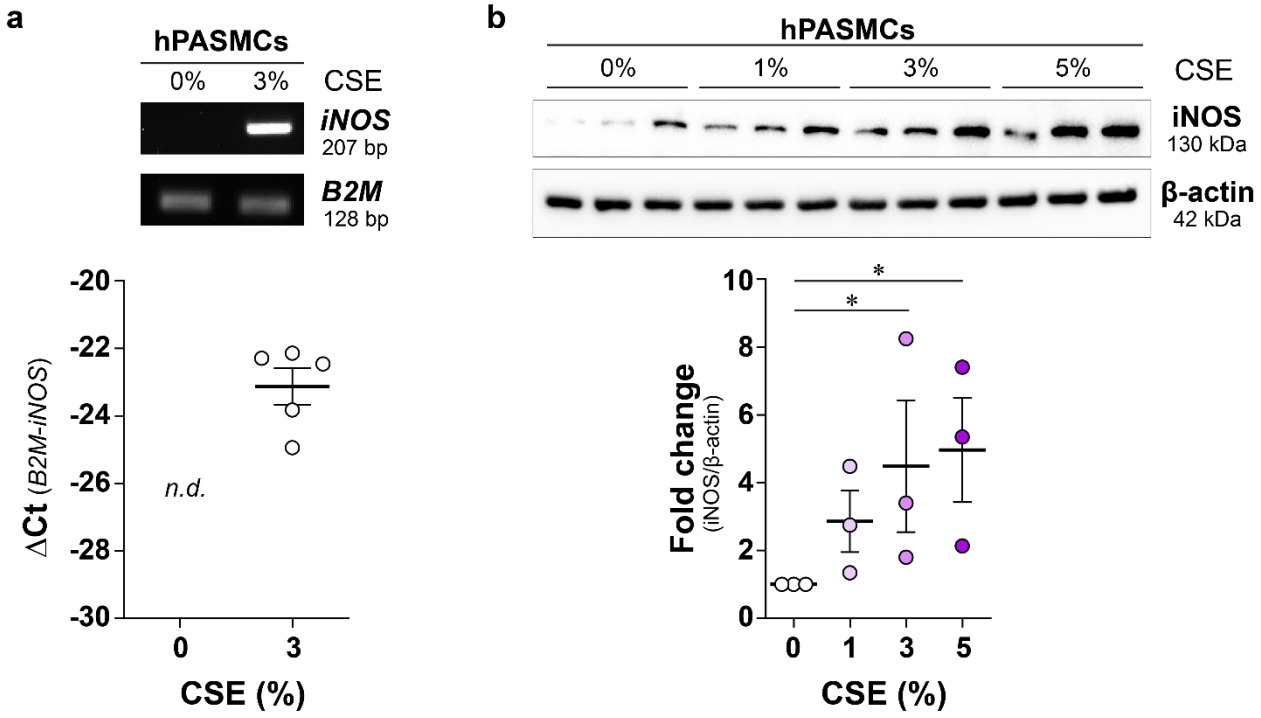

Figure 25. The mRNA and protein expression of iNOS in human pulmonary artery smooth muscle cells (hPASMCs) upon cigarette smoke extract (CSE) exposure. a, The representative image of qRT-PCR end-point analysis on agarose gel and the quantification of iNOS mRNA expression (n=5). **b,** The western blot image and the quantification of iNOS protein expression in hPASMCs upon the different concentrations of CSE exposure (n=3). Each dot represents a measurement in a sample from one technical replicate. The ratio of iNOS/β-actin in 1%, 3%, and 5% CSE-exposed samples was further normalized to the indicated 0% CSE-exposed samples. The mean value of each group is represented by a horizontal line ± standard error of the mean (S.E.M.). Statistical analysis: **b,** One-Way ANOVA with Dunnett's corrections was applied for *p*-value adjustment. An asterisk (*) denotes *p*-value < 0.05, which is considered statistically significant between the two groups. Abbreviations: hPASMCs, human pulmonary smooth muscle cells. CSE, cigarette smoke extract. iNOS, inducible nitric oxide synthase. B2M, beta-2 microglobulin.

3.2 Intracellular CSE-induced NO production is derived from iNOS in both human and mouse PASMCs.

After confirming that iNOS expression was upregulated in CSE-exposed PASMCs, nitric oxide (NO) production was investigated in these cells. In this regard, an intracellular NO detection probe, 4-Amino-5-Methylamino-2', 7'-Difluorofluorescein Diacetate (DAF-FM DA), was employed. Human PASMCs were probed with DAF-FM DA subsequent to 0% or 5% CSE exposure. The

results exhibited a significant increase in fluorescence intensity following CSE exposure, indicating a vast amount of NO was generated **(Figure 26a, b)**. To further verify if increased NO was derived from iNOS, a selective iNOS inhibitor, N^6-(1-Iminoethyl)-lysine (L-NIL), was exploited to hamper the enzyme activity. L-NIL does not affect NO production under basal conditions (0% CSE), but decreases CSE-induced NO formation **(Figure 26a, b)**.

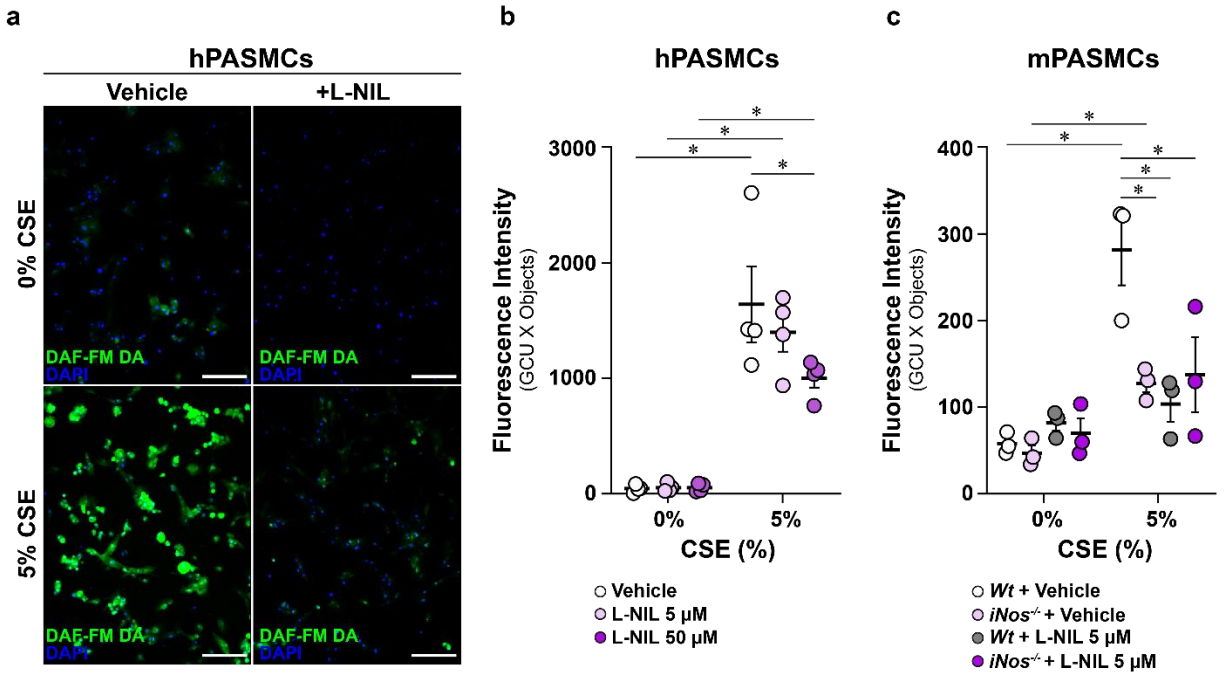

Figure 26. Intracellular NO detection in human and mouse pulmonary artery smooth muscle cells (PASMCs). a, Representative fluorescence images of the NO probe DAF-FM DA in hPASMCs upon CSE exposure with or without L-NIL pretreatment. Scale bar = 200 µm **b,** Quantification of the NO probe DAF-FM DA fluorescence intensity in hPASMCs upon 0% or 5% CSE exposure (n=4). **c,** Quantification of the NO probe DAF-FM DA fluorescence intensity in 0% or 5% CSE-exposed mPASMCs isolated from *Wt* or *iNos*$^{-/-}$ mice with or without L-NIL pretreatment (n=4).
Each dot represents a measurement in a sample obtained from technical replicates (hPASMCs) or from biological replicates (mPASMCs). The mean value of each group is represented by a horizontal line ± standard error of the mean (S.E.M.).
Statistical analysis: **b,** Two-Way ANOVA with an uncorrected *p*-value. **c,** Three-Way ANOVA with an uncorrected *p*-value. An asterisk (*) denotes a *p*-value < 0.05, which is considered statistically significant between the two groups. Abbreviations: hPASMCs, human pulmonary smooth muscle cells. mPASMCs, mouse pulmonary smooth muscle cells. L-NIL, N6-(1-Iminoethyl)-lysine, a selective iNOS inhibitor. CSE, cigarette smoke extract. DAF-FM DA, 4-Amino-5-Methylamino-2', 7'-Difluorofluorescein Diacetate, an NO intracellular probe. DAPI, 4′,6-diamidino-2-phenylindole. *Wt*, Wildtype. *iNos*$^{-/-}$, inducible nitric oxide synthase-knockout.

To consolidate the data obtained from hPASMCs, mouse PASMCs (mPASMCs) were isolated from wildtype (*Wt*) and *iNos*-knockout (*iNos*$^{-/-}$) mice. The cells were treated with L-NIL or the vehicle control prior to exposure of 0% or 5% CSE. Then, NO production was measured by DAF-FM DA. The results demonstrated a significant increased fluorescent intensity in 5% CSE-exposed mPASMCs isolated from *Wt* and *iNos*$^{-/-}$ mice with vehicle pretreatment. However, compared with mPASMCs isolated from *Wt* mice, mPASMCs isolated from *iNos*$^{-/-}$ mice showed a decreased NO production in mPASMCs upon CSE exposure. The NO level in the L-NIL-treated mPASMCs, either isolated from *Wt* or *iNos*$^{-/-}$ mice, was similar as vehicle-treated mPASMCs isolated from *iNos*$^{-/-}$ mice **(Figure 26c)**.

3.3 Deletion of *iNos* protects mPASMCs and mouse alveolar type 2 epithelial cells (mAEC2s) against CSE-induced damage.

Going beyond, we hypothesized that deletion of *iNos* in mPASMCs prevents CSE-induced damage. As a comparison, additionally, two other types of pulmonary NBMD cells, mouse alveolar type 2 epithelial cells (mAEC2s) and mouse fibroblasts (mFBs) from *Wt* and *iNos*$^{-/-}$ mice were isolated. A sulforhodamine B (SRB) assay was used to determine the cell survival after CSE exposure. The results showed that CSE decreased the percentage of cell survival in mPASMCs, mAEC2s and mFBs isolated from *Wt* mice **(Figure 27a-27c)**. Consistent with the hypothesis, mPASMCs isolated from *iNos*$^{-/-}$ mice showed less CSE-induced cell damage than mPASMCs isolated from *Wt* mice **(Figure 27a)**. Similarly, the survival of CSE-exposed AEC2 isolated from *iNos*$^{-/-}$ mice was significant higher than the survival of those isolated from *Wt* mice **(Figure 27b)**. Deletion of *iNos* in mFB, nevertheless, did not have significant protective effects against CSE **(Figure 27c).**

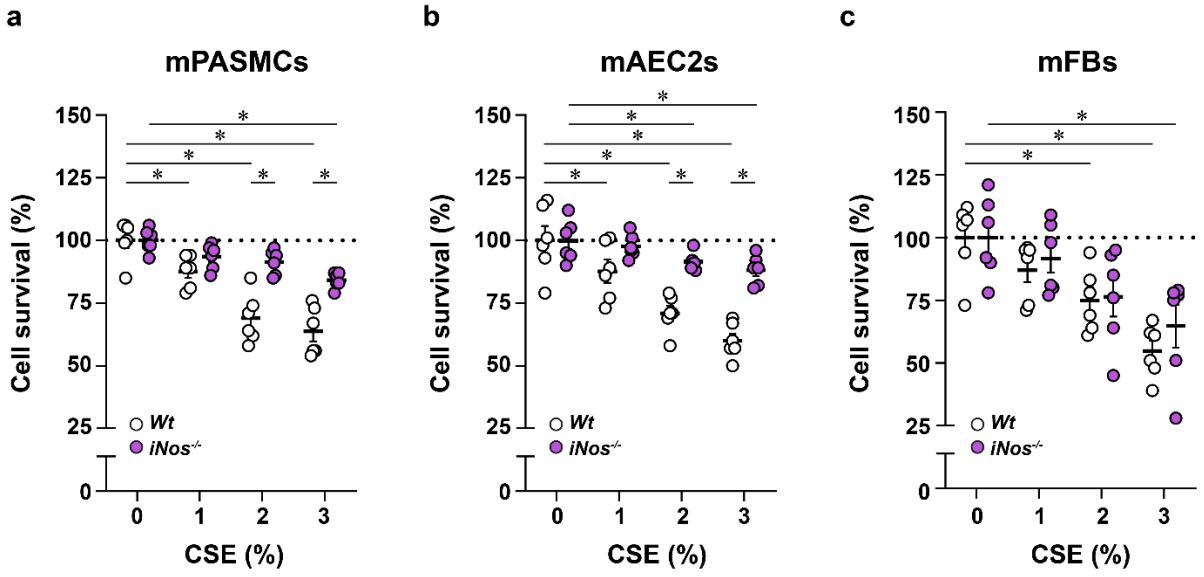

Figure 27. The effect of *iNos*-deletion on cell survival of different pulmonary cells upon cigarette smoke extract (CSE) exposure. a, Mouse pulmonary artery smooth muscle cells (mPASMCs) isolated from *Wt* and *iNos*$^{-/-}$ mice (n=6/group). **b,** Mouse alveolar type 2 epithelial cells (mAEC2s) isolated from *Wt* and *iNos*$^{-/-}$ mice (n=6/group). **c,** Mouse fibroblasts (mFBs) isolated from *Wt* and *iNos*$^{-/-}$ mice (n=6/group).
Each dot represents a measurement in a sample obtained from biological replicates. The mean value of each group is represented by a horizontal line ± standard error of the mean (S.E.M.). Statistical analysis: **a-c**, One-Way ANOVA with Dunnett's correction was applied for *p*-value adjustment when comparing the indicated concentration of CSE exposure to 0% CSE-exposed groups. For comparison between *Wt* and *iNos*$^{-/-}$ cells within the same condition, a two-tailed Student's t-test was used. An asterisk (*) denotes a *p*-value < 0.05, which is considered statistically significant between the two groups. Abbreviations: CSE, cigarette smoke extract. *Wt*, Wildtype. *iNos*$^{-/-}$, inducible nitric oxide synthase-knockout. mPASMCs, mouse pulmonary smooth muscle cells. mAEC2s, mouse alveolar type 2 epithelial cells. mFBs, mouse fibroblasts.

3.4 3-nitrotyrosine is present in the pulmonary vessels and alveolar septal wall of smokers with COPD.

CS-induced iNOS and NO are involved in the 3-NT formation pathway **(Figure 28a)**. Therefore, 3-NT levels in human lungs obtained from healthy donors, smokers without COPD and smokers with COPD were investigated. Analysis of lung homogenate revealed increased 3-NT levels in smokers with COPD, in comparison of 3-NT level in healthy donors or smokers without COPD **(Figure 28b)**. To localize 3-NT formation in the lung, immunofluorescence staining was

performed. The images acquired from confocal microscopy showed that 3-NT immunoreactivity was present in both pulmonary vessels and alveolar septa of smokers with COPD (**Figure 28c)**.

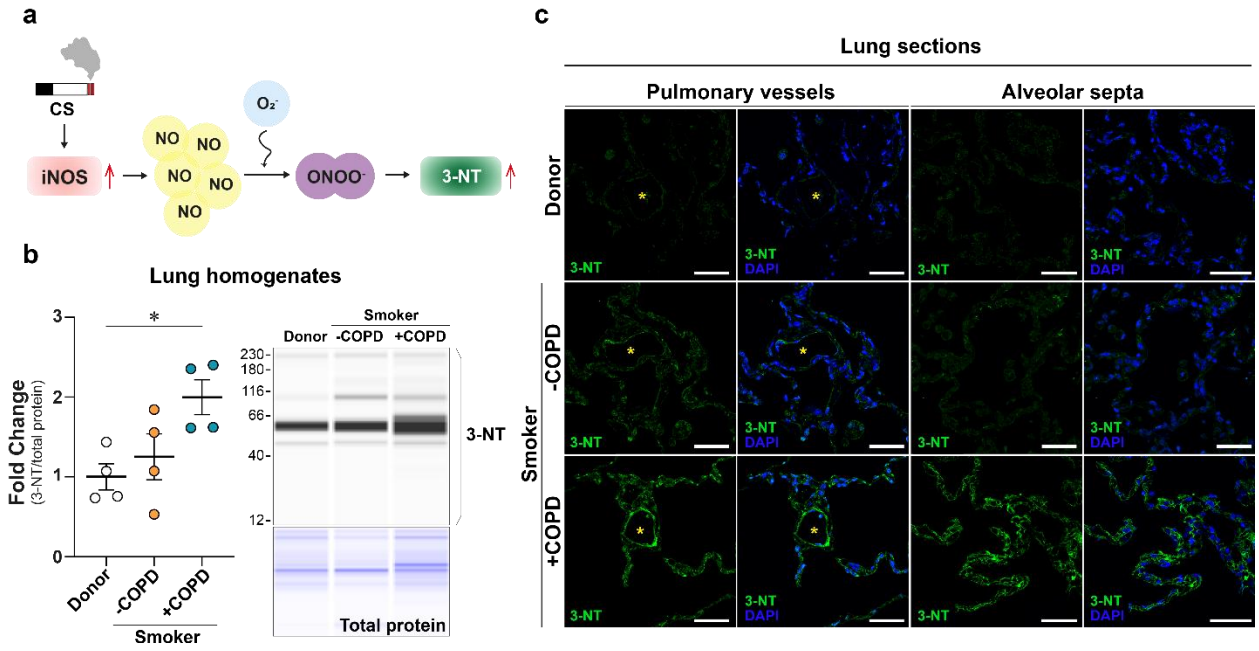

Figure 28. 3-nitrotyrosine levels in lung tissue from healthy donors and smokers without and with COPD. a, Graphical representation of the pathway of 3-NT formation. **b,** Quantification of 3-NT levels in lung homogenate samples from healthy donors (Donor), smokers without COPD (Smoker - COPD) and smokers with COPD (Smoker + COPD) (n=4/group, left-panel) and the representative lane-views from capillary-based protein immunoassay (right-panel). Each dot represents a measurement in a sample obtained from one human individual. The mean value of each group is represented by a horizontal line ± standard error of the mean (S.E.M.). **c,** Localization of 3-NT formation in pulmonary vessels and alveolar septa of donors, smokers without and with COPD. Scale bars = 50 µm. Yellow asterisks depict pulmonary vessels.
Statistical analysis: **b,** One-Way ANOVA with Tukey's corrections was applied for *p*-value adjustment. Abbreviations: CS, Cigarette smoke. iNOS, inducible nitric oxide. NO. nitric oxide. O_2^-, superoxide. $ONOO^-$, peroxynitrite. 3-NT, 3-nitrotyrosine. COPD, chronic obstructive pulmonary disease. DAPI, 4′,6-diamidino-2-phenylindole.

3.5 Characterization of *Acta2*$^{+}$ cell-specific *iNos*-knockout mice upon chronic CS exposure.

3.5.1 The effect of 3 months of CS exposure in *Acta2*$^{+}$ cell-specific *iNos*-knockout mice.

3.5.1.1 No significant changes in body weight and heart rate were observed upon CS exposure or tamoxifen administration.

Neither CS exposure nor *Acta2*$^{+}$ cell-specific *iNos*-deletion altered body weight **(Figure 29a)**. Before performing non-invasive transthoracic echocardiography, the heart rates of the anesthetized mice were measured, indicating 400 – 600 beats per minute (BPM) in all experimental groups. There were no significant differences between the groups **(Figure 29b)**.

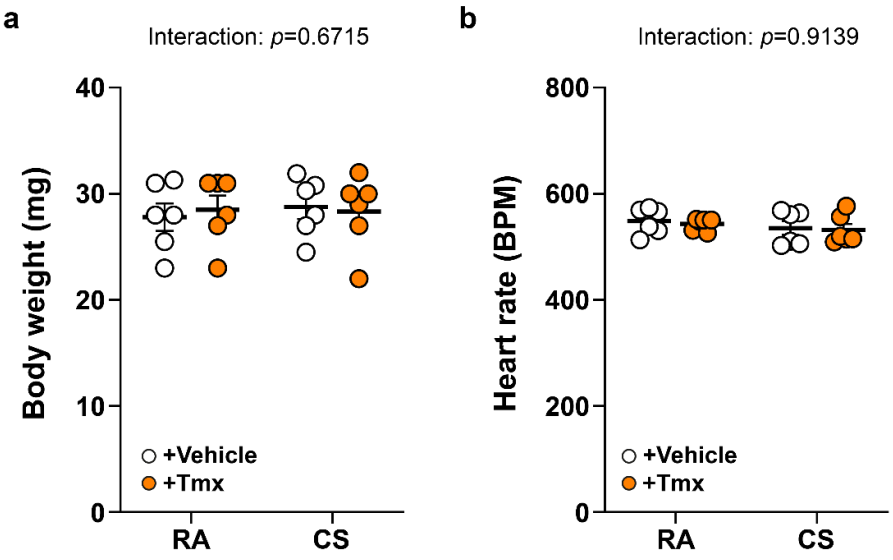

Figure 29. Measurement of body weight and heart rate in transgenic mice after 3 months of room air (RA) or cigarette smoke (CS) exposure. a, Body weight of the transgenic mice (n=6/group). **b,** Heart rate of anesthetized mice, measured before non-invasive transthoracic echocardiography (n=6/group).
Each dot represents a measurement in one mouse. The mean value of each group is represented by a horizontal line ± standard error of the mean (S.E.M.). Values from the mice administrated with vehicle (+Vehicle) are given as white dots, whereas those with tamoxifen (+Tmx) are shown as orange dots. Statistical analysis: Two-Way ANOVA with an uncorrected *p*-value. The interaction between the experimental factors is evaluated and the *p*-value is indicated in the graph. Abbreviations: RA, room air. CS, cigarette smoke. BPM, beats per minute.

3.5.1.2 Acta2^{+} cell-specific iNos-knockout mice developed PH after 3 months of CS exposure.

To determine whether the mice develop PH after 3 months of CS exposure, right ventricular systolic pressure (RVSP) was measured using a Millar catheter. The results demonstrated a significant increase of RVSP in both CS-exposed mouse groups **(Figure 30a)**. In line with this finding, the assessments obtained from the non-invasive transthoracic echocardiography showed that tricuspid annular plane systolic excursion (TAPSE), for evaluation of RV function, was markedly decreased in CS-exposed mice, independently of *iNos*-deletion in *Acta2*$^{+}$ cells **(Figure 30b)**. In addition, the ratio of pulmonary artery acceleration time (PAT) and pulmonary artery ejection time (PET), an inverse indicator of RV afterload, was significantly reduced in all CS-exposed mice **(Figure 30c)**.

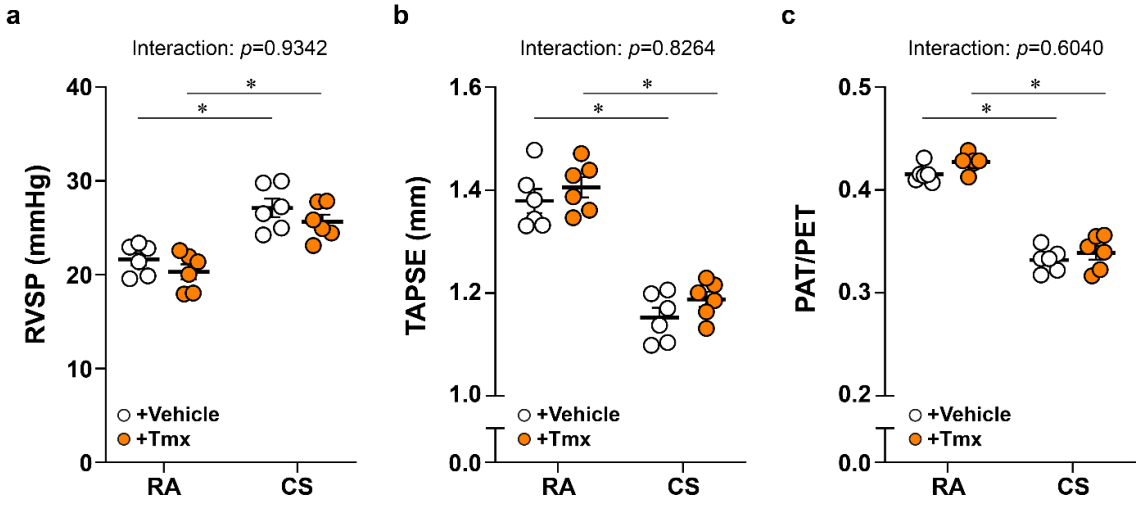

Figure 30. Hemodynamic and right ventricular function measurement in transgenic mice after 3 months of room air (RA) or cigarette smoke (CS) exposure. a, RVSP measured by right heart catheterization in mice exposed to RA or CS exposure for 3 months (n=6/group). **b,** Measurement of TAPSE in mice exposed to RA or CS exposure for 3 months (n=6/group). **c,** Measurement of PAT/PET ratio in mice exposed to RA/CS exposure for 3 months (n=6/group). Each dot represents a measurement in one mouse. The mean value of each group is represented by a horizontal line ± standard error of the mean (S.E.M.). Values from the mice administrated with vehicle (+Vehicle) are given as white dots, whereas those with tamoxifen (+Tmx) are shown as orange dots.
Statistical analysis: Two-Way ANOVA with an uncorrected *p*-value. The interaction between the experimental factors is evaluated and the *p*-value is indicated in each graph. An asterisk (*) denotes a *p*-value < 0.05, which is considered statistically significant between the two groups. Abbreviations: RVSP, right ventricular systolic pressure. TAPSE, tricuspid annular plane systolic excursion. PAT/PET, the ratio of pulmonary artery acceleration time and pulmonary artery ejection time. RA, room air. CS, cigarette smoke.

3.5.1.3 The heart function in Acta2^{+} cell-specific iNos-knockout mice was declined after 3 months of CS exposure.

The heart function of mice exposed to 3 months of RA/CS exposure was assessed using a non-invasive transthoracic echocardiography. Deletion of *iNos* in *Acta2*$^{+}$ cell affected neither cardiac index (CI) nor ejection fraction (EF), but CS exposure decreased CI **(Figure 31a)** and EF **(Figure 31b)**.

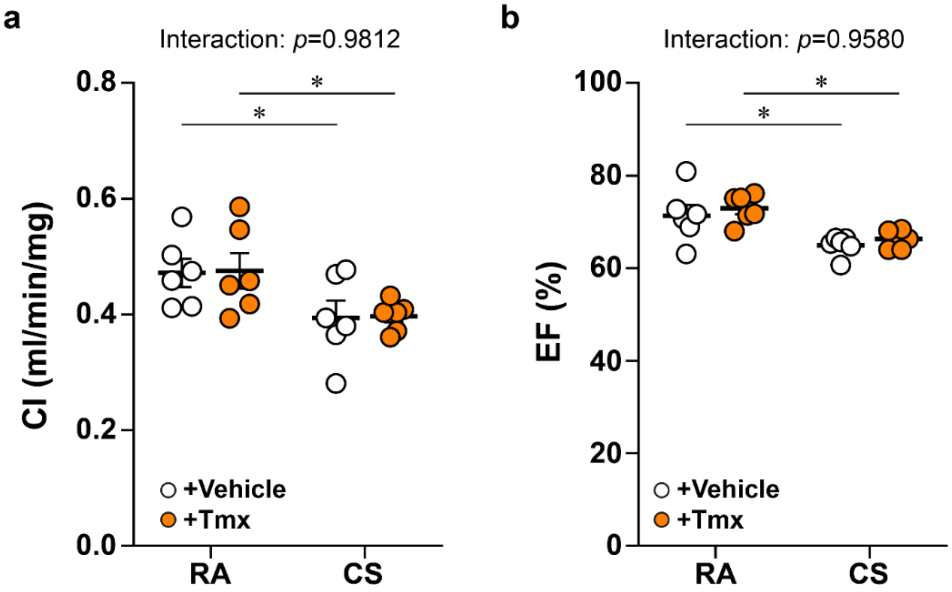

Figure 31. Heart function measurement in transgenic mice after 3 months of room air (RA) or cigarette smoke (CS) exposure. a, Measurement of CI by a non-invasive transthoracic echocardiography (n=6/group). **b,** Measurement of EF by a non-invasive transthoracic echocardiography (n=6/group), shown in percentage calculated from the *formula 2* mentioned in the method section.
Each dot represents a measurement in a mouse. The mean value of each group is represented by a horizontal line ± standard error of the mean (S.E.M.). Values from the mice administrated with vehicle (+Vehicle) are given as white dots, whereas those with tamoxifen (+Tmx) are shown as orange dots.
Statistical analysis: Two-Way ANOVA with an uncorrected *p*-value. The interaction between the experimental factors is evaluated and the *p*-value is indicated in each graph. An asterisk (*) denotes a *p*-value < 0.05, which is considered statistically significant between the two groups.
Abbreviations: CI, cardiac index. EF, ejection fraction. RA, room air. CS, cigarette smoke.

3.5.1.4 Acta2^{+} cell-specific iNos-knockout mice developed right heart hypertrophy after 3 months of CS exposure.

To investigate whether the mice develop right heart hypertrophy and RV dilatation, right ventricular free wall thickness (RVWT) and right ventricular internal diameter (RVID) were assessed by a non-invasive transthoracic echocardiography. The results indicated a significantly increase in RVWT and decreased RVID in mice after 3 months of CS exposure. **(Figure 32a** and **32b)**. Assessment of the RV hypertrophy using Fulton index further confirmed the findings from the non-invasive transthoracic echocardiography **(Figure 32c).**

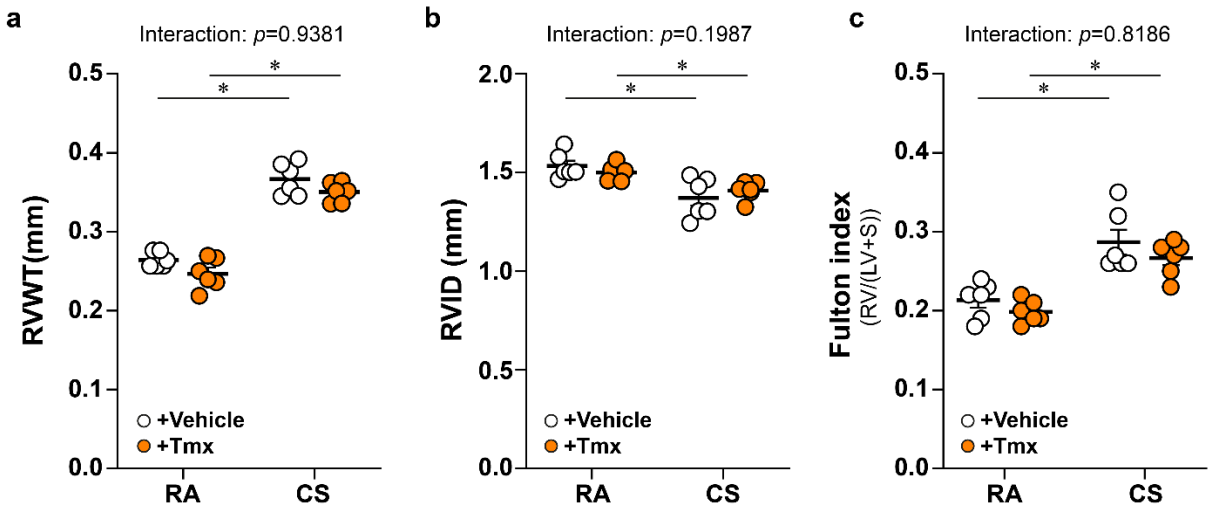

Figure 32. Right ventricular hypertrophy assessment in transgenic mice after 3 months of room air (RA) or cigarette smoke (CS) exposure. a, Measurement of RVWT by a non-invasive transthoracic echocardiography (n=6/group). **b,** Measurement of RVID by a non-invasive transthoracic echocardiography (n=6/group). **c,** Measurement of Fulton index, shown as the ratio of the weight of RV and the weight of LV+S (n=6/group). Each dot represents a measurement in a mouse. The mean value of each group is represented by a horizontal line ± standard error of the mean (S.E.M.). Values from the mice administrated with vehicle (+Vehicle) are given as white dots, whereas those with tamoxifen (+Tmx) are shown as orange dots.
Statistical analysis: Two-Way ANOVA with an uncorrected *p*-value. The interaction between the experimental factors is evaluated and the *p*-value is indicated in each graph. An asterisk (*) denotes a *p*-value < 0.05, which is considered statistically significant between the two groups. Abbreviations: RVWT, right ventricular free wall thickness. RVID, right ventricular internal diameter. RV, right ventricle. LV, left ventricle. S, septum. RA, room air exposure. CS, cigarette smoke exposure.

3.5.1.5 CS-exposed Acta2^{+} cell-specific iNos-knockout mice showed an increased lung compliance.

To determine the lung function *in vivo*, a flexiVent system was used. The mouse lungs were step-wise inflated with air from the pressure of 10 cmH_2O to 30 cmH_2O, followed by deflation in a similar way to generate a pressure-volume (PV) loop. The results demonstrated a left-shifted loop in CS-exposed mice, independent of *iNos*-knockout in *Acta2*$^{+}$ cells **(Figure 33a)**. Consistently, CS exposure significantly increased pulmonary static compliance in both mouse groups **(Figure 33b)**.

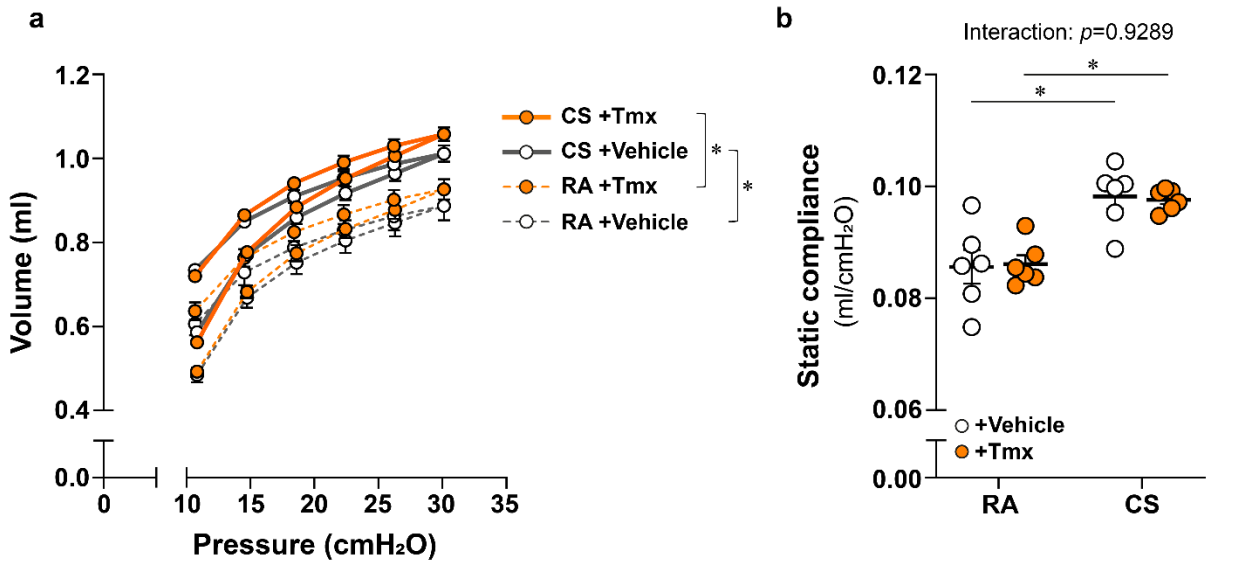

Figure 33. *In vivo* lung function measurements in transgenic mice after 3 months of room air (RA) or cigarette smoke (CS) exposure. a, Pressure-volume (PV) loops (n=6/group). Each dot depicts a mean value of each group, which is represented by a horizontal line ± standard error of the mean (S.E.M.). **b,** Measurement of static lung compliance (n=6/group).
Each dot depicts a measurement in a mouse. The mean value of each group is represented by a horizontal line ± standard error of the mean (S.E.M.). Values from the mice administrated with vehicle (+Vehicle) are given as white dots, whereas those with tamoxifen (+Tmx) are shown as orange dots.
Statistical analysis: Two-Way ANOVA with an uncorrected *p*-value. **b,** The interaction between the experimental factors is evaluated and the *p*-value is indicated in the graph. An asterisk (*) denotes a *p*-value < 0.05, which is considered statistically significant between the two groups.
Abbreviations: RA, room air exposure. CS, cigarette smoke exposure.

3.5.1.6 Acta2^{+} cell-specific iNos-knockout CS-exposed mouse lungs showed a partial protection against pulmonary emphysema.

The *in vivo* lung function data were validated in histology and design-based stereology by the analyses of alveolar morphometry and the assessments of alveoli number. **Figure 34a** exhibits representative images of the alveolar septa of a mouse from each group. In line with the lung function data, the air space in alveolar septa from CS-exposed mice was larger than in RA-exposed mice **(Figure 34b)**. The alveolar septal wall thickness was reduced in CS-exposed compared with corresponding RA-exposed mice **(Figure 34c)**. Interestingly, CS did not alter mean linear intercept (MLI) of *Acta2*$^{+}$ cell-specific *iNos*-knockout mice, but MLI was only increased in alveolar septa of CS-exposed, vehicle-administrated mice. **(Figure 34d)**. Consistently, ablation of *iNos* in *Acta2*$^{+}$ cells prevented the loss of alveoli after 3 months of CS exposure **(Figure 34e)**.

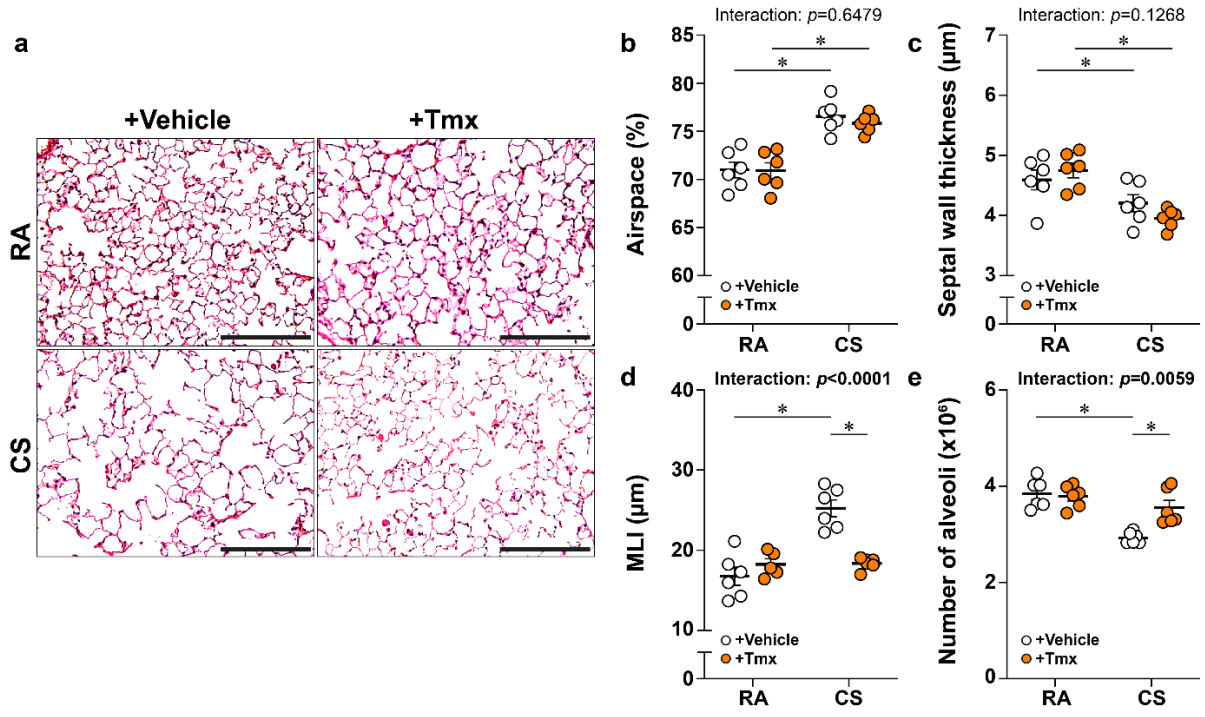

Figure 34. Alveolar morphometry and design-based stereological analysis in transgenic mice after 3 months of room air (RA) or cigarette smoke (CS) exposure. a, Representative images of alveolar septa in the different groups. Scale bars = 200 µm. **b,** Quantification of airspace in alveolar septa of each group, shown in percentage (n=6/group). **c,** Quantification of alveolar septal wall thickness of each group (n=6/group). **d,** Quantification of MLI in alveolar septa of each group (n=6/group). **e,** Number of alveoli in the lungs of each group.

Each dot represents an assessment in a mouse. The mean value of each group is represented by a horizontal line ± standard error of the mean (S.E.M.). Values from the mice administrated with vehicle (+Vehicle) are given as white dots, whereas those with tamoxifen (+Tmx) are shown as orange dots.
Statistical analysis: Two-Way ANOVA with an uncorrected *p*-value. The interaction between the experimental factors is evaluated and the *p*-value is indicated in each graph. An asterisk (*) denotes a *p*-value < 0.05, which is considered statistically significant between the two groups. Abbreviations: RA, room air exposure. CS, cigarette smoke exposure. MLI, mean linear intercept.

3.5.2 The effect on *Acta2*$^{+}$ cell-specific *iNos*$^{-/-}$ mice after 8 months of CS exposure.

3.5.2.1 No significant changes in body weight and heart rate were observed upon CS exposure or tamoxifen administration.

The transgenic mice exposed to RA or CS for 8 months showed no significant differences in body weight. The same results were observed when comparing vehicle-/tamoxifen-administrated mice **(Figure 35a)**. Before performing non-invasive transthoracic echocardiography, heart rates of the anesthetized mice were measured. Neither CS exposure, nor tamoxifen administration significantly influenced the heart rate. **(Figure 35b)**.

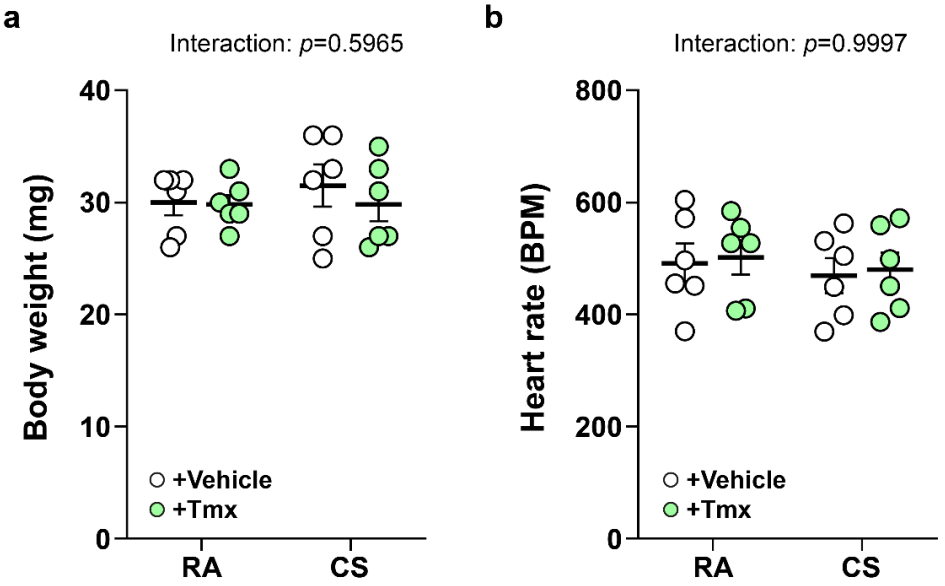

Figure 35. Measurement of the body weight and heart rate in transgenic mice after 8 months of room air (RA) or cigarette smoke (CS) exposure. a, Body weight of the transgenic mice after 8 months of RA or CS exposure (n=6/group). **b,** Heart rate of anesthetized mice after

8 months of RA or CS exposure, measured before conducting non-invasive transthoracic echocardiography (n=6/group).
Each dot represents a measurement in one mouse. The mean value of each group is represented by a horizontal line ± standard error of the mean (S.E.M.). Values from the mice administrated with vehicle (+Vehicle) are given as white dots, whereas those with tamoxifen (+Tmx) are shown as green dots.
Statistical analysis: Two-Way ANOVA with an uncorrected *p*-value. The interaction between the experimental factors is evaluated and the *p*-value is indicated in each graph. Abbreviations: RA, room air. CS, cigarette smoke. BPM, beats per minute.

3.5.2.2 Acta2^{+} cell-specific iNos-knockout mice developed PH after 8 months of CS exposure.

The results obtained from right heart catheterization demonstrated an increased RVSP in all transgenic mice after 8 months of CS exposure **(Figure 36a)**. The measurements of TAPSE and the ratio of PAT/PET showed a significant decrease **(Figure 36b, 36c)**. Such a decrease was observed in CS-exposed mice, independent of *iNos*-deletion in *Acta2*$^{+}$ cells.

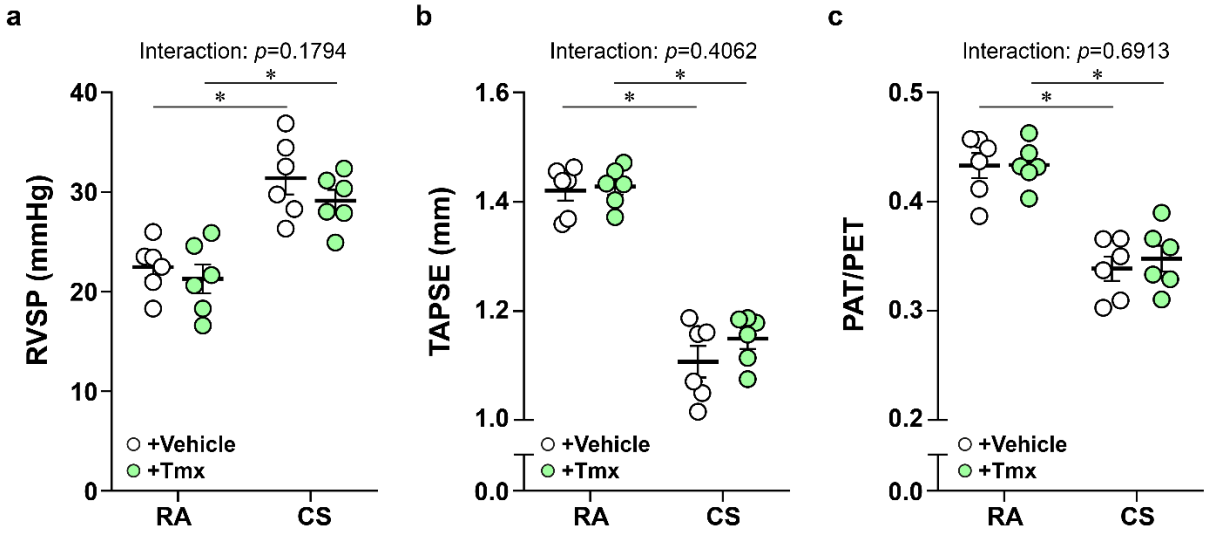

Figure 36. Hemodynamic and right ventricular function assessment in transgenic mice after 8 months of room air (RA) or cigarette smoke (CS) exposure. a, RVSP measured by right heart catheterization in mice exposed to RA/CS exposure for 8 months (n=6/group). **b,** Measurement of TAPSE in mice exposed to RA/CS exposure for 8 months (n=6/group). **c,** Measurement of PAT/PET ratio in mice exposed to RA/CS exposure for 8 months (n=6/group). Each dot represents a measurement in a mouse. The mean value of each group is represented by a horizontal line ± standard error of the mean (S.E.M.). Values from the mice administrated with vehicle (+Vehicle) are given as white dots, whereas those with tamoxifen (+Tmx) are shown as green dots.

Statistical analysis: Two-Way ANOVA with an uncorrected *p*-value. The interaction between the experimental factors is evaluated and the *p*-value is indicated in each graph. An asterisk (*) denotes a *p*-value < 0.05, which is considered statistically significant between the two groups. Abbreviations: RVSP, right ventricular systolic pressure. TAPSE, tricuspid annular plane systolic excursion. PAT/PET, ratio of pulmonary artery acceleration time and pulmonary artery ejection time. RA, room air. CS, cigarette smoke.

3.5.2.3 Declined heart function in Acta2^{+} cell-specific iNos-knockout mice was observed upon 8 months of CS exposure.

Decreased CI and EF were observed in CS-exposed mice compared with RA-exposed mice. *Acta2*$^{+}$ cell-specific *iNos*-knockout mice in both RA and CS conditions showed no differences in CI and EF from the corresponding control group **(Figure 37a, 37b)**.

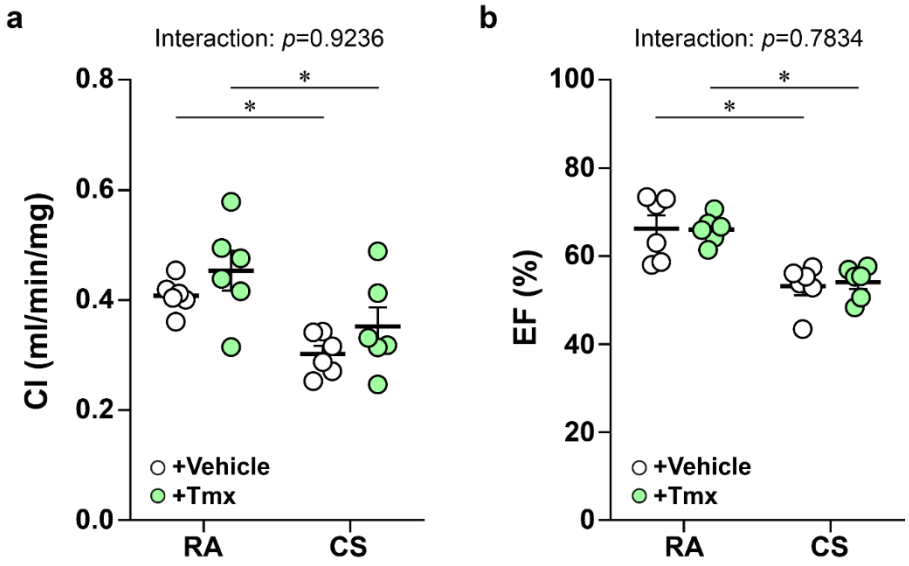

Figure 37. Heart function measurement in transgenic mice after 8 months of room air (RA) or cigarette smoke (CS) exposure. a, Measurement of CI by non-invasive transthoracic echocardiography (n=6/group). **b,** Measurement of EF by non-invasive transthoracic echocardiography, shown in percentage (n=6/group).
Each dot represents a measurement in one mouse. The mean value of each group is represented by a horizontal line ± standard error of the mean (S.E.M.). Values from the mice administrated with vehicle (+Vehicle) are given as white dots, whereas those with tamoxifen (+Tmx) are shown as green dots.
Statistical analysis: Two-Way ANOVA with an uncorrected *p*-value. The interaction between the experimental factors is evaluated and the *p*-value is indicated in each graph. An asterisk (*) denotes a *p*-value < 0.05, which is considered statistically significant between the two groups.

Abbreviations: CI, cardiac index. EF, ejection fraction. RA, room air exposure. CS, cigarette smoke exposure.

3.5.2.4 Acta2^{+} cell-specific iNos-knockout mice developed right heart hypertrophy after 8 months of CS exposure.

After 8 months of CS exposure, RVWT was significantly increased in all transgenic mice independent of *iNos*-deletion in *Acta2*$^{+}$ cells **(Figure 38a)**. RVID has declined in CS-exposed transgenic mice compared to RA-exposed transgenic mice **(Figure 38b)**. The obtained results were in line with Fulton index assessment, in which transgenic mice showed increased values after 8 months of CS exposure **(Figure 38c)**.

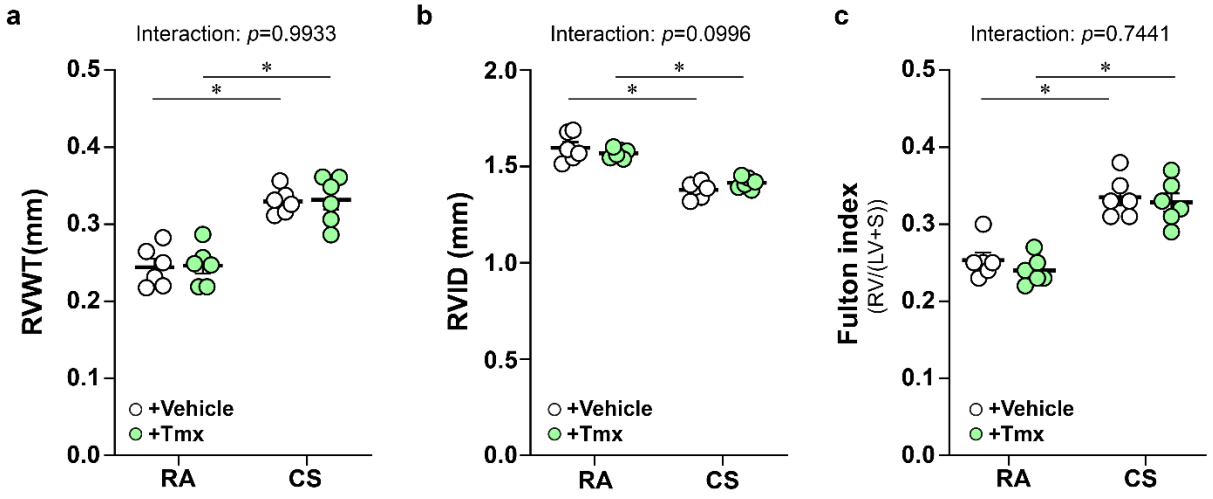

Figure 38. Right ventricular hypertrophy assessment in transgenic mice after 8 months of room air (RA) or cigarette smoke (CS) exposure. a, Measurement of RVWT by a non-invasive transthoracic echocardiography (n=6/group). **b,** Measurement of RVID by a non-invasive transthoracic echocardiography (n=6/group). **c,** Measurement of Fulton index, shown as the ratio of the weight of RV and the weight of LV+S (n=6/group).
Each dot represents a measurement in one mouse. The mean value of each group is represented by a horizontal line ± standard error of the mean (S.E.M.). Values from the mice administrated with vehicle (+Vehicle) are given as white dots, whereas those with tamoxifen (+Tmx) are shown as green dots.
Statistical analysis: Two-Way ANOVA with an uncorrected *p*-value. The interaction between the experimental factors is evaluated and the *p*-value is indicated in each graph. An asterisk (*) denotes a *p*-value < 0.05, which is considered statistically significant between the two groups.
Abbreviations: RVWT, right ventricular free wall thickness. RVID, right ventricular internal diameter. RA, room air. CS, cigarette smoke. RV, right ventricle. LV, left ventricle. S, septum.

3.5.2.5 CS-exposed Acta2^{+} cell-specific iNos-knockout mice showed a declined lung function.

The lung function results revealed left-shifted PV loops in transgenic mice after 8 months of CS exposure (**Figure 39a**). Pulmonary static compliance was significantly increased in CS-exposed mice, with no significant differences between vehicle-/tamoxifen-administrated mice **(Figure 39b)**.

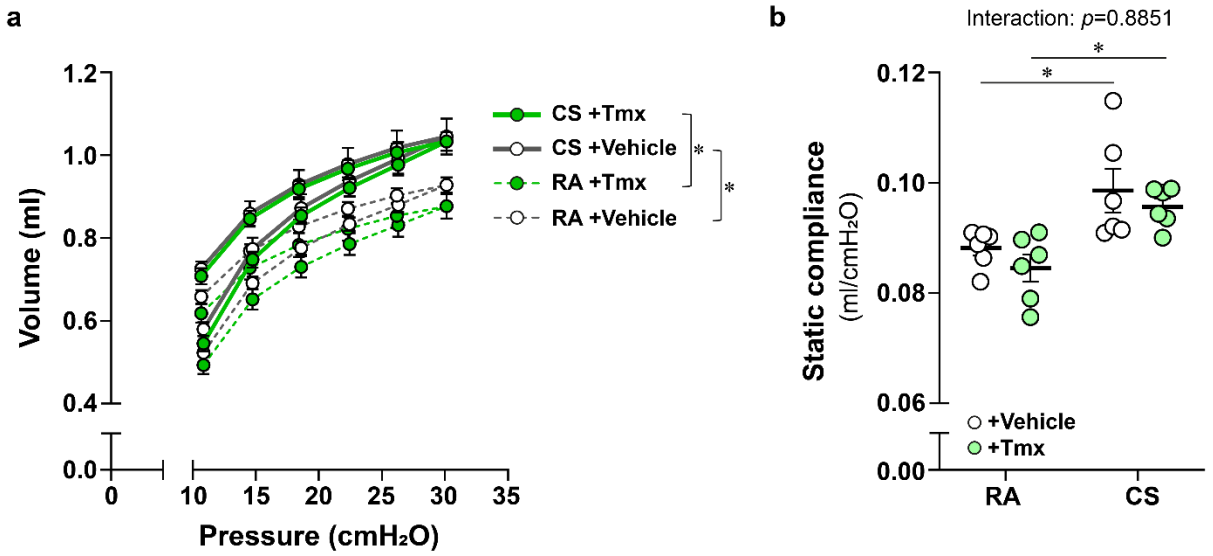

Figure 39. *In vivo* lung function measurements in transgenic mice after 8 months of room air (RA) or cigarette smoke (CS) exposure. a, Pressure-Volume (PV) loops. Each dot represents a mean value of each group (n=6/group), which is represented by a horizontal line ± standard error of the mean (S.E.M.). **b,** Measurement of static lung compliance (n=6/group). Each dot represents a measurement in one mouse. The mean value of each group is represented by a horizontal line ± standard error of the mean (S.E.M.). Values from the mice administrated with vehicle (+Vehicle) are given as white dots, whereas those with tamoxifen (+Tmx) are shown as green dots.
Statistical analysis: Two-Way ANOVA with an uncorrected *p*-value. **b,** The interaction between the experimental factors is evaluated and the *p*-value is indicated in the graph. An asterisk (*) denotes a *p*-value < 0.05, which is considered statistically significant between the two groups. Abbreviations: RA, room air. CS, cigarette smoke.

3.5.2.6 Acta2^{+} cell-specific iNos-knockout CS-exposed mouse lungs showed a marked destruction of alveolar septa.

Several emphysematous lesions were observed in alveolar septa of CS-exposed mice, regardless if *iNos* was deleted in *Acta2*$^{+}$ cells or not **(Figure 40a)**. Air space was markedly increased, whereas

alveolar septal wall thickness was significantly decreased in CS-exposed mice **(Figure 40b** and **40c)**. MLI, which was partially preserved in the lungs *Acta2*$^{+}$ cell-specific *iNos*-knockout mice after 3 months of CS exposure, showed no obvious difference between vehicle-/tamoxifen-administrated mice **(Figure 40d)**. These results were confirmed by the stereological analysis. The alveoli numbers declined in the mice after 8 months of CS exposure, independent of *iNos*-deletion in *Acta2*$^{+}$ cells **(Figure 40e)**.

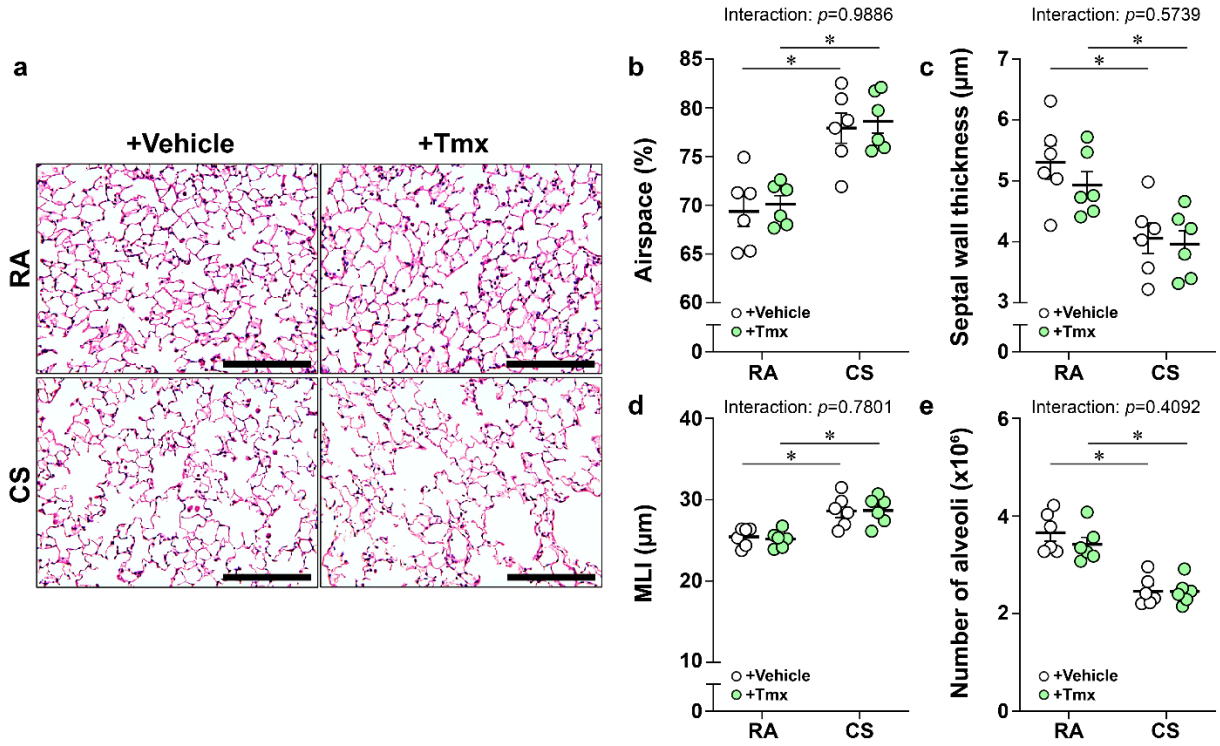

Figure 40. Alveolar morphometry and design-based stereological analysis in transgenic mice after 8 months of room air (RA) or cigarette smoke (CS) exposure. a, Representative images of alveolar septa in different groups. Scale bars = 200 µm. **b,** Quantification of airspace in alveolar septa of each group, shown in percentage (n=6/group). **c,** Quantification of alveolar septal wall thickness of each group (n=6/group). **d,** Quantification of MLI in alveolar septa of each group. **e,** Number of alveoli in the lungs of each group (n=6/group). Each dot represents an assessment in a mouse. The mean value of each group is represented by a horizontal line ± standard error of the mean (S.E.M.). Values from the mice administrated with vehicle (+Vehicle) are given as white dots, whereas those with tamoxifen (+Tmx) are shown as green dots.
Statistical analysis: Two-Way ANOVA with an uncorrected *p*-value. The interaction between the experimental factors is evaluated and the *p*-value is indicated in each graph. An asterisk (*) denotes a *p*-value < 0.05, which is considered statistically significant between the two groups. Abbreviations: RA, room air. CS, cigarette smoke. MLI, mean linear intercept.

3.5.3 *Acta2*$^{+}$ cell-specific *iNos*-knockout efficiency in the mouse lungs after 8 months of CS exposure.

To confirm the efficiency of tamoxifen-induced *iNos*-deletion in transgenic mice, immunofluorescence staining was performed in paraffin-embedded slides. An antibody against PECAM1 was used to locate pulmonary vessel. The results showed that iNos immunoreactivity was present in vehicle-administrated mouse lungs. However, it was absent in the area immunoreactive for ACTA2 in tamoxifen-administrated mouse lungs, even after a duration of 8 months **(Figure 41a)**. Immunofluorescence intensity of iNOS was approximately 3-fold decreased in tamoxifen-administrated mouse lungs **(Figure 41b)**.

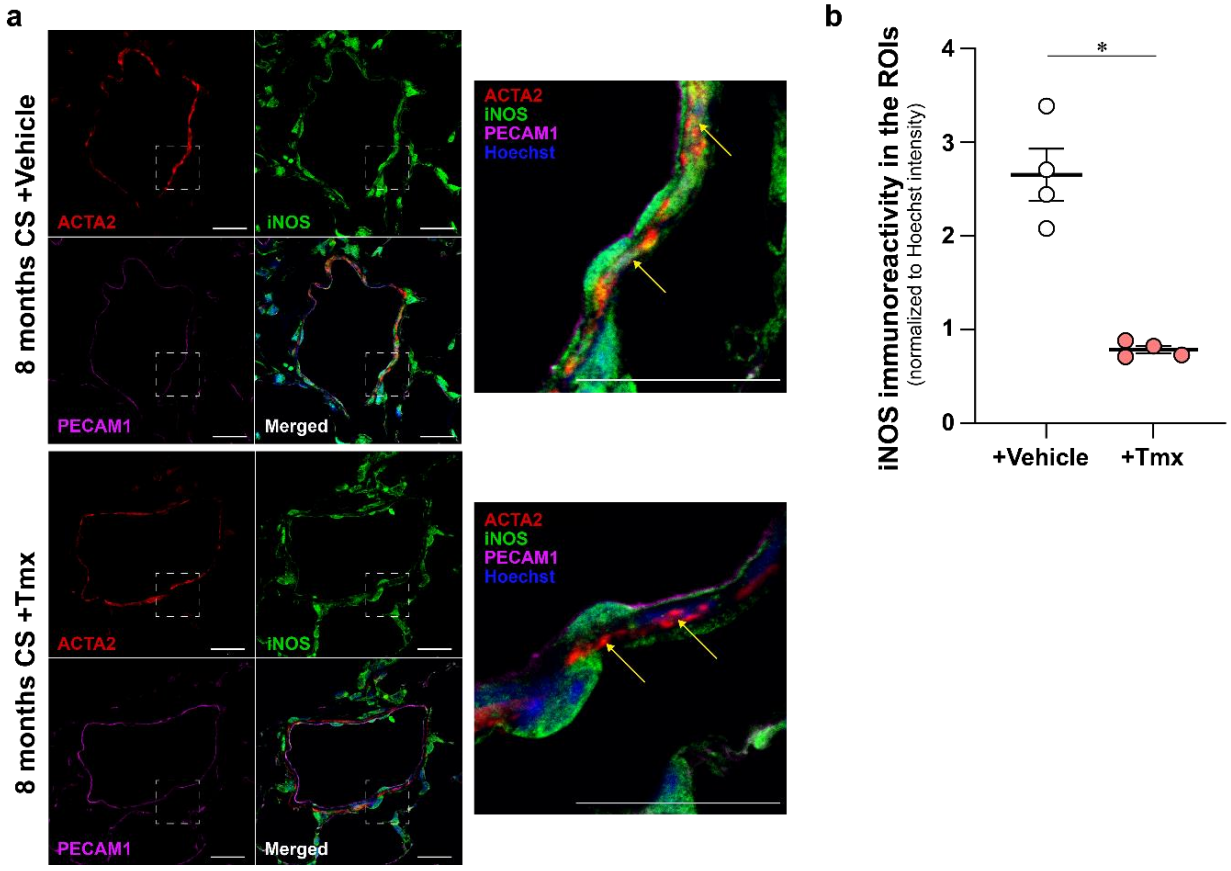

Figure 41. Efficiency of tamoxifen-induced *Acta2*$^{+}$ cell-specific *iNos*-ablation in transgenic mice. a, Representative images of immunofluorescence staining for ACTA2 (red), PECAM1 (magenta) and iNOS (green) in pulmonary vessels from CS-exposed transgenic mice administrated with vehicle (CS+Vehicle) or tamoxifen (CS+Tmx). Hoechst-33342 (blue) was

used to display nuclei. Yellow arrows indicate the areas immunoactive for ACTA2, where were defined as the regions of interest (ROIs) for quantification. Scale bars = 20 µm. **b,** Quantification of iNOS immunofluorescence intensity in the ROIs of mice administrated with vehicle (+Vehicle) or tamoxifen (+Tmx). The values of iNOS immunofluorescence intensity was normalized to the intensity of the Hoechst-33342 staining. Each dot represents an assessment in a mouse. The mean value of each group is represented by a horizontal line ± standard error of the mean (S.E.M.). Values from the mice administrated with vehicle (+Vehicle) are given as white dots, whereas those with tamoxifen (+Tmx) are shown as pink dots.
Statistical analysis: Two-tailed Student's t-test. An asterisk (*) denotes a p-value < 0.05, which is considered statistically significant between the two groups. Abbreviations: ACTA2, alpha-smooth muscle actin. PECAM1, Platelet endothelial cell adhesion molecule 1. iNOS, Inducible nitric oxide synthase. Tmx, Tamoxifen.

4. Discussion

The major findings in the current study are:

1. In hPASMCs, CSE exposure upregulated iNOS at both mRNA and protein level. A vast amount of iNOS-derived NO was produced upon CSE exposure.
2. Deletion of *iNos* protected mPASMCs and mAEC2s from CS-induced damage.
3. 3-NT, an indicator of nitrosative stress, was formed in pulmonary vessels and alveolar septa of smokers with end-stage COPD.
4. The CS-exposed transgenic mice developed PH after 3 and 8 months, independent of *iNos*-ablation in *Acta2*$^{+}$ cells.
5. *Acta2*$^{+}$ cell-specific *iNos*-knockout delayed alveolar destruction, but did not prevent CS-induced emphysema development.

4.1. Limitation of the techniques and animal models used in this study.

4.1.1 *In vitro* experiments.

In this study, the iNOS RNA/protein expression, NO levels and cell survival upon CSE exposure were investigated in a 2-dimentional (2D) monolayer cell culture system. Despite the advantages of the system, including focusing on one cell type at a time, standardized protocols, and well-established cell lines, one of the main limitation of such *in vitro* experiments is the lack of cell-cell interaction [127]. Over the past few years, large multitude of 3-dimentional (3D) cell culture techniques have been developed, such as an organoid/spheroid system, precision-cut lung slices (PCLS), and lung-on-a-chip [128-130]. To overcome the limitation of 2D cell culture system, one can employ 3D cell culture system to recapitulate the microenvironment and study the mechanisms in a more physiological manner [131].

Another remark is applications of cigarette smoke in the *in vitro* experiments. Although CSE was used throughout my study, it is possible to directly expose cells to the main stream CS (gas phase) using an air-liquid interface (ALI) system [132]. Moreover, to study non-epithelial cell behaviors upon CS, for instance, vascular/mesenchymal cells, one can introduce the lipid-soluble component in cigarette smoke (L-CSE) [133]. It is worth mentioning that, due the difficulty of long-term CS

exposure in the primary cell culture, the *in vitro* experiments can only partially reconstruct the scenarios of noxious gas exposure and study mechanisms underlying COPD development [12]. Therefore, animal experiments are indispensable to investigate the disease mechanisms and conduct pre-clinical studies of COPD [134].

4.1.2 Animal model of CS-induced COPD.

Chronic CS exposure was employed in my study to induce PH and emphysema in mice. As CS is the leading risk factor of COPD, it gives strength over other models to recapitulate the disease mechanisms in human [92]. Despite this model sharing most of the features observed in humans, such as vascular remodeling, augmented inflammation, and increased nitrosative/oxidative stress, it is not optimal for investigating mechanisms underlying human bronchitis due to the anatomical differences [85]. In addition, COPD progresses after cessation of CS in humans, but such an event is absent in the mouse model of CS-induced emphysema [85]. Therefore, to investigate the therapeutic potentials of CS-induced COPD, one should ensure that all the above-addressed points are considered.

4.1.3 Animal model of tamoxifen-induced gene ablation.

A cell-specific tamoxifen inducible Cre-*lox*P system was used in this study for deleting *iNos* in mice. Using transgenic mice, carrying a gene encoding tamoxifen inducible Cre-ER^{T2} fusion protein under mouse *Acta2* promoter, allows me to investigate the impact of iNOS-ablation in PASMCs on CS-induce PH and emphysema development. However, ACTA2 is not exclusively expressed in PASMCs. Studies using *Acta2*-$CreER^{T2}$ mouse line showed that ACTA2 is also expressed in myofibroblasts, airway smooth muscle cells (ASMCs) and alveolar fibroblasts [135, 136]. Nevertheless, compared with other common smooth muscle cell (SMC)-Cre mouse driver lines (e.g. *Myosin heavy chain 11 (Myh11)*-$CreER^{T2}$ or *Transgelin (Tagln)*-$CreER^{T2}$), *Acta2*-$CreER^{T2}$ was a more rigorous mouse line to achieve gene-deletion in PASMCs [137].

This study was conducted using the same strain of transgenic mice, which were administrated with either tamoxifen or vehicle control. The main concerns for such an experimental setup are the sole effect of tamoxifen and the off-target effect of activated Cre recombinase. Tamoxifen has been used as a treatment for breast cancer [138, 139]. As an anti-estrogen compound, tamoxifen *per se* influences cell signaling pathways, including activation of adenosine monophosphate activated

protein kinase (AMPK) pathway and inhibition of mitochondria complex I [140]. Although tamoxifen-induced gene deletion is very effective in the mouse lungs, a case report demonstrated that tamoxifen triggers a mild immune response leading to histopathological alterations in the distal lungs [141, 142]. Further study may include a tamoxifen-administrated wildtype mouse group to address the sole effect of tamoxifen treatment in the model of CS-induced PH and emphysema. Besides, to understand off-target effect of Cre recombinase in mice for this study, future research may include an additional control group using the transgenic mice without a floxed *iNos* gene, which are administrated with tamoxifen. Nevertheless, the current *in vivo* experimental design has a major advantage – the disease is induced in the littermate mice with the same genetic background. Most importantly, using these mice, the effect of the genetic background during crossbreeding can be excluded [143].

4.2. CSE exposure induces iNOS expression and iNOS-derived NO in PASMCs.

In this study, iNOS upregulation was confirmed at mRNA and protein level in CSE-exposed primary hPASMCs. Upon CSE exposure, a massive amount of NO production was observed in both hPASMCs and mPASMCs. As NO can be generated from not only iNOS, but also its isoforms, eNOS and nNOS [144-146], a pharmacological strategy was adopted to determine which enzyme is the source of NO in both CSE-exposed hPASMCs and mPASMCs. L-NIL, an iNOS-selective inhibitor, was reported to have the half maximal inhibitory concentration (IC_{50}) value of 3.3 µM in mouse iNOS and around 100 µM in rat eNOS [119]. To determine the optimal concentration for iNOS inhibition without hampering activity of other enzyme isoforms, 5 and 50 µM L-NIL were used to treat hPASMCs. Although CSE-exposed hPASMCs with 5 µM L-NIL pretreatment showed only a slight decrease in NO production, 5 µM L-NIL was potent enough to inhibit NO production in mPASMCs upon CSE exposure. Moreover, upon CSE exposure, the amount of NO in L-NIL-treated mPASMCs isolated from *Wt* mice was at the similar level as in mPASMCs isolated from *iNos*$^{-/-}$ mice without L-NIL pre-treatment. It further consolidated the hypothesis that iNOS is the NO source in PASMCs. Interestingly, CS-exposed hPASMCs with L-NIL pre-treatment and mPASMCs isolated from *Wt* and *iNos*$^{-/-}$ mice without L-NIL pre-treatment showed a significantly increased NO level relative to corresponding 0% CSE-exposed controls. Since the probe was added in the fresh media and applied to the cells after 6 hours of CSE exposure, exogenous NO from the CSE could be excluded. Thus, such increases in NO levels may derived

from other isoforms of NOS, such as nNOS or eNOS [147]. Nevertheless, from the results showing that *iNos*-deletion in CSE-exposed mPASMCs and mAEC2s showed higher survival than corresponding *Wt* groups, it may be concluded that iNOS and iNOS-derived NO, instead of eNOS and nNOS, were responsible in causing cell damage upon CSE exposure.

Since iNOS and iNOS-derived NO are involved in the 3-nitrotyrosine (3-NT) formation [148], 3-NT levels were investigated in the lungs explanted from healthy donors, smokers without COPD and smokers with COPD. In COPD, 3-NT is not only an indicator of nitrosative/oxidative stress, but also has been suggested to drive the disease development and linked to the disease's severity [65, 66]. In the current study, 3-NT was immunoreactive in pulmonary vessels and in alveolar septa of smokers with COPD, although a previous publication showed that iNOS in alveolar septa of CS-exposed mice was not regulated [44]. This may be explained by the biochemical properties of NO, superoxide and peroxynitrite. NO has a longer diffusion distance and is more stable than superoxide. Therefore, NO derived from iNOS in vascular cells (e.g. PASMCs) may diffuse to or near to the superoxide source in alveolar epithelial cells and react with superoxide to form a very short-living molecule, peroxynitrite. Peroxynitrite preferably attacks tyrosine residues of proteins, leading to 3-NT formation (protein nitration) [65, 148]. This notion is supported by a recent study, demonstrating that the superoxide release was inhibited in CSE-exposed *Noxo1*-knockout mAEC2s but not in mPASMCs, and 3-NT levels were reduced in the lungs of CS-exposed *Noxo1*-knockout mice as NOXO1-containing NADPH oxidases produces superoxide [47]. Similarly, deletion of iNOS in PASMCs may significant reduce nitrosative stress in the lungs and eventually prevent CS-induced emphysema development.

4.2 Transgenic mice are more susceptible to CS-induced damage.

Against this background, my study aimed to investigate the effect of *iNos*-deletion in PASMCs on CS-induced emphysema development. PASMCs are known to have abundant α-smooth muscle actin (*Acta2*) expression [149]. To delete the gene in PASMCs, a mouse model was designed using a tamoxifen-inducible *iNos*-knockout in *Acta2*-positive (*Acta*2^{+}) cells. The corresponding control to this variables was the same transgenic mouse line without tamoxifen administration (only vehicle). Both groups were exposed to RA or CS for 3 or 8 months, respectively. The transgenic mice showed no significant differences in body weight neither upon 3 and 8 months of CS exposure

nor tamoxifen administration. In a previous study, *Wt* mice (C57BL/6J) developed PH, evident from a significant increase in RVSP after 3 months of CS exposure [44]. Exposure of CS for 6 and 8 months caused emphysema development in mice, determined by increased mean linear intercept (MLI), airspace and decreased alveolar septal wall thickness [44]. Increased Fulton index, an indicator of right ventricular hypertrophy, was observed in *Wt* mice exposed to CS after 6 months [44]. The current findings in the transgenic mice demonstrated that PH was indeed developed after 3 months of CS exposure. However, right heart hypertrophy was seen in CS-exposed transgenic mice at this time-point. Moreover, according to the *in vivo* lung function measurements, the CS-exposed mice, independent of *iNos*-ablation in *Acta2*$^{+}$ cells, had emphysema already after 3 months of CS exposure. Hence, the transgenic mice used in this study were more susceptible to CS-induced damage. This could due to the strains and the genetic background of the transgenic mice, since these mice were bred across three different genotypes. Indeed, Guerassivmov *et al.* showed that CS-induced emphysema development depends on mouse strains [150]. Although the transgenic mice were more susceptible to CS exposure, the corresponding controls of this study ensured comparability within the study as all mice were of the same genetic background.

4.3 Deletion of *iNos* in *Acta2*$^{+}$ cells does not protect mice from CS-induced PH.

Non-invasive transthoracic echocardiography and right heart catheterization were used to determine whether the mice developed PH after 3 or 8 months of CS exposure. All measurements were performed during isoflurane anesthesia. It has been shown that the dose of anesthetics can influence the heart rate and therefore can affect echocardiography and RVSP measurements [151, 152]. However, in this study, there were no significant differences in the average heart rate among the experimental groups. The measured values were located in the range that is similar to a previous study used the same dose of isoflurane [153]. In addition, the average body weight among the groups showed no obvious differences. Therefore, when interpreting the data from non-invasive transthoracic echocardiography and right heart catheterization, the influence from these two factors can be excluded.

With the evidence of increased RVSP, declined TAPSE and a decreased PAT/PET ratio in the CS-exposed mice at both time-points (3 and 8 months), it can be concluded that *iNos*-ablation in *Acta2*$^{+}$ cells does not interfere with the CS-induced PH development. The results were in line with the

previous findings that iNOS in non-bone marrow-derived (NBMD) cells was not responsible for CS-induced PH in mice [44]. TAPSE is known to reflex the right ventricular function, whereas left ventricular function can be predicted by ejection fraction (EF) [154]. The cardiac function was therefore assessed by echocardiography. Both cardiac index (CI) and EF were decreased upon CS exposure. This is corresponding to the human situation when the cardiac function is affected in active cigarette smokers [155].

It is commonly known that right ventricular hypertrophy is a consequence of PH, due to the increased right ventricle afterload [19]. Indeed, this was confirmed by an increase in RV-free wall thickness (RVWT) and Fulton index as well as a profound decreased in right ventricular internal diameter (RVID) in CS-exposed mice. Even though transgenic mice developed right ventricular hypertrophy after 3 months of CS exposure, they did not develop right ventricular dilatation following 8 months of CS exposure. Right ventricular dilatation is one of the manifestations of right ventricular decompensation, which further leads to right heart failure [156, 157]. It usually occurs in more severe animal models of PH, such as the combined exposure to the vascular endothelial growth factor receptor antagonist – Sugen 5416 and chronic hypoxia or pulmonary artery banding (PAB) [158, 159]. In chronic CS exposed mice, merely a decreased diastolic function and EF was shown. However, heart failure has not been reported yet [160].

4.4 Lacking *iNos* in *Acta2*$^+$ cells delays, but does not completely prevent CS-induced emphysema.

In vivo lung function measurement confirmed that lungs in CS-exposed transgenic mice were more pliable than lungs in RA-exposed transgenic mice. This phenotype was independent from the ablation of *iNos* in *Acta2*$^+$ cells. Histological analyses consolidated the results from *in vivo* lung function measurement as increased percentage of airspace and decreased alveolar septal wall thickness were observed in transgenic mice exposed to CS for 3 and 8 months. However, when comparing images from alveolar morphometry between vehicle- and tamoxifen-administrated transgenic mice upon CS exposure for 3 months, alveolar septal wall in tamoxifen-administrated group was slightly thinner than in vehicle-administrated group. At the same duration of CS exposure, less emphysematous lesions were seen in *Acta2*$^+$ cell-specific *iNos*-knockout mice. This explains that MLI and number of alveoli (determined by stereological analysis) were preserved in

this group. Notably, such a phenotype was absent at the time-point of 8 months. These results indicated that *iNos*-ablation in *Acta2*$^+$ cells may partly confer a protection against CS-induced damage by reducing nitrosative stress in the lungs and delaying the process of emphysema development. It was shown that iNOS is expressed in many pulmonary cell types [161]. In the context of CS-exposed mice, iNOS was increased exclusively in pulmonary vessels, which comprise several cell types (e.g. smooth muscle cells (SMCs), endothelial cells (ECs) and fibroblasts (FBs)) [44, 162]. Knocking out *iNos* in *Acta2*$^+$ cells such as PASMCs can reduce iNOS-derived nitrosative stress. However, once CS exposure continued to a longer time-point, iNOS in other cell types (e.g. non-*Acta2*$^+$ vascular cells) could also contribute to 3-NT formation and cause emphysematous lesions. Eventually, *iNos*-deficiency in *Acta2*$^+$ cells solely slowed down the process of CS-induced alveolar destruction, but did not prevent establishment of emphysema.

Along this line, the lung is a regenerative organ similar to the liver and pancreas [163]. The regeneration relies on the stem/progenitor cells, receiving autocrine/paracrine instructive signals, primarily from growth factor secretion by mesenchymal stromal cells (MSCs). In addition, developmental signaling pathways, such as sonic hedgehog (Shh), Wnt/ß-catenin, Notch and Hippo signaling can also initiate the lung regeneration process [163-167]. It has been reported that several *Acta2*$^+$ pulmonary cell types, such as ASMCs, PASMCs and alveolar myofibroblasts, may reside in the lungs as MSCs [149]. Not only are they indispensable during the lung development, but also important for reparative process in the adult lungs [149, 168, 169]. The delayed development of emphysema in *Acta2*$^+$ cell-specific *iNos*-knockout mice upon CS exposure is possibly owing to the increased lung regenerative capacity in *iNos*-knockout SMCs or *Acta2*$^+$ cells.

Although *iNos*-knockout in *Acta2*$^+$ cells may boost the lung reparative activities, iNOS in non-*Acta2*$^+$ vascular cells could lead to 3-NT formation in growth factors [170]. Such a post-translational modification in growth factors derived from MSCs or in the proteins related to developmental pathways may hamper the regeneration process during the extensive CS-induced injury [171]. Eventually, the lung regeneration was overwhelmed by lung destruction. Thus, *Acta2*$^+$ cell-specific *iNos*-knockout mice developed CS-induced emphysema when the duration of CS exposure was prolonged. Recent studies, using lineage-traced and single-cell transcriptomic profiling, revealed many distinct mesenchymal niches that contribute to epithelial self-renewal [172, 173]. Some of these mesenchymal niches are *Acta2*$^+$ cells, such as ASMCs or myofibroblasts

[169, 174]. Therefore, further investigations are needed to decipher whether after the CS-induced injury, *iNos*-knockout in *Acta2*$^{+}$ cells could reverse the established pulmonary emphysema. If it does, a single-cell sequencing-based transcriptomic analysis would pinpoint the cell population and the underlying mechanisms in restoration of the lung.

5. Conclusion

Inducible nitric oxide synthase (iNOS) expression *in vitro*, in pulmonary artery smooth muscle cells (PASMCs) was increased upon cigarette smoke extract (CSE) exposure. The upregulation of iNOS led to an increased production of nitric oxide (NO). Consequently, nitrosative stress was augmented, which could be responsible for decreased cell survival upon CSE exposure via 3-nitrotyrosine formation and thus COPD development.

Along this line, I performed an animal study using transgenic mice to delete *iNos* in PASMCs in order to investigate its impact during cigarette smoke (CS)-induced pulmonary hypertension (PH) and emphysema development. All animals in the study carried *iNos*$^{flox/flox}$ and the gene encoded inducible Cre recombinase (Cre/ER^{T2}), expressed under the *Acta2* gene promoter (*Acta2*-Cre/ER^{T2}). Ablation of the *iNos* gene in *Acta2*-positive (*Acta2*$^{+}$) cells was induced upon tamoxifen administration. PH was observed in transgenic mice after 3 and 8 months of CS exposure, evident from increased right ventricular systolic pressure (RVSP), deceased tricuspid annular plane systolic excursion (TAPSE) and declined ratio of pulmonary artery acceleration time and pulmonary artery ejection time (PAT/PET). This phenotype appeared independent of *iNos*-deletion in *Acta2*$^{+}$ cells. In addition, these mice had an increased right ventricular wall thickness (RVWT), a decreased right ventricular internal diameter (RVID), and an increased Fulton index, indicating the development of right heart hypertrophy.

Moreover, left-shifted pressure-volume (PV) loops upon assessment of lung function and elevated lung static compliance occurred not only in mice upon 8 months of CS exposure, but also in those after 3 months of CS exposure. These results indicated that CS-exposed transgenic mice develop emphysema. The early development of right heart hypertrophy and aberrant lung function in CS-exposed mice, in comparison to a previous study in wildtype mice, could be associated with the background of the transgenic mice. This effect could, however, be controlled by appropriate control groups (littermate mice with the same genetic background) in my study.

Interestingly, histological and design-based stereological analyses revealed a reduction in alveolar septal wall thickness and an enlargement in alveolar airspace of CS-exposed mouse lungs. However, the number of alveoli and the structure of the septal wall (evaluate by mean linear intercept (MLI)) were preserved in *Acta2*$^{+}$ cell-specific *iNos*-knockout mice after 3 months of CS

exposure. Such differences were not detectable in CS-exposed *Acta2*$^{+}$ cell-specific *iNos*-knockout mice following CS exposure for 8 months. Such data indicated a delayed development of emphysema in CS-exposed *Acta2*$^{+}$ cell-specific *iNos*-knockout mice. Lacking *iNos* in *Acta2*$^{+}$ cells could possibly decrease the nitrosative stress in the CS-exposed mouse lung. As many mesenchymal stromal cells (MSCs) are *Acta2*-lineage cells, participating in lung regeneration by, for example, secreting growth factors [175], *Acta2*$^{+}$ cell-specific *iNos*-ablation may reduce the 3-NT formation in the secreted growth factors. Hence, *Acta2*$^{+}$ cell-specific *iNos*-knockout mice may have a higher lung regenerative capacity. However, the contributions of nitrosative stress from other non-bone marrow-derived (NBMD) vascular cell types, such as endothelial cell, may also jeopardize the lung repair process. Therefore, the *Acta2*$^{+}$ cell-specific *iNos*-knockout mice may still develop emphysema after 8 months of CS exposure.

Taken together, the current study provided evidence that iNOS is expressed and can be induced by CSE in PASMCs. *Acta2*$^{+}$ cell-specific *iNos*-ablation does not protect mice from CS-induced PH and emphysema development, but delays the process of alveolar destruction **(Figure 42)**. Further studies may be conducted by targeting other vascular cell types (e.g. endothelial cell-specific *iNos*-knockout) to pinpoint the cell type(s) responsible for the prevention against CS-induced emphysema. Also, future research directions can focus on deciphering whether the mechanisms underlying the lung regeneration is iNOS-dependent by employing a therapeutic approach (e.g. to knockout *iNos* in *Acta2*$^{+}$ cell after the full-established CS-induced emphysema).

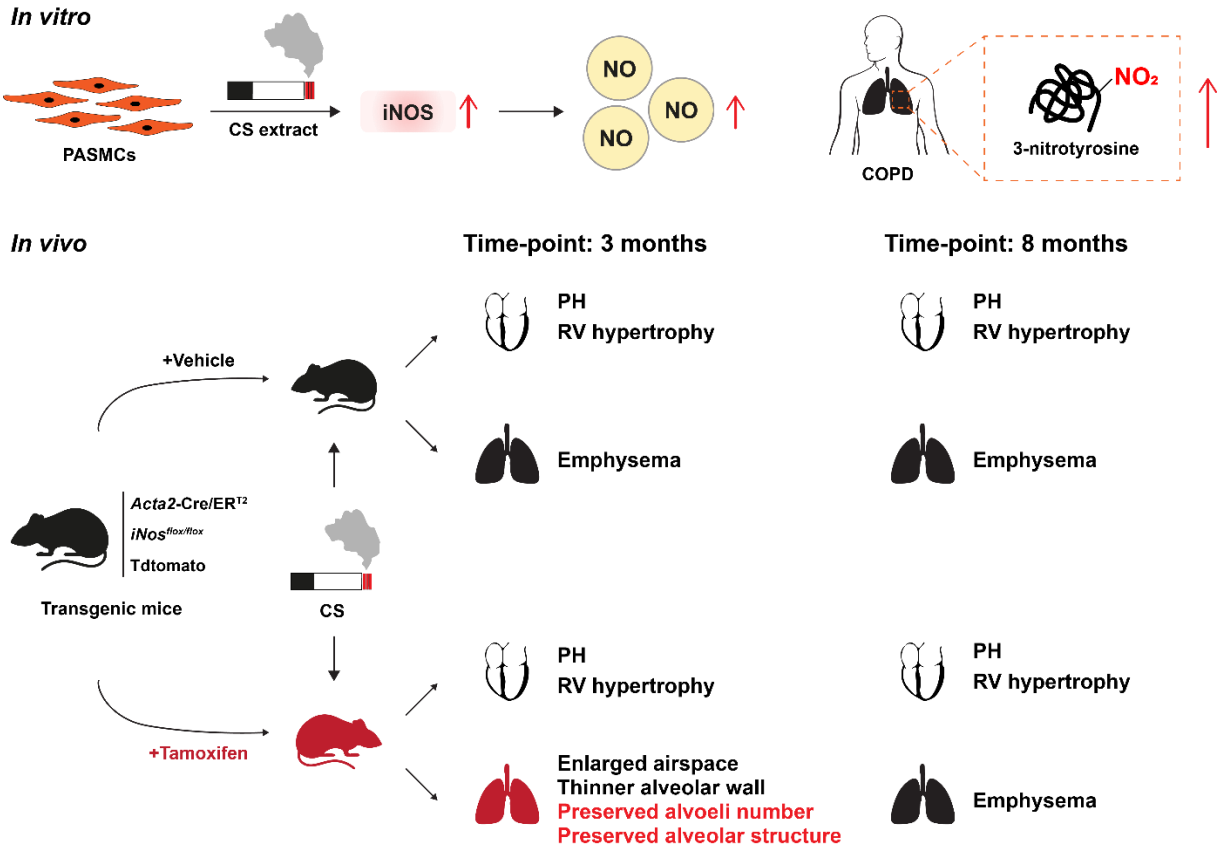

Figure 42. Schematic illustration of the conclusion of the study.
In vitro results showed that nitrosative stress (iNOS, NO) was increased in pulmonary artery smooth muscle cells (PASMCs) upon cigarette smoke (CS) extract exposure. These findings were in line with increased 3-nitrotyroine levels in the patients with COPD. Targeting *iNos*-ablation in *Acta2*$^{+}$ cells led to the development of pulmonary hypertension (PH) and right ventricular hypertrophy, but a delayed emphysema development in CS-exposed mice.
Abbreviation: PASMCs, Pulmonary artery smooth muscle cells. CS, Cigarette smoke. iNOS, Inducible nitric oxide synthase. NO, Nitric oxide. COPD, Chronic obstructive pulmonary disease. PH, Pulmonary hypertension. RV hypertrophy, Right ventricular hypertrophy.

6. Summary

Chronic obstructive pulmonary disease (COPD) is a significant health problem and, in addition to the burden for the patients, has a large socio-economic impact. Apart from airway diseases and pulmonary emphysema, COPD patients often suffer from a least mild pulmonary hypertension (PH). The major etiological factor is the inhalation of noxious gases or particulate matters, primarily from cigarette smoking and air pollution. Cigarette smoke (CS) drives COPD development through multiple cellular and molecular mechanisms, encompassing augmented immune responses, unbalanced proteases/anti-proteases, aberrant cell death/senescence and excessive nitrosative/oxidative stress.

Previously, the inducible nitric oxide synthase (iNOS) was identified, from a mouse model of chronic exposure to CS, as a key enzyme responsible for pulmonary hypertension (PH) and emphysema development by causing nitrosative stress. In this animal model, CS-exposed mice showed alterations in the pulmonary vasculature way before signs of emphysema development. Such results indicate a possible interaction between the pulmonary vasculature and the alveolar compartment during CS-induced PH and emphysema development. Moreover, *iNos*-deletion in non-bone marrow-derived cells prevented CS-induced emphysema in mice, whereas PH was absent in CS-exposed mice lacking *iNos* in bone marrow-derived cells. A significant iNOS upregulation was observed in pulmonary vessels of CS-exposed mice and human COPD lungs. However, the contribution of increased iNOS expression/nitrosative stress in lung vessels to CS-induced emphysema and PH development remains unresolved.

Against this background, the current study aimed to investigate the role of iNOS in pulmonary artery smooth muscle cells (PASMCs) during CS-induced PH and emphysema development. *In vitro* results revealed that iNOS was expressed in human PASMCs and increased upon cigarette smoke extract (CSE) exposure. Increased NO production was a consequence of iNOS upregulation, validated by employing a selective iNOS inhibitor – L-NIL, as well as by using PASMCs isolated from *iNos*-knockout ($iNos^{-/-}$) mice. Furthermore, PASMCs and alveolar type 2 epithelial cells (AEC2s) isolated from $iNos^{-/-}$ mice were partially protected from CSE-induced damage. This may be associated with the reduction in NO levels. NO is one of the main contributors to nitrosative stress. Together with superoxide, it can form peroxynitrite, causing

protein nitration at tyrosine residues, known as 3-nitrotyrosine (3-NT). 3-NT is not only a marker of nitrosative/oxidative stress, but can also alter cell signaling and thus can propagate disease progression. Along this line, an increased 3-NT formation was observed in the lung from patients with COPD, predominantly in pulmonary vessels and alveolar septa.

To investigate the effect of iNOS in PASMCs on the development of CS-induced PH and emphysema, transgenic animals in which *iNos* was deleted in *Acta2*-positive (*Acta2*$^+$) cells were employed and exposed to CS for 3 or 8 months. Neither CS, nor *iNos* deletion in *Acta2*$^+$ cells, affected body weight and heart rate. However, CS led to an increased right ventricular systolic pressure (RVSP), a decreased ratio of pulmonary artery acceleration time and pulmonary artery ejection time (PAT/PET) and a decreased tricuspid annular plane systolic excursion (TAPSE), indicating the development of PH. This was independent of *iNos*-ablation in *Acta2*$^+$ cells. Interestingly, right heart hypertrophy was already present in CS-exposed transgenic mice at time-point of 3 months, determined by an increased right ventricular wall thickness (RVWT), a decreased right ventricular internal diameter (RVID), and an elevated Fulton index. This is in contradiction to previous studies, in which *Wt* mice (C57BL/6J) showed an increased Fulton index after a longer period of CS exposure only. Possibly, this may be due to a higher strain-dependent susceptibility to CS-induced damage.

Indeed, *in vivo* lung function parameters indicated that emphysema was developed after 3 and 8 months of CS exposure, regardless of the loss of *iNos* in *Acta2*$^+$ cells. However, histological and designed-based stereological analyses suggested that the deletion of *iNos* in *Acta2*$^+$ cells preserved the alveoli number and the alveolar structure in mice after 3 months of CS exposure. Such findings were absent in *Acta2*$^+$ cell-specific *iNos*-knockout mice after 8 months of CS exposure, pointing out that *Acta2*$^+$ cell-specific *iNos*-ablation delayed, but did not completely prevent CS-induced emphysema. This may be due to the nitrosative stress conferred by other iNOS-containing cell types, such as endothelial cells or an increased regenerative capacity when *iNos* was deleted in PASMCs.

In conclusion, iNOS expression in PASMCs caused a large amount of NO production upon CS-exposure, which can be a main contributor for nitrosative stress and 3-NT formation in the lungs. In line with a previous study, when mice with deletion of *iNos* in non-bone marrow-derived cells were investigated, the loss of *iNos* in *Acta2*$^+$ cells did not interfere with CS-induced PH

development. A delayed emphysema development was observed in transgenic mice when *iNos* was deleted in *Acta2*$^{+}$ cells after 3 months of CS exposure. It would be intriguing for further investigation to focus on the role of other iNOS-containing vascular cell types in CS-induced emphysema prevention, or on the effect of iNOS-ablation in PASMCs on lung regeneration.

7. Zusammenfassung

Die chronisch obstruktive Lungenerkrankung (COPD) ist ein bedeutendes Gesundheitsproblem und stellt darüber hinaus eine enorme sozioökonomische Belastung dar. Neben Atemwegserkrankungen und Lungenemphysem leiden COPD-Patienten häufig an einer zumindest leichten pulmonalen Hypertonie (PH). Der wichtigste ätiologische Faktor ist das Einatmen von schädlichen Gasen oder Partikeln, vor allem durch Zigarettenrauch und Luftverschmutzung. Zigarettenrauch (CS) fördert die Entwicklung von COPD durch mehrere zelluläre und molekulare Mechanismen, darunter verstärkte Immunreaktionen, ein Ungleichgewicht von Proteasen/Antiproteasen, abnormalem Zelltod/Seneszenz und übermäßigem nitrosativem/oxidativem Stress.

In vorangehenden Untersuchungen wurde die induzierbare Stickstoffmonoxid-Synthase (iNOS) in einem Mausmodell mit chronischer CS-Exposition als ein Schlüsselenzym identifiziert, das für die Entwicklung der Pulmonale Hypertonie (PH) und des Emphysems verantwortlich ist, indem es übermäßigen nitrosativen Stress verursacht. In diesem Tiermodell zeigten CS-exponierte Mäuse Veränderungen im Lungengefäßsystem lange vor den Anzeichen der Emphysementwicklung. Diese Ergebnisse deuten auf eine mögliche Interaktion zwischen dem Lungengefäßsystem und dem alveolären Kompartiment während der CS-induzierten PH und der Emphysementwicklung hin. Darüber hinaus verhinderte die Deletion von *iNos* in Zellen, die nicht aus dem Knochenmark stammen, das CS-induzierte Emphysem bei Mäusen, während die PH bei CS-exponierten Mäusen, denen *iNos* in Zellen aus dem Knochenmark fehlte, ausblieb. In den Lungengefäßen von CS-exponierten Mäusen und menschlichen COPD-Lungen wurde eine signifikante iNOS-Hochregulierung beobachtet. Die physiologische Relevanz der erhöhten iNOS-Expression und des gesteigerten nitrosativen Stresses in den Lungengefäßen bei der Entwicklung des CS-induzierten Emphysems und der PH ist jedoch noch ungeklärt.

Vor diesem Hintergrund habe ich die Rolle von iNOS in glatten Muskelzellen der Lungenarterie (PASMCs) während der CS-induzierten PH und Emphysementwicklung untersucht. In dieser Studie konnte ich nachweisen, dass iNOS in menschlichen PASMCs exprimiert wird und durch die *in-vitro*-Exposition mit Zigarettenrauchextrakt (CSE) induziert wird. Dann bestätigte ich, dass der massive Anstieg der NO-Produktion eine Folge der iNOS-Hochregulierung war, indem ich

einen selektiven iNOS-Inhibitor – L-NIL – sowie PASMCs, die aus *iNos*-knockout (*iNos*$^{-/-}$)-Mäusen isoliert wurden, verwendet habe. Darüber hinaus waren PASMCs und alveoläre Typ-2-Epithelzellen (AEC2s), die aus *iNos*$^{-/-}$-Mäusen isoliert wurden, teilweise vor CSE-induzierten Schäden geschützt. Dies könnte mit der Verringerung des NO-Spiegels zusammenhängen. NO ist einer der Hauptverursacher von nitrosativem Stress. Zusammen mit Superoxid bildet es Peroxynitrit, das die Nitrierung von Proteinen an Tyrosinresten, als 3-Nitrotyrosin (3-NT)-Bildung bekannt, verursacht. 3-NT ist nicht nur ein Marker für nitrosativen/oxidativen Stress, sondern kann auch die Zellsignalübertragung verändern und damit das Fortschreiten der Erkrankung fördern. In diesem Sinne habe ich in der Lunge von COPD-Patienten eine erhöhte 3-NT-Bildung, vor allem in den Lungengefäßen und den Alveolarsepten, beobachtet.

Um die Wirkung von iNOS in PASMCs auf die Entwicklung von CS-induzierter PH und Emphysem zu untersuchen, habe ich transgene Tiere, bei denen *iNos* in *Acta2*-positiven (*Acta2*$^{+}$) Zellen deletiert wurde, verwendet. Die Tiere wurden dann 3 oder 8 Monate lang CS ausgesetzt. Weder CS, noch die Deletion von *iNos* in *Acta2*$^{+}$-Zellen, zeigte einen Einfluss auf das Körpergewicht und die Herzfrequenz. Allerdings führte CS zu einem erhöhten rechtsventrikulären systolischen Druck, einem verringerten Verhältnis zwischen der Beschleunigungszeit der Lungenarterie und der Auswurfzeit der Lungenarterie (PAT/PET) und einer verringerten systolischen Auslenkung der Trikuspidalebene (TAPSE), was auf die Entwicklung einer PH hinweist. Dies war unabhängig von der *iNos*-Ablation in *Acta2*$^{+}$-Zellen. Interessanterweise wurde bei CS-exponierten transgenen Mäusen nach drei Monaten eine Rechtsherzhypertrophie beobachtet, die durch eine erhöhte rechtsventrikuläre Wanddicke (RVWT), einen verringerten rechtsventrikulären Innendurchmesser (RVID) und einen erhöhten Fulton-Index bestimmt wurde. Ein erhöhter Fulton-Index wurde im vorangehenden Studien in z.B. Wildtyp-Mäusen erst nach längerer CS-exposition festgestellt. Dieses könnte eventuell mit dem genetischen Hintergrund der verwendeten Mäuse in Zusammenhang stehen; möglicherweise sind diese anfälliger für CS-induzierte Schäden.

In der Tat deuteten die *in vivo* Lungenfunktionsparameter bei allen CS-exponierten Mäusen nicht nur zum 8-Monats-Zeitpunkt, sondern auch schon zum 3-Monats-Zeitpunkt auf ein Emphysem hin, unabhängig vom Verlust von *iNos* in *Acta2*$^{+}$-Zellen. Insbesondere zeigten stereologische und histologische Analysen, dass durch die Deletion von *iNos* in *Acta2*$^{+}$-Zellen die Anzahl der

Alveolen und die alveoläre Struktur bei Mäusen nach 3 Monaten CS-Exposition erhalten blieb. Diese Phänomene waren bei 8-monatiger CS-Exposition von *Acta2*$^{+}$-Zellen-spezifischen *iNos*-Knockout-Mäusen nicht vorhanden. Die Ergebnisse legen nahe, dass die *Acta2*$^{+}$-Zell-spezifische iNos-Ablation das CS-induzierte Emphysem zwar verzögert, aber nicht vollständig verhindert. Dies könnte auf den nitrosativen Stress zurückzuführen sein, der von anderen iNOS-haltigen Zelltypen, wie z. B. Endothelzellen, ausgeht, oder auf eine erhöhte Regenerationsfähigkeit, wenn iNOS in PASMCs nicht vorhanden ist.

Zusammenfassend lässt sich sagen, dass die iNOS-Expression in CSE-exponierten PASMCs zu einer erhöhten NO-Produktion führt, welche ein Hauptfaktor für nitrosativen Stress und die Bildung von 3-NT in der Lunge sein kann. In Übereinstimmung mit der vorangegangenen Studie hatte der Verlust von *iNos* in *Acta2*$^{+}$-Zellen keinen Einfluss auf die CS-induzierte PH-Entwicklung. Bei Mäusen, die 3 Monate lang CS ausgesetzt waren und bei denen *iNos* in *Acta2*$^{+}$-Zellen entfernt wurde, wurde eine verzögerte Emphysementwicklung beobachtet. Weitergehende Studien wäre ist interessant die Rolle anderer iNOS-exprimierender vaskulärer Zellen für die Prävention des CS-induzierten Emphysems und/oder die Auswirkungen der iNOS-Ablation in PASMCs auf die Lungenregeneration zu untersuchen.

8. Index of Figures

9. Index of Tables

10. Declaration

I declare that I have completed this thesis on my own, without unauthorized outside help and only with the assistance acknowledged therein. I have properly acknowledged and referenced all the passages which are derived literally or analogously from published or unpublished work and all information that relates to verbal communications. I have the principles of good scientific practice such as these in the “Statute of Justus Liebig University Giessen to ensure good scientific practice” in my work and in my thesis.

_____

Cheng-Yu Wu

11. Acknowledgements

My doctoral dissertation "**The effect of inducible nitric oxide synthase-ablation in pulmonary artery smooth muscle cells on CS-induced pulmonary hypertension and emphysema development**" was done in the laboratory for Molecular Mechanisms of Emphysema, Hypoxia and Lung ageing (Professor Dr. Norbert Weißmann) at the Excellence Cluster Cardio Pulmonary Institute (CPI), Department of Internal Medicine, Justus Liebig University Giessen.

Undertaking the work for this thesis at Justus Liebig University Giessen has not only been challenging, but also a life-changing experience for me. It would have not been possible to achieve without the guidance and support that I received from many people.

First and foremost, I am indebted with the deepest gratitude to Professor Dr. Norbert Weißmann, for his invaluable advice, prompt inspiration, insightful suggestions, timely encouragement and selfless assistance during my PhD study. His passion for science, extensive research knowledge, and trust in me have nurtured me from a sapling to a tree.

I would like to thank my co-supervisor – Professor Dr. Martin Diener. Without his guidance, I would have gotten lost as if a boat without a lighthouse in an academic ocean.

Special acknowledgements to Professor Dr. Werner Seeger, Department of Internal Medicine, Director of the Medical Clinic II, Chairmen of the German Centre for Lung Research (DZL), Director of the Department IV, Max Planck Institute for Heart and Lung Research, Bad Nauheim. His vision, commitment and pursue of providing the perfect scientific working environment gave me the opportunity to develop my academic career in the best conditions.

My warmest thanks to Dr. Simone Kraut for recruiting me for this research group. Thanks to her kindness, support and professional skills, the journey of obtaining my doctoral title has become less bumpy.

I would like to acknowledge the International Giessen Graduate Centre for the Life Sciences (GGL) and Molecular Biology and Medicine of the Lung (MBML) PhD program for shaping me into a proper researcher in the lung field.

I would like to express my immense gratitude to Dr. Christine Veith-Berger, Dr. Jochen Wilhelm, Dr. Mariola Bednorz, Dr. Monika Brosien, Prof. Dr. Andreas Günther, Prof. Dr. Natascha Sommer, Prof. Dr. Friedrich Grimminger, Prof. Dr. Hossein A. Ghofrani, Prof. Dr. Ralph T. Schermuly, Dr. Ingrid Henneke, Dr. Thomas Sontag, Siddartha Doswada and Marouane Qsaib for the precious exchange of opinions and practical assistance.

I also would like to thank: Daniela Weber, Elizabeta Krstić, Karin Quanz, Nils Schupp, Carmen Homberger, Dileep Bonthu, Ingrid Breitenborn-Müller, Miriam Wessendorf, Christina Pilz for their assistance in administrative, technical or personal issues.

I offer my sincere appreciation to Marija Gredić, PhD, Dr. Oleg Pak and Dr. Stefan Hadžić for their selfless assistance, priceless advice, brilliant ideas, extraordinary suggestions and most importantly, their companionship on the path to my PhD degree.

I whole-heartedly thank Dr. Đuro Kosanović, Dr. Claudio Nardiello, Claudia Fernanda Garcia Castro, Aleksandar Petrović, Zeki Ilker Kanbagli, Julia Schäffer, Dr. Kathrin Malkmus, Dr. Katharina Schäfer, Dr. Ipek Vartürk-Özcan, Dr. Mira Y. Gökyildirim and Dr. Magdalena Wujak who have been with me over the years in the laboratory; therefore, I never felt lonely on this journey.

I am very grateful to my friends from Taiwan, the Handsomeline group, especially the members who visited me during my study: 高仲均、楊森喜、謝亞辰、詹士徵.

Last but not the least, I owe my utmost gratitude to my family who is always there unconditionally supporting me, who believe in me and who have subordinated their lives to my success. 在此特別感謝我的父母，吳水金、王金妹，以及我的姊姊，吳妮晏，沒有他們的支持與鼓勵，我永遠沒有機會拿到博士學位。我也要感謝阿公、阿嬤時時刻刻掛念我，讓我有動力持續向前衝。感謝我的叔叔與阿嬸，吳振揚、陳癸伶，我的舅舅與舅媽，王條明、鄧麗華，有了他們的關愛與照顧，才使我今天能夠完成我的學術論文。最後我要感謝神明們保佑我一路順遂直到今日。

12. Literature

1. Weibel, E.R., *The pathway for oxygen : structure and function in the mammalian respiratory system*. 1984, Cambridge, Mass.: Harvard University Press.
2. Jurgens, K.D. and G. Gros, *[Phylogeny of gas exchange systems]*. Anasthesiol Intensivmed Notfallmed Schmerzther, 2002. **37**(4): p. 185-98.
3. Whittemore, S. and D.A. Cooley, *The Respiratory System*. 2009: Chelsea House.
4. Mitchell, P. and J. Moyle, *Chemiosmotic hypothesis of oxidative phosphorylation.* Nature, 1967. **213**(5072): p. 137-9.
5. Zepp, J.A. and E.E. Morrisey, *Cellular crosstalk in the development and regeneration of the respiratory system.* Nat Rev Mol Cell Biol, 2019. **20**(9): p. 551-566.
6. Cardoso, W.V. and D.N. Kotton, *Specification and patterning of the respiratory system*, in *StemBook*. 2008: Cambridge (MA).
7. Marieb, E.N., *Human anatomy & physiology*. 2004, San Francisco, Calif.: Pearson Benjamin Cummings.
8. Ochs, M., et al., *The number of alveoli in the human lung.* Am J Respir Crit Care Med, 2004. **169**(1): p. 120-4.
9. West, J.B. and A. Luks, *West's respiratory physiology : the essentials*. 2016.
10. Carel, R.S. *Chapter 3 Health Aspects of Air Pollution*. 1998.
11. Mader, S.S.W.M., *Human biology*. 2018.
12. Hadzic, S., et al., *Lung epithelium damage in COPD - An unstoppable pathological event?* Cell Signal, 2020. **68**: p. 109540.
13. Robertson, H.T., *Dead space: the physiology of wasted ventilation.* Eur Respir J, 2015. **45**(6): p. 1704-16.
14. Wanger, J., et al., *Standardisation of the measurement of lung volumes.* Eur Respir J, 2005. **26**(3): p. 511-22.
15. Lutfi, M.F., *The physiological basis and clinical significance of lung volume measurements.* Multidiscip Respir Med, 2017. **12**: p. 3.
16. Mead, J., et al., *Significance of the relationship between lung recoil and maximum expiratory flow.* J Appl Physiol, 1967. **22**(1): p. 95-108.
17. David, S. and C.W. Edwards, *Forced Expiratory Volume*, in *StatPearls*. 2021: Treasure Island (FL).
18. Barnes, P.J., et al., *Chronic obstructive pulmonary disease.* Nat Rev Dis Primers, 2015. **1**: p. 15076.
19. Gredic, M., et al., *Pulmonary hypertension in chronic obstructive pulmonary disease.* Br J Pharmacol, 2020.
20. Vogelmeier, C.F., et al., *Global Strategy for the Diagnosis, Management, and Prevention of Chronic Obstructive Lung Disease 2017 Report. GOLD Executive Summary.* Am J Respir Crit Care Med, 2017. **195**(5): p. 557-582.
21. White, A.J., S. Gompertz, and R.A. Stockley, *Chronic obstructive pulmonary disease . 6: The aetiology of exacerbations of chronic obstructive pulmonary disease.* Thorax, 2003. **58**(1): p. 73-80.
22. Woodhead, M., et al., *Guidelines for the management of adult lower respiratory tract infections.* Eur Respir J, 2005. **26**(6): p. 1138-80.
23. Anzueto, A., *Impact of exacerbations on COPD.* Eur Respir Rev, 2010. **19**(116): p. 113-8.

24. Cavailles, A., et al., *Comorbidities of COPD.* Eur Respir Rev, 2013. **22**(130): p. 454-75.
25. Soriano, J.B., et al., *Global, regional, and national deaths, prevalence, disability-adjusted life years, and years lived with disability for chronic obstructive pulmonary disease and asthma, 1990–2015: a systematic analysis for the Global Burden of Disease Study 2015.* Lancet Respir Med, 2017. **5**(9): p. 691-706.
26. Greulich, T., et al., *The prevalence of diagnosed alpha1-antitrypsin deficiency and its comorbidities: results from a large population-based database.* Eur Respir J, 2017. **49**(1).
27. Garudadri, S. and P.G. Woodruff, *Targeting Chronic Obstructive Pulmonary Disease Phenotypes, Endotypes, and Biomarkers.* Ann Am Thorac Soc, 2018. **15**(Suppl 4): p. S234-S238.
28. Corlateanu, A., et al., *"Chronic obstructive pulmonary disease and phenotypes: a state-of-the-art."*. Pulmonology, 2020. **26**(2): p. 95-100.
29. Brightling, C. and N. Greening, *Airway inflammation in COPD: progress to precision medicine.* Eur Respir J, 2019. **54**(2).
30. *Definition and classification of chronic bronchitis for clinical and epidemiological purposes. A report to the Medical Research Council by their Committee on the Aetiology of Chronic Bronchitis.* Lancet, 1965. **1**(7389): p. 775-9.
31. Saetta, M., et al., *Goblet cell hyperplasia and epithelial inflammation in peripheral airways of smokers with both symptoms of chronic bronchitis and chronic airflow limitation.* Am J Respir Crit Care Med, 2000. **161**(3 Pt 1): p. 1016-21.
32. Kumar, Vinay, Abul K. Abbas, and Jon C. Aster. *Robbins basic pathology* e-book. Elsevier Health Sciences, 2017.
33. Higham, A., et al., *The pathology of small airways disease in COPD: historical aspects and future directions.* Respir Res, 2019. **20**(1): p. 49.
34. Snider, G.L., et al., *The definition of emphysema: report of a National Heart, Lung, and Blood Institute, Division of Lung Diseases workshop*. 1985, American Lung Association.
35. Black, P.N., et al., *Changes in elastic fibres in the small airways and alveoli in COPD.* Eur Respir J, 2008. **31**(5): p. 998-1004.
36. Kim, W.D., et al., *Centrilobular and panlobular emphysema in smokers. Two distinct morphologic and functional entities.* Am Rev Respir Dis, 1991. **144**(6): p. 1385-90.
37. Smith, B.M., et al., *Pulmonary emphysema subtypes on computed tomography: the MESA COPD study.* Am J Med, 2014. **127**(1): p. 94.e7-23.
38. Im, J.G., H. Itoh, and M.C. Han, *CT of pulmonary tuberculosis.* Semin Ultrasound CT MR, 1995. **16**(5): p. 420-34.
39. Simonneau, G., et al., *Haemodynamic definitions and updated clinical classification of pulmonary hypertension.* Eur Respir J, 2019. **53**(1): p. 1801913.
40. Hoeper, M.M. and M. Humbert, *The new haemodynamic definition of pulmonary hypertension: evidence prevails, finally!* Eur Respir J, 2019. **53**(3): p. 1900038.
41. Hoeper, M.M., et al., *Definitions and diagnosis of pulmonary hypertension.* J Am Coll Cardiol, 2013. **62**(25 Suppl): p. D42-50.
42. Santos, S., et al., *Characterization of pulmonary vascular remodelling in smokers and patients with mild COPD.* Eur Respir J, 2002. **19**(4): p. 632-638.
43. Weissmann, N., et al., *Stimulation of soluble guanylate cyclase prevents cigarette smoke-induced pulmonary hypertension and emphysema.* Am J Respir Crit Care Med, 2014. **189**(11): p. 1359-73.

44. Seimetz, M., et al., *Inducible NOS inhibition reverses tobacco-smoke-induced emphysema and pulmonary hypertension in mice.* Cell, 2011. **147**(2): p. 293-305.
45. Ferrer, E., et al., *Effects of cigarette smoke on endothelial function of pulmonary arteries in the guinea pig.* Respir Res, 2009. **10**(1): p. 76.
46. Wright, J.L. and A. Churg, *Effect of long-term cigarette smoke exposure on pulmonary vascular structure and function in the guinea pig.* Exp Lung Res, 1991. **17**(6): p. 997-1009.
47. Seimetz, M., et al., *NADPH oxidase subunit NOXO1 is a target for emphysema treatment in COPD.* Nat Metab, 2020. **2**(6): p. 532-546.
48. Vogelmeier, C.F., et al., *Global Strategy for the Diagnosis, Management, and Prevention of Chronic Obstructive Lung Disease 2017 Report: GOLD Executive Summary.* Eur Respir J, 2017. **49**(3).
49. Corrigan, C.J. and A.B. Kay, *The roles of inflammatory cells in the pathogenesis of asthma and of chronic obstructive pulmonary disease.* Am Rev Respir Dis, 1991. **143**(5 Pt 1): p. 1165-8; discussion 1175-6.
50. Shapiro, S.D., *Proteolysis in the lung.* Eur Respir J Suppl, 2003. **44**: p. 30s-32s.
51. MacNee, W., *Oxidants/antioxidants and chronic obstructive pulmonary disease: pathogenesis to therapy.* Novartis Found Symp, 2001. **234**: p. 169-85; discussion 185-8.
52. Brusselle, G.G., G.F. Joos, and K.R. Bracke, *New insights into the immunology of chronic obstructive pulmonary disease.* Lancet, 2011. **378**(9795): p. 1015-1026.
53. Hogg, J.C. and W. Timens, *The pathology of chronic obstructive pulmonary disease.* Annu Rev Pathol, 2009. **4**: p. 435-59.
54. Urbanowicz, R.A., et al., *Enhanced effector function of cytotoxic cells in the induced sputum of COPD patients.* Respir Res, 2010. **11**: p. 76.
55. Saetta, M., et al., *CD8+ T-lymphocytes in peripheral airways of smokers with chronic obstructive pulmonary disease.* Am J Respir Crit Care Med, 1998. **157**(3 Pt 1): p. 822-6.
56. Roh, J.S. and D.H. Sohn, *Damage-Associated Molecular Patterns in Inflammatory Diseases.* Immune Netw, 2018. **18**(4): p. e27.
57. Kumar, M., W. Seeger, and R. Voswinckel, *Senescence-associated secretory phenotype and its possible role in chronic obstructive pulmonary disease.* Am J Respir Cell Mol Biol, 2014. **51**(3): p. 323-33.
58. Coppe, J.P., et al., *The senescence-associated secretory phenotype: the dark side of tumor suppression.* Annu Rev Pathol, 2010. **5**: p. 99-118.
59. Lopez-Otin, C., et al., *The hallmarks of aging.* Cell, 2013. **153**(6): p. 1194-217.
60. Mercado, N., K. Ito, and P.J. Barnes, *Accelerated ageing of the lung in COPD: new concepts.* Thorax, 2015. **70**(5): p. 482-9.
61. Betteridge, D.J., *What is oxidative stress?* Metabolism, 2000. **49**(2 Suppl 1): p. 3-8.
62. Ichinose, M., et al., *Increase in reactive nitrogen species production in chronic obstructive pulmonary disease airways.* Am J Respir Crit Care Med, 2000. **162**(2 Pt 1): p. 701-6.
63. Ricciardolo, F.L., et al., *Nitrosative stress in the bronchial mucosa of severe chronic obstructive pulmonary disease.* J Allergy Clin Immunol, 2005. **116**(5): p. 1028-35.
64. Boukhenouna, S., et al., *Reactive Oxygen Species in Chronic Obstructive Pulmonary Disease.* Oxid Med Cell Longev, 2018. **2018**: p. 5730395.
65. Szabo, C., H. Ischiropoulos, and R. Radi, *Peroxynitrite: biochemistry, pathophysiology and development of therapeutics.* Nat Rev Drug Discov, 2007. **6**(8): p. 662-80.

66. Kharitonov, S.A. and P.J. Barnes, *Nitric oxide, nitrotyrosine, and nitric oxide modulators in asthma and chronic obstructive pulmonary disease.* Curr Allergy Asthma Rep, 2003. **3**(2): p. 121-9.
67. Jin, H., et al., *Smoking, COPD, and 3-nitrotyrosine levels of plasma proteins.* Environ Health Perspect, 2011. **119**(9): p. 1314-20.
68. Barnes, P.J., *Nitrosative stress in patients with asthma-chronic obstructive pulmonary disease overlap.* J Allergy Clin Immunol, 2019. **144**(4): p. 928-930.
69. Osoata, G.O., et al., *Peroxynitrite elevation in exhaled breath condensate of COPD and its inhibition by fudosteine.* Chest, 2009. **135**(6): p. 1513-20.
70. Barnes, P.J., *Cellular and molecular mechanisms of chronic obstructive pulmonary disease.* Clin Chest Med, 2014. **35**(1): p. 71-86.
71. Collaborators, G.B.D.C.R.D., *Global, regional, and national deaths, prevalence, disability-adjusted life years, and years lived with disability for chronic obstructive pulmonary disease and asthma, 1990-2015: a systematic analysis for the Global Burden of Disease Study 2015.* Lancet Respir Med, 2017. **5**(9): p. 691-706.
72. Agusti, A., et al., *Characterisation of COPD heterogeneity in the ECLIPSE cohort.* Respir Res, 2010. **11**: p. 122.
73. Boschetto, P., et al., *Predominant emphysema phenotype in chronic obstructive pulmonary.* Eur Respir J, 2003. **21**(3): p. 450-4.
74. Young, R.P., et al., *Functional variants of antioxidant genes in smokers with COPD and in those with normal lung function.* Thorax, 2006. **61**(5): p. 394-9.
75. Ross, D. and D. Siegel, *Functions of NQO1 in Cellular Protection and CoQ10 Metabolism and its Potential Role as a Redox Sensitive Molecular Switch.* Front Physiol, 2017. **8**: p. 595.
76. Boutten, A., et al., *NRF2 targeting: a promising therapeutic strategy in chronic obstructive pulmonary disease.* Trends Mol Med, 2011. **17**(7): p. 363-71.
77. Rangasamy, T., et al., *Genetic ablation of Nrf2 enhances susceptibility to cigarette smoke-induced emphysema in mice.* J Clin Invest, 2004. **114**(9): p. 1248-59.
78. Spira, A., et al., *Gene expression profiling of human lung tissue from smokers with severe emphysema.* Am J Respir Cell Mol Biol, 2004. **31**(6): p. 601-10.
79. Yamada, N., et al., *Microsatellite polymorphism in the heme oxygenase-1 gene promoter is associated with susceptibility to emphysema.* Am J Hum Genet, 2000. **66**(1): p. 187-95.
80. Ryter, S.W. and A.M. Choi, *Targeting heme oxygenase-1 and carbon monoxide for therapeutic modulation of inflammation.* Transl Res, 2016. **167**(1): p. 7-34.
81. Franco, N.H., *Animal Experiments in Biomedical Research: A Historical Perspective.* Animals (Basel), 2013. **3**(1): p. 238-73.
82. Brock, T.D., *Robert Koch: a life in medicine and bacteriology*. 1999: Zondervan.
83. Behring, E.v., *Ueber das zustandekommen der diphtherie-immunität und der tetanus-immunität bei thieren.* Drucke 19. Jh., 1890.
84. Shapiro, S.D., *Animal models for chronic obstructive pulmonary disease: age of klotho and marlboro mice.* Am J Respir Cell Mol Biol, 2000. **22**(1): p. 4-7.
85. Churg, A., M. Cosio, and J.L. Wright, *Mechanisms of cigarette smoke-induced COPD: insights from animal models.* Am J Physiol Lung Cell Mol Physiol, 2008. **294**(4): p. L612-31.

86. Gehr, P., et al., *Design of the mammalian respiratory system. V. Scaling morphometric pulmonary diffusing capacity to body mass: wild and domestic mammals.* Respiration physiology, 1981. **44**(1): p. 61-86.
87. Hoang, T.V., et al., *Stereological analysis of individual lung lobes during normal and aberrant mouse lung alveolarisation.* J Anat, 2018. **232**(3): p. 472-484.
88. Metzger, R.J., et al., *The branching programme of mouse lung development.* Nature, 2008. **453**(7196): p. 745-50.
89. Irvin, C.G. and J.H. Bates, *Measuring the lung function in the mouse: the challenge of size.* Respir Res, 2003. **4**: p. 4.
90. Gehr, P., M. Bachofen, and E.R. Weibel, *The normal human lung: ultrastructure and morphometric estimation of diffusion capacity.* Respir Physiol, 1978. **32**(2): p. 121-40.
91. Rock, J.R., S.H. Randell, and B.L. Hogan, *Airway basal stem cells: a perspective on their roles in epithelial homeostasis and remodeling.* Dis Model Mech, 2010. **3**(9-10): p. 545-56.
92. Wright, J.L., M. Cosio, and A. Churg, *Animal models of chronic obstructive pulmonary disease.* Am J Physiol Lung Cell Mol Physiol, 2008. **295**(1): p. L1-15.
93. Hadzic, S., et al., *The effect of long-term doxycycline treatment in a mouse model of cigarette smoke-induced emphysema and pulmonary hypertension.* Am J Physiol Lung Cell Mol Physiol, 2021. **320**(5): p. L903-L915.
94. Shapiro, S.D., et al., *Neutrophil elastase contributes to cigarette smoke-induced emphysema in mice.* Am J Pathol, 2003. **163**(6): p. 2329-35.
95. Reynolds, P.R., M.G. Cosio, and J.R. Hoidal, *Cigarette smoke-induced Egr-1 upregulates proinflammatory cytokines in pulmonary epithelial cells.* Am J Respir Cell Mol Biol, 2006. **35**(3): p. 314-9.
96. Nishikawa, M., et al., *Superoxide mediates cigarette smoke-induced infiltration of neutrophils into the airways through nuclear factor-kappaB activation and IL-8 mRNA expression in guinea pigs in vivo.* Am J Respir Cell Mol Biol, 1999. **20**(2): p. 189-98.
97. Pichl, A., et al., *Riociguat for treatment of pulmonary hypertension in COPD: a translational study.* Eur Respir J, 2019. **53**(6): 1802445.
98. Franciosi, L.G., et al., *Efficacy and safety of RPL554, a dual PDE3 and PDE4 inhibitor, in healthy volunteers and in patients with asthma or chronic obstructive pulmonary disease: findings from four clinical trials.* Lancet Respir Med, 2013. **1**(9): p. 714-27.
99. Tian, H., et al., *High-dose N-acetylcysteine for long-term, regular treatment of early-stage chronic obstructive pulmonary disease (GOLD I-II): study protocol for a multicenter, double-blinded, parallel-group, randomized controlled trial in China.* Trials, 2020. **21**(1): p. 780.
100. Fysikopoulos, A., et al., *Amelioration of elastase-induced lung emphysema and reversal of pulmonary hypertension by pharmacological iNOS inhibition in mice.* Br J Pharmacol, 2021. **178**(1): p. 152-171.
101. Hall, B., A. Limaye, and A.B. Kulkarni, *Overview: generation of gene knockout mice.* Curr Protoc Cell Biol, 2009. **Chapter 19**: p. Unit 19 12 19 12 1-17.
102. Vogel, G., *Nobel Prizes. A knockout award in medicine.* Science, 2007. **318**(5848): p. 178-9.
103. Matthaei, K.I., *Genetically manipulated mice: a powerful tool with unsuspected caveats.* J Physiol, 2007. **582**(Pt 2): p. 481-8.

104. Mahadeva, R. and S.D. Shapiro, *Chronic obstructive pulmonary disease * 3: Experimental animal models of pulmonary emphysema.* Thorax, 2002. **57**(10): p. 908-14.
105. Sternberg, N. and D. Hamilton, *Bacteriophage P1 site-specific recombination. I. Recombination between loxP sites.* J Mol Biol, 1981. **150**(4): p. 467-86.
106. Austin, S., M. Ziese, and N. Sternberg, *A novel role for site-specific recombination in maintenance of bacterial replicons.* Cell, 1981. **25**(3): p. 729-36.
107. Kim, H., et al., *Mouse Cre-LoxP system: general principles to determine tissue-specific roles of target genes.* Lab Anim Res, 2018. **34**(4): p. 147-159.
108. Metzger, D. and P. Chambon, *Site- and time-specific gene targeting in the mouse.* Methods, 2001. **24**(1): p. 71-80.
109. Indra, A.K., et al., *Temporally-controlled site-specific mutagenesis in the basal layer of the epidermis: comparison of the recombinase activity of the tamoxifen-inducible Cre-ER(T) and Cre-ER(T2) recombinases.* Nucleic Acids Res, 1999. **27**(22): p. 4324-7.
110. Floren, L.C., et al., *Tamoxifen in liver disease: potential exacerbation of hepatic dysfunction.* Ann Oncol, 1998. **9**(10): p. 1123-6.
111. Payne, S., S. De Val, and A. Neal, *Endothelial-Specific Cre Mouse Models.* Arterioscler Thromb Vasc Biol, 2018. **38**(11): p. 2550-2561.
112. Greenhalgh, S.N., K.P. Conroy, and N.C. Henderson, *Cre-ativity in the liver: transgenic approaches to targeting hepatic nonparenchymal cells.* Hepatology, 2015. **61**(6): p. 2091-9.
113. Diseases, G.B.D. and C. Injuries, *Global burden of 369 diseases and injuries in 204 countries and territories, 1990-2019: a systematic analysis for the Global Burden of Disease Study 2019.* Lancet, 2020. **396**(10258): p. 1204-1222.
114. Gredic, M., et al., *Myeloid cell-specific deletion of inducible nitric oxide synthase protects against smoke-induced pulmonary hypertension in mice.* Eur Respir J, 2021. **59**(4): 210053
115. Weiss, A., et al., *Targeting cyclin-dependent kinases for the treatment of pulmonary arterial hypertension.* Nat Commun, 2019. **10**(1): p. 2204.
116. Kohut, A., N. Patel, and H. Singh, *Comprehensive Echocardiographic Assessment of the Right Ventricle in Murine Models.* J Cardiovasc Ultrasound, 2016. **24**(3): p. 229-238.
117. Gouveia, L., et al., *Lung developmental arrest caused by PDGF-A deletion: consequences for the adult mouse lung.* Am J Physiol Lung Cell Mol Physiol, 2020. **318**(4): p. L831-l843.
118. Vichai, V. and K. Kirtikara, *Sulforhodamine B colorimetric assay for cytotoxicity screening.* Nat Protoc, 2006. **1**(3): p. 1112-6.
119. Moore, W.M., et al., *L-N6-(1-iminoethyl)lysine: a selective inhibitor of inducible nitric oxide synthase.* J Med Chem, 1994. **37**(23): p. 3886-8.
120. Cortese-Krott, M.M., et al., *A multilevel analytical approach for detection and visualization of intracellular NO production and nitrosation events using diaminofluoresceins.* Free Radic Biol Med, 2012. **53**(11): p. 2146-58.
121. Ochs, M. and J. Schipke, *A short primer on lung stereology.* Respir Res, 2021. **22**(1): p. 305.
122. Fischer, A.H., et al., *Hematoxylin and eosin staining of tissue and cell sections.* CSH Protoc, 2008. **2008**: p. pdb prot4986.
123. Weigert, C., *Uber eine Methode zur Farbung elastischer Fasern.* Zentralbl Allg Pathol Anat, 1898. **9**: p. 289-292.

124. Sterio, D.C., *The unbiased estimation of number and sizes of arbitrary particles using the disector.* J Microsc, 1984. **134**(Pt 2): p. 127-36.
125. Knudsen, L., C. Brandenberger, and M. Ochs, *Stereology as the 3D tool to quantitate lung architecture.* Histochem Cell Biol, 2021. **155**(2): p. 163-181.
126. D'Agostino, R.B. and A. Belanger, *A Suggestion for Using Powerful and Informative Tests of Normality.* The American Statistician, 1990. **44**(4): p. 316-321.
127. Duval, K., et al., *Modeling Physiological Events in 2D vs. 3D Cell Culture.* Physiology (Bethesda), 2017. **32**(4): p. 266-277.
128. Barkauskas, C.E., et al., *Lung organoids: current uses and future promise.* Development, 2017. **144**(6): p. 986-997.
129. Liu, G.H., et al., *Use of precision cut lung slices as a translational model for the study of lung biology.* Respir Res, 2019. **20**.
130. Huh, D., et al., *Reconstituting Organ-Level Lung Functions on a Chip.* Science, 2010. **328**(5986): p. 1662-1668.
131. Fang, Y. and R.M. Eglen, *Three-Dimensional Cell Cultures in Drug Discovery and Development.* Slas Discovery, 2017. **22**(5): p. 456-472.
132. Lacroix, G., et al., *Air–Liquid InterfaceIn VitroModels for Respiratory Toxicology Research: Consensus Workshop and Recommendations.* Applied In Vitro Toxicology, 2018. **4**(2): p. 91-106.
133. van der Toorn, M., et al., *Lipid-soluble components in cigarette smoke induce mitochondrial production of reactive oxygen species in lung epithelial cells.* Am J Physiol Lung Cell Mol Physiol, 2009. **297**(1): p. L109-14.
134. Barre-Sinoussi, F. and X. Montagutelli, *Animal models are essential to biological research: issues and perspectives.* Future Sci OA, 2015. **1**(4): p. FSO63.
135. Wendling, O., et al., *Efficient temporally-controlled targeted mutagenesis in smooth muscle cells of the adult mouse.* Genesis, 2009. **47**(1): p. 14-8.
136. Sheikh, A.Q., J.K. Lighthouse, and D.M. Greif, *Recapitulation of developing artery muscularization in pulmonary hypertension.* Cell Rep, 2014. **6**(5): p. 809-17.
137. Chakraborty, R., et al., *Promoters to Study Vascular Smooth Muscle.* Arterioscler Thromb Vasc Biol, 2019. **39**(4): p. 603-612.
138. Osborne, C.K., *Tamoxifen in the treatment of breast cancer.* N Engl J Med, 1998. **339**(22): p. 1609-18.
139. Hammad, S., et al., *Confounding influence of tamoxifen in mouse models of Cre recombinase-induced gene activity or modulation.* Arch Toxicol, 2018. **92**(8): p. 2549-2561.
140. Daurio, N.A., et al., *AMPK Activation and Metabolic Reprogramming by Tamoxifen through Estrogen Receptor-Independent Mechanisms Suggests New Uses for This Therapeutic Modality in Cancer Treatment.* Cancer Res, 2016. **76**(11): p. 3295-306.
141. Ilchuk, L.A., et al., *Limitations of Tamoxifen Application for In Vivo Genome Editing Using Cre/ER(T2) System.* Int J Mol Sci, 2022. **23**(22).
142. Wyatt, K.D., K. Sakamoto, and W.T. Watford, *Tamoxifen administration induces histopathologic changes within the lungs of Cre-recombinase-negative mice: A case report.* Lab Anim, 2022. **56**(3): p. 297-303.
143. Gunschmann, C., et al., *Transgenic mouse technology in skin biology: inducible gene knockout in mice.* J Invest Dermatol, 2014. **134**(7): p. 1-4.

144. Forstermann, U. and W.C. Sessa, *Nitric oxide synthases: regulation and function.* Eur Heart J, 2012. **33**(7): p. 829-37, 837a-837d.
145. Dick, A.S., et al., *Cyclic stretch stimulates nitric oxide synthase-1-dependent peroxynitrite formation by neonatal rat pulmonary artery smooth muscle.* Free Radic Biol Med, 2013. **61**: p. 310-9.
146. Tan, X., et al., *Histone deacetylase inhibitors promote eNOS expression in vascular smooth muscle cells and suppress hypoxia-induced cell growth.* J Cell Mol Med, 2017. **21**(9): p. 2022-2035.
147. Kim, H.J., et al., *Wall stretch and thromboxane A(2) activate NO synthase (eNOS) in pulmonary arterial smooth muscle cells via H(2)O(2) and Akt-dependent phosphorylation.* Pflugers Arch, 2016. **468**(4): p. 705-16.
148. Wink, D.A. and J.B. Mitchell, *Chemical biology of nitric oxide: Insights into regulatory, cytotoxic, and cytoprotective mechanisms of nitric oxide.* Free Radic Biol Med, 1998. **25**(4-5): p. 434-56.
149. Moiseenko, A., et al., *Origin and characterization of alpha smooth muscle actin-positive cells during murine lung development.* Stem Cells, 2017. **35**(6): p. 1566-1578.
150. Guerassimov, A., et al., *The development of emphysema in cigarette smoke-exposed mice is strain dependent.* Am J Respir Crit Care Med, 2004. **170**(9): p. 974-80.
151. Gao, S., et al., *Echocardiography in Mice.* Curr Protoc Mouse Biol, 2011. **1**: p. 71-83.
152. Roth, D.M., et al., *Impact of anesthesia on cardiac function during echocardiography in mice.* Am J Physiol Heart Circ Physiol, 2002. **282**(6): p. H2134-40.
153. Stypmann, J., *Doppler ultrasound in mice.* Echocardiography, 2007. **24**(1): p. 97-112.
154. Bleeker, G.B., et al., *Assessing right ventricular function: the role of echocardiography and complementary technologies.* Heart, 2006. **92 Suppl 1**: p. i19-26.
155. Hendriks, T., et al., *Active Tobacco Smoking Impairs Cardiac Systolic Function.* Sci Rep, 2020. **10**(1): p. 6608.
156. Dignam, J.P., et al., *Animal models of pulmonary hypertension: Getting to the heart of the problem.* Br J Pharmacol, 2021.
157. Zelt, J.G.E., et al., *Medical Therapy for Heart Failure Associated With Pulmonary Hypertension.* Circ Res, 2019. **124**(11): p. 1551-1567.
158. De Raaf, M.A., et al., *Histone deacetylase inhibition with trichostatin A does not reverse severe angioproliferative pulmonary hypertension in rats (2013 Grover Conference series).* Pulm Circ, 2014. **4**(2): p. 237-43.
159. Boehm, M., et al., *Delineating the molecular and histological events that govern right ventricular recovery using a novel mouse model of pulmonary artery de-banding.* Cardiovasc Res, 2020. **116**(10): p. 1700-1709.
160. Sussan, T.E., et al., *Targeting Nrf2 with the triterpenoid CDDO-imidazolide attenuates cigarette smoke-induced emphysema and cardiac dysfunction in mice.* Proc Natl Acad Sci U S A, 2009. **106**(1): p. 250-5.
161. Ermert, M., et al., *Cell-specific nitric oxide synthase-isoenzyme expression and regulation in response to endotoxin in intact rat lungs.* Lab Invest, 2002. **82**(4): p. 425-41.
162. Stevens, T., et al., *Lung vascular cell heterogeneity: endothelium, smooth muscle, and fibroblasts.* Proc Am Thorac Soc, 2008. **5**(7): p. 783-91.
163. Kotton, D.N. and E.E. Morrisey, *Lung regeneration: mechanisms, applications and emerging stem cell populations.* Nat Med, 2014. **20**(8): p. 822-32.

164. Tsao, P.N., et al., *Epithelial Notch signaling regulates lung alveolar morphogenesis and airway epithelial integrity.* Proc Natl Acad Sci U S A, 2016. **113**(29): p. 8242-7.
165. Peng, T., et al., *Hedgehog actively maintains adult lung quiescence and regulates repair and regeneration.* Nature, 2015. **526**(7574): p. 578-82.
166. Raslan, A.A. and J.K. Yoon, *WNT Signaling in Lung Repair and Regeneration.* Mol Cells, 2020. **43**(9): p. 774-783.
167. Gokey, J.J., S.D. Patel, and J.A. Kropski, *The Role of Hippo/YAP Signaling in Alveolar Repair and Pulmonary Fibrosis.* Front Med (Lausanne), 2021. **8**: p. 752316.
168. Peng, T., et al., *Coordination of heart and lung co-development by a multipotent cardiopulmonary progenitor.* Nature, 2013. **500**(7464): p. 589-92.
169. Moiseenko, A., et al., *Identification of a Repair-Supportive Mesenchymal Cell Population during Airway Epithelial Regeneration.* Cell Rep, 2020. **33**(12): p. 108549.
170. Speyer, C.L., et al., *Regulatory effects of iNOS on acute lung inflammatory responses in mice.* Am J Pathol, 2003. **163**(6): p. 2319-28.
171. Kharitonov, S.A. and K. Ito, *Chapter 30 - Nitric Oxide*, in *Asthma and COPD (Second Edition)*, P.J. Barnes, et al., Editors. 2009, Academic Press: Oxford. p. 363-372.
172. Zepp, J.A., et al., *Distinct Mesenchymal Lineages and Niches Promote Epithelial Self-Renewal and Myofibrogenesis in the Lung.* Cell, 2017. **170**(6): p. 1134-1148 e10.
173. Kruk, D., et al., *Mesenchymal Stromal Cells to Regenerate Emphysema: On the Horizon?* Respiration, 2018. **96**(2): p. 148-158.
174. Karvonen, H.M., et al., *Myofibroblast expression in airways and alveoli is affected by smoking and COPD.* Respir Res, 2013. **14**: p. 84.
175. Pittenger, M.F., et al., *Mesenchymal stem cell perspective: cell biology to clinical progress.* NPJ Regen Med, 2019. **4**: p. 22.